

UNIVERSIDADE DE SÃO PAULO
INSTITUTO DE FÍSICA DE SÃO CARLOS

VALERIA SPOLON MARANGONI

Theranostic nanomaterials applied to the cancer diagnostic and therapy and
nanotoxicology studies

São Carlos
2016

VALERIA SPOLON MARANGONI

Theranostic nanomaterials applied to the cancer diagnostic and therapy and
nanotoxicology studies

Thesis presented to the Graduate Program in
Physics at the Instituto de Física de São
Carlos, Universidade de São Paulo to obtain
the degree of Doctor of Science.

Concentration area: Applied Physics
Option: Biomolecular Physics

Advisor: Prof. Dr. Valtencir Zucolotto

Corrected version

(Original version available on the Program Unit)

São Carlos

2016

AUTHORIZE THE REPRODUCTION AND DISSEMINATION OF TOTAL OR PARTIAL COPIES OF THIS THESIS, BY CONVENCIONAL OR ELECTRONIC MEDIA FOR STUDY OR RESEARCH PURPOSE, SINCE IT IS REFERENCED.

Cataloguing data reviewed by the Library and Information Service
of the IFSC, with information provided by the author

Marangoni, Valeria Spolon

Theranostic nanomaterials applied to the cancer
diagnostic and therapy and nanotoxicology studies /
Valeria Spolon Marangoni; advisor Valtencir
Zucolotto - reviewed version -- São Carlos 2016.
154 p.

Thesis (Doctorate - Graduate Program in
Biomolecular Physics) -- Instituto de Física de São
Carlos, Universidade de São Paulo - Brasil , 2016.

1. Plasmonic nanoparticles. 2. Photothermal
therapy. 3. Magnetic resonance imaging. I.
Zucolotto, Valtencir, advisor. II. Title.

*To my parents, Marcia e Adenir,
and my brother Bruno
for their love and support*

ACKNOWLEDGEMENTS

I would like to express my deep gratitude to all people and institutions that have contributed direct or indirectly during my graduate school. First, I would like to acknowledge God for all opportunities to learn and be better and to keep me strong to overcome all adversities.

I deeply acknowledge my parents Marcia and Adenir for always provide education for me and my brother. I thank them for being my friends, encouraging me in all my decisions, and for their unconditional love and patience.

I deeply acknowledge Pedro for being “more than just a partner..”, for being my best friend. I also thank his family, in special his parents Rosa Helena and Adalmir, for making me feel as family and always encouraging me.

I deeply acknowledge my advisor prof. Dr. Valtencir Zucolotto for all opportunities and trust during these years. I highly appreciate the freedom I had on choosing my projects and pursuing them. I thank him for always involve me in exciting projects, which have expanded my knowledge.

I deeply acknowledge prof. Dr. Naomi Halas for receiving me twice in your laboratory during the PhD. I thank her for trust me and give me all support to develop the project. I highly appreciate her suggestions and constructive criticism that have made me a better researcher and person.

I deeply thank Dr. Oara Neumann for being not only a researcher partner, but, more importantly, a good friend. I thank her for supporting me in the lab, presentations, writing, for walking me home and give me many advices. I have no words to express all my gratitude.

I deeply acknowledge prof. Dr. Jim Bankson. Specially, I thank Caterina Kaffes for helping with the MRI measurements and for always being willing to stay during the nights and weekends doing the measurements with me.

I thank prof. Dr. Peter Nordlander and his student Hui Zhang for helping with the theoretical model for the MRI-active nanoparticles, which allowed a better understanding about the system.

I deeply acknowledge Dr. Sandra Bishnoi for helping me in writing the project and supporting me in the research. I highly appreciate her help (inside and outside the Lab) and the helpful discussions.

I deeply acknowledge Dr. Ciceron Ayala-Orozco, my mentor during the beginning of my internship in Houston, for guiding me quickly throughout the synthesis.

I deeply thank to my dear friend and research collaborator, Dra. Juliana Cancino-Bernardi for helping me in the experiments, especially those of tens of cell culture plates.

I thank Dra. Lilian Centurion for being a good friend and collaborator during all these years. I also thank her for helping in the text revision of this thesis.

I thank everybody that keeps the GNano lab working: Jaque, Julielle, Romeu, Nelzeli. I thank Martha Alexander, Sandy Willians, Surbhi Lal, for all of the work with the invoices at LANP (Rice University) and for helping me with the visa paperwork.

I thank my very good friends from GNano: Lais Brazaca, Jaque, Camilo, Idelma, Nirton, Lorena, Paula, Henrique, Fran, Cris, Lais Ribovisk, Helena, Adrislaine, Isa, Olavo, Abilene. I also thank Ila and Clara for helpful discussions in the cell culture room and friendship.

I am also grateful to my close friends Paty, Ana Eliza, Amanda and our princess Sofia. I thank them for their help and support all the time.

I thank Nayára Oliveira to show me the importance of the self-knowledge for the personal and professional evolution during the coaching program.

I thank all the undergrad and masters students that I have opportunity to guide during all these years. The opportunities to work with different projects and problems have made me a better researcher and person.

I thank my dear friend Tatiana Wolfe for helping me in Houston, especially in the first time in 2012. I highly appreciate her friendship, support, and scientific discussions. I also would like to thank my good Brazilian friends in Houston: Caio, Angelica, Daniel, Fabio, Gustavo, Leonardo.

I deeply thank my very good friends in Houston: Pratiksha, Tiyaash, Mihika, Liangliang. Thank you for supporting and helping me in the difficult moments and for showing me different cultures and foods.

I thank all Halas' group members, especially Andie, Adam, Ali, Dayne, Alejandra, Ben, Bob, Linan, Chao, Fanfang, Shu, Amanda, Michael, Nate, Sam for all useful discussions and help.

I deeply acknowledge Instituto de Física de São Carlos - IFSC, for the award "Yvonne Primerano Mascarenhas", which give me the financial support to do my first internship at Rice University in 2012.

I thank Fundação de Amparo a Pesquisa do Estado de São Paulo (FAPESP) for the fellowship during the PhD (2012/11166-4) and for the research internships abroad (BEPE) (2014/13645-2). I also would like to thank the opportunities to participate of international conferences, which have expanded my vision of science and world.

I acknowledge the Laboratorio de Microscopia Eletrônica (Laboratório Nacional de Nanotecnologia – LNNano, Campinas) for the training and possibility to use the Transmission Electron Microscopy many times during the PhD.

I thank the IFSC multi-user laboratories: Laboratorio de Microscopia Eletronica and Microscopia confocal. I would like to thank prof. Dr Francisco Guimarães for helping with the confocal microscopy and Daniela Correa de Melo for helping with the Iatroscan measurements.

I deeply acknowledge the post-graduation office and library for always being willing to help the students, especially with the thesis and deadlines.

I thank Rice University for providing a singular infrastructure and cultural activities during my internship program. I deeply thank Dr. Pennington and Dr. Wenhua for training me on ICP-MS and TEM, and Dr. Budi Utama for helping with the confocal measurements. I thank the faculty and staff of Chemistry Department, the Office of International Students and Scholars (OISS), and of the collaborating institution MD Anderson Cancer Center. I thank Mayra Onuchic for the important work at Brazil@Rice, and all support.

Finally, I would like to thank Universidade de Sao Paulo, especially Instituto de Química de Sao Carlos (IQSC) and Fisica de Sao Carlos (IFSC), and all professors and faculty, for the exceptional education that I received in this decade (bachelor, master and PhD).

“In a gentle way, you can shake the world”

Mahatma Gandhi

ABSTRACT

MARANGONI, V. S. **Theranostic nanomaterials applied to the cancer diagnostic and therapy and nanotoxicity studies**. 2016. 154 p. Thesis (Doctor in Science) - Instituto de Física de São Carlos, Universidade de São Paulo, São Carlos, 2016.

Multifunctional plasmonic nanoparticles have shown extraordinary potential for near infrared photothermal and triggered-therapeutic release treatments of solid tumors. However, the accumulation rate of the nanoparticles in the target tissue, which depends on their capacity to escape the immune system, and the ability to efficiently and accurately track these particles *in vivo* are still limited. To address these challenges, we have created two different systems. The first one is a multifunctional nanocarrier in which PEG-coated gold nanorods were grouped into natural cell membrane vesicles from lung cancer cell membranes (A549) and loaded with β -lap (CM- β -lap-PEG-AuNRs). Our goal was to develop specific multifunctional systems for cancer treatment by using the antigens and the unique properties of the cancer cell membrane combined with photothermal properties of AuNRs and anticancer activity of β -lap. The results confirmed the assembly of PEG-AuNRs inside the vesicles and the irradiation with NIR laser led to disruption of the vesicles and release of the PEG-AuNRs and β -Lap. *In vitro* studies revealed an enhanced and synergic cytotoxicity against A549 cancer cells, which can be attributed to the specific cytotoxicity of β -Lap combined with heat generated by laser irradiation of the AuNRs. No cytotoxicity was observed in absence of laser irradiation. In the second system, MRI-active Au nanomaterials were developed. These are Au core-silica layer-Au shell nanoparticles, where Gd(III) ions are encapsulated within the silica layer between the inner core and outer Au layer of the nanoparticle (Gd-NM). This theranostic nanoparticle retains its strong near infrared optical absorption properties, essential for *in vivo* photothermal cancer therapy, while simultaneously providing increased T_1 contrast in MR imaging by concentrating Gd(III) within the nanoparticle. Measurements of Gd-NM revealed a substantially enhanced T_1 relaxivity ($r_1 \sim 17 \text{ mM}^{-1} \text{ s}^{-1}$) even at 4.7 T, surpassing conventional Gd(III)-DOTA chelating agents ($r_1 \sim 4 \text{ mM}^{-1} \text{ s}^{-1}$) currently in clinical use. The observed relaxivities are consistent with Solomon-Bloembergen-Morgan (SBM) theory, describing the longer-range interactions between the Gd(III) and protons outside the nanoparticle. These novel multifunctional systems open the door for the development of more efficient nanoplatforms for diagnosis and treatment of cancer.

Keywords: Plasmonic nanoparticles. Photothermal therapy. Magnetic resonance imaging.

RESUMO

MARANGONI, V. S. **Nanomateriais Teranósticos Aplicados à Problemática do Câncer e Estudos de Nanotoxicidade**. 2016. 154 p. Tese (Doutorado em Ciências) - Instituto de Física de São Carlos, Universidade de São Paulo, São Carlos, 2016.

Nanopartículas plasmônicas multifuncionais têm revelado elevado potencial para fototermia na região (NIR) do infravermelho e liberação controlada de fármacos para o tratamento de tumores sólidos. No entanto, a taxa de acumulação das nanopartículas no tecido alvo, que depende da capacidade delas de escapar do sistema imunológico, e a habilidade de rastrear de maneira efetiva essas partículas *in vivo* ainda são limitadas. Para superar essas barreiras, dois sistemas diferentes foram desenvolvidos. O primeiro corresponde a um nanocarreador multifuncional, onde nanobastões de ouro funcionalizados com PEG foram agrupados dentro de vesículas de membranas de células naturais originárias de células cancerígenas de pulmão (A549) conjugadas com β -Lap (CM- β -lap-PEG-AuNRs). Nosso principal objetivo foi desenvolver um sistema multifuncional específico para tratamento de câncer utilizando os antígenos e propriedades únicas da membrana das células cancerígenas combinados com as propriedades fototérmicas dos AuNRs e a atividade anticancerígena da β -Lap. Os resultados confirmaram o agrupamento dos PEG-AuNRs dentro das CM e irradiação com o laser no NIR levou ao rompimento das vesículas e liberação dos AuNRs e β -Lap. Estudos *in vitro* revelaram uma elevada e sinérgica citotoxicidade contra células A549, que pode ser atribuída a combinação da específica toxicidade da β -Lap com o calor gerado pelos AuNRs por meio da irradiação com laser. Nenhuma citotoxicidade significativa foi observada na ausência de irradiação com laser. No segundo sistema, nanomatyoshkas de Au ativas em MRI foram desenvolvidas. Elas consistem em um núcleo de Au, uma camada intersticial de sílica, onde os íons de Gd(III) são encapsulados, e uma camada externa de Au (Gd-NM). Esta nanopartícula teranóstica mantém as propriedades de elevada absorção óptica no NIR, enquanto simultaneamente fornece um elevado contraste T_1 em imagem por ressonância magnética por meio da concentração dos íons de Gd(III) dentro da nanopartícula. Medidas de Gd-NM revelaram uma relaxividade elevada ($r_1 \sim 17 \text{ mM}^{-1} \text{ s}^{-1}$) a 4,7 T, superando os convencionais agentes quelantes de Gd(III)-DOTA ($r_1 \sim 4 \text{ mM}^{-1} \text{ s}^{-1}$) utilizados clinicamente. As relaxividades observadas são consistentes com a teoria Solomon-Bloembergen-Morgan (SBM), descrevendo as interações de longo alcance entre Gd(III) e prótons de H fora da partícula. Os novos sistemas multifuncionais desenvolvidos abrem oportunidades para o

desenvolvimento de nanoplataformas mais eficientes para o diagnóstico e tratamento de câncer.

Palavras-chave: Nanopartículas plasmônicas. Terapia fototérmica. Imagem por ressonância magnética.

LIST OF FIGURES

Figure 2.1 - Schematic representation of the SPR oscillation and its respective extinction spectra for gold (A) nanospheres and (B) nanorods.	39
Figure 2.2 - Schematic representation of a gold nanoshell and a representative extinction spectrum for a $[r_1, r_2] = [62, 76]$ nm.....	42
Figure 2.3 - Schematic energy-level diagram describing the plasmon hybridization in gold nanoshells resulting from the interaction between the sphere and cavity plasmons.....	43
Figure 2.4 - Schematic representation of a gold nanomatrixoshka and a representative extinction spectrum for a $[r_1, r_2, r_3] = [24, 34, 44]$ nm.....	44
Figure 2.5 - Schematic representation of the gold nanorod synthesis process. (A) First, small gold nanoparticles are synthesized in the presence of CTAB, and (B) used as seeds for the growth of the nanorods.	49
Figure 2.6 - Characterization of the seeds: (A) UV-VIS-NIR spectrum, (B) Hydrodynamic diameter obtained from Dynamic Light Scattering measurements, and (C) TEM image, showing very small particles.....	49
Figure 2.7 - (A) UV-VIS-NIR spectra showing the growth kinetics of nanorods after addition of 100 μ L of seeds into the growth solution, and (B) the changing in the maximal wavelength of the longitudinal band as function of time.....	50
Figure 2.8 - UV-VIS-NIR spectra of AuNRs obtained using different amount of AgNO_3 and the respective TEM images. The aspect ratio are 2.1, 2.8, and 3.5 for blue, green, and red, respectively. Scale bar = 50 nm.....	51
Figure 2.9 - TEM images of the gold nanorods with maximal longitudinal absorption at 700 nm, showing a monodisperse system.	51
Figure 2.10 - UV-VIS-NIR spectra of gold nanorods prepared with different concentrations of seeds.	52
Figure 2.11 - (A) Schematic representation of the gold nanomatrixoshka synthesis: 50 nm diameter gold colloids are coated with SiO_2 -APTES shell, followed by a continuous gold shell.....	53
Figure 2.12 - UV-VIS-NIR extinction spectra and their respective TEM images corresponding to (A) Au colloids of about 50 nm, (B) APTES- SiO_2 -coated Au colloids, and (C) gold nanomatrixoshkas.	54

Figure 2.13 - UV-VIS-NIR spectra of gold nanomatryoskas obtained using different amount of seeded precursor.....	55
Figure 2.14 - UV-VIS-NIR spectrum of Au-coated Au ₂ S nanoshells and its respective TEM image.....	56
Figure 2.15 - Analysis of the composition of the (A) nanoshells and (B) triangular plates by High Resolution TEM coupled with energy dispersive spectroscopy (EDS).....	56
Figure 2.16 - Pictures of the centrifuge tubes before and after the centrifugation showing the separation of the particles through the density gradient, and the UV-VIS-NIR spectra and TEM images of the two indicated fractions.....	57
Figure 2.17 - UV-VIS-NIR spectra and their respective TEM images of different synthesis process to synthesized Au-coated Au ₂ S nanoshells. (A) Na ₂ S ₂ O ₃ :HAuCl ₄ (18 mL:10 mL); (B) Na ₂ S : HAuCl ₄ (18 mL : 10 mL) under N ₂ atmosphere; (C) Na ₂ S : HAuCl ₄ (18 mL : 10 mL) in pH = 1.6, and (D) Na ₂ S : HAuCl ₄ (10 mL : 10 mL), and after 5 min, more 2 mL of Na ₂ S were added.	58
Figure 2.18 - UV-VIS-NIR spectrum and the respective TEM image taken 1h30 after mixing HAuCl ₄ with NaOH and then with Na ₂ S.	59
Figure 2.19 - UV-VIS-NIR spectrum and the respective TEM image of the Au-coated Au ₂ S nanoshells prepared by a new two-step method.....	60
Figure 3.1 - The near infrared region (NIR) window for <i>in vivo</i> applications, showing the region of minimal light absorption by hemoglobin and water.	65
Figure 3.2 - Schematics of the synthesis of the Red blood cell (RBC) membrane-coated polymeric PLGA nanoparticles.	69
Figure 3.3 - Chemical structure of β -Lapachone.	71
Figure 3.4 - Schematic representation (not to scale) of proposed mechanism for the fabrication of the cancer cell membrane-coated PEG-Gold nanorods and loaded with the anticancer agent β -Lapachone (CM- β -Lap-PEG-AuNRs). First, A549 lung cancer cells are isolated, lysed to remove the internal content and purified by ultracentrifugation. β -Lap is loaded on cell membrane structure and they are extruded through 200 porous membrane (CM- β -Lap). In parallel, gold nanorods (AuNRs) are synthesized by the seed-mediated method in presence of surfactant CTAB, followed by covalent functionalization with mPEG-SH. The fusion of the resulting PEG-AuNRs and CM- β -Lap are performed by mechanical extrusion through 100 nm pore membrane.	83

- Figure 3.5** - a) Representative spectra of β -Lap in water:ethanol (1:1) in different concentrations and b) Calibration curve of β -Lap at 257 nm made from triplicate of the spectra in different concentrations..... 83
- Figure 3.6** - Calibration curve of BSA protein obtained from bicinchoninic acid (BCA) assay and used to determine the protein concentration on the cell membranes vesicles (CM)..... 84
- Figure 3.7** - Characterization of the A549 cell membrane (CM). (A) Polyacrylamide gel electrophoresis (PAGE-SDS) of the CM in duplicate. (B) Dynamic light scattering analysis of the CM- β -Lap after extrusion through 200 nm porous polycarbonate membrane, and (C) UV-VIS spectra of CM with/without β -Lapachone. 85
- Figure 3.8** - Iatroscan TLC/FID chromatograms of standard lipids and A549 cell membrane (CM) samples. 86
- Figure 3.9** - (A) Representative FEG-SEM image of the PEG-AuNRs and (B) Histogram of length and (C) width determined by measuring about 100 particles using the software ImageJ. The average aspect ratio (length/width) calculated from the mean 47.4/13.37 was about 3.5. 87
- Figure 3.10** - Characterization of gold nanorods coated with cell membrane loaded β -Lapachone (CM- β -Lap-PEG-AUNRs) and comparison with PEG-AuNRs. (A) UV-VIS-NIR spectra and (B) hydrodynamic diameter obtained from DLS measurements of PEG-AuNRs before and after coating with CM- β -Lap. Longitudinal plasma resonance of PEG-AuNRs ($\lambda_{\text{max}} \sim 750$ nm) decreased after the coating. C) Zeta potential of the AuNRs before and after functionalizations, D) stability of CM- β -Lap-PEG-AuNRs in PBS buffer and 10% Fetal Bovine Serum; (e) and (f) FEG-SEM images of CM- β -Lap-PEG-AuNRs showing the PEG-AUNRs grouped inside the cell membrane vesicles. 89
- Figure 3.11** - (A) Representative FEG-SEM image of CM- β -PEG-AuNRs and (B) histogram determined by measuring about 100 particles using the software ImageJ. The average diameter calculated was about 109 nm. 90
- Figure 3.12** - Representative FEG-SEM image of the CM- β -Lap-coated CTAB-AuNRs. No spherical cell membrane vesicles are observed, suggesting their destabilization in presence of the surfactant CTAB..... 90
- Figure 3.13** - Plots of heat flow vs time of microcalorimetric titration of (a) PEG-AuNRs; (b) CM- β -Lap-PEG-AuNRs and (c) CTAB/PEG-AuNRs by BSA solution. Injections of 2 μ L, at 25 $^{\circ}$ C, of 0.01 mM of BSA solution were

made on nanoparticles suspensions. Control of BSA dilution was carried out by injections of BSA solution in buffer.92

Figure 3.14 - (A) Representative of temperature change vs time in suspensions (optical density at 750 nm = 1) irradiated with 808 nm laser with power density of 1.5 W/cm^2 , (B) Increase of the longitudinal band with the laser irradiation, (C) release of β -Lapachone at different time of irradiation. SEM images of CM- β -Lap-PEG-AuNRs (D) before, (E) after 10 min and (F) after 20 min of laser irradiation. The laser irradiation increases the temperature of the suspension, breaks the vesicles and causes the release of the AuNRs.....94

Figure 3.15 - Photothermal therapy of A549 cancer cells treated with CM- β -Lap-PEG-AuNRs and CM-PEG-AuNRs. The highlight areas represent approximately the laser spots ($\sim 1.5 \text{ W/cm}^2$, 10 min) on the samples. Dead cells were stained with Trypan Blue. Cells without the particles are not affected by the laser irradiation while cells incubated with CM- β -Lap-PEG-AuNRs and CM-PEG-AuNRs were visibly injured.....95

Figure 3.16 - Photothermal therapy of A549 cancer cells treated with CM- β -Lap-PEG-AuNRs and CM-PEG-AuNRs for 4 h. The highlight areas represent approximately the laser spots ($\sim 1.5 \text{ W/cm}^2$, 10 min) on the samples. Dead cells were stained with Trypan Blue. Cells without the particles are not affected by the laser irradiation while cells incubated with CM- β -Lap-PEG-AuNRs and CM-PEG-AuNRs were visibly injured.....96

Figure 3.17 - (A) Confocal images of A549 cells after cell exposure to CM-PEG-AuNRs for 4 h. Blue: cell nuclei (Hoechst 33258). red: CellMask Deep Red-labeled CM-PEG-AuNRs (Exc/Em = 649/667 nm). (B) Time dependence of the extinction at 750 nm of the cells treated with CM- β -Lap-PEG-AuNRs, showing the dynamic of the uptake of the particles. The data were corrected by the number of cells (relative ext) and are showed as mean \pm SD of triplicate. (C) Comparison of the uptake of PEG-AuNRs and CM- β -Lap-PEG-AuNRs after 4 h of incubation. The extinctions were corrected by the number of cells and normalized.98

Figure 3.18 - Intracellular uptake of CM-PEG-AuNRs. Samples were incubated with A549 cells for 4 h. Red: CellMask Deep Red-labeled CM-PEG-AuNRs (Exc/Em = 649/667 nm); Blue: nuclei stained with Hoechst 33258. CM-PEG-AuNRs show strong signal when nucleus is in focus (middle row), demonstrating cellular uptake.99

Figure 3.19 - Confocal images of A549 cells after cell exposure to CellMask Deep Red stain (a, b, c) and CellMask-stained CM-PEG-AuNRs (d, e, f) for 4 h. Blue: cell nuclei (Hoechst 33258).100

- Figure 3.20** - Cell viability, evaluated by (a) MTT; (b) Crystal Violet, and (c) MTT of A549, HTC and HepaRG cells after incubation with the samples for 24 h. In (a) and (b) the columns blue, green, and red represent the quantities of 5, 10 and 15 μL , respectively. In (c) the columns red, green, blue, light blue and pink represents the concentrations of 0.5, 1.0, 2.0, 4.0 and 8.0 μM of $\beta\text{-Lap}$, respectively. The relative percentage of viable cells was calculated by considering the control as 100% of viable cells. The results represent the mean \pm SD of data normalized to untreated controls from two independent experiments in triplicate. $*P < 0.05$ with respect to untreated controls. 102
- Figure 3.21** - Measurement of generation of ROS in A549 and HepaRG cells. (a) Cells were incubated with the samples and the generation of ROS was measured using the 2',7'-dichlorodihydrofluorescein diacetate (H2DCFDA) assay. The relative percentage was calculated by considering the control as 100%. Data are expressed as mean \pm SD of triplicate from two independent experiments. $*P < 0.05$ with respect to untreated controls. 103
- Figure 4.1** - Schematic showing the main differences between T_1 and T_2 relaxation. 107
- Figure 4.2** - (A) Schematic representation of the MRI active nanomatryoshka synthesis showing the stepwise synthesis process: the 50 nm diameter gold colloids are coated with Gd(III) chelates embedded in a SiO_2 shell and then a continuous Au shell. (B) TEM images corresponding to each step in the process; scale bars are 100 nm. 120
- Figure 4.3** - (A) FTIR spectra of (i) $\text{Au@SiO}_2\text{-APTES}$, (ii) Gd-DOTA-SCN , and (iii) Gd-doped SiO_2 -coated Au colloid. The disappearance of the 2100 cm^{-1} peak, attributed to the $\text{N}=\text{C}=\text{S}$ vibration, is an indicative of the bond between Gd-DOTA-SCN and the amine groups from APTES (B) the chemical reaction showing the bond formation. The table shows the FTIR peak assessments corresponding to each spectrum. 121
- Figure 4.4** - High resolution TEM images of: (A) SiO_2 -coated Au colloid and (B) Gd-doped SiO_2 coated Au colloid. 121
- Figure 4.5** - (A) The r_1 relaxivity of Gd-NM as a function of the number of Gd(III) per NM measured at 4.7 T. (B) The r_1 relaxivities of Gd(III)-DOTA (for comparison), Gd(III)-NM, and Gd(III)-NM-PEG; error bars represent standard deviation of three independent experiments at 25°C . (C) Thermal variation of T_1 for Gd-NM-PEG at 25°C (blue, $r_1 = 14.6\text{ mM}^{-1}\text{ s}^{-1}$) and 37°C (red, $r_1 = 16.1\text{ mM}^{-1}\text{ s}^{-1}$). The r_1 values were extracted from the slopes. 122

- Figure 4.6** - T_1 (longitudinal) rate of Gd-NM for: (A) 0.8×10^5 , (B) 2.7×10^5 , and (C) 8.2×10^5 numbers of Gd(III) ions per particle at 4.7 T and 25°C. The r_1 values were extracted from the slopes.....123
- Figure 4.7** - (A) Dynamic Light Scattering and (B) Zeta potential for Gd-NM before and after PEG surface functionalization.....124
- Figure 4.8** - (A) Schematic representation of (A) the regular NM synthesis and (B) the functionalization of the NM with Gd(III) chelate (GdPEG-coated-NM).....125
- Figure 4.9** - (A) Dynamic Light Scattering and (B) Zeta potential for regular NM before and after conjugation with PEG-NH₂ and Gd chelates (GdPEG-coated-NM).125
- Figure 4.10** - Percentage of Gd(III) ions released from Gd-NM-PEG, where the Gd(III) is located inside the NM which is then functionalized using PEG, versus GdPEG-coated NM, where the Gd(III)-DOTA-SCN is attached outside the NM through a thiol-PEG-amine linker, after 48 h of incubation at 37°C in 10% FBS (red) and H₂O (blue). Gd(III) concentration was quantified using ICP-MS.....126
- Figure 4.11** - (A) T_1 (longitudinal) rate and (B) extinction spectra for Gd-NM-PEG in water (blue) and 10% serum (red). (C) T_1 (longitudinal) rate and (D) extinction spectra GdPEG-coated NM in water (blue) and 10% serum (red). The T_1 measurements were performed at 4.7 T and 25°C.127
- Figure 4.12** - T_1 (longitudinal) rate versus Gd(III) concentration at 4.7 T for (A) seeded precursor, (B) Gd-NM-PEG, and (C) GdPEG-coated-NM; and the corresponding (D,E,F) extinction spectra and (G,H,I) TEM images; (scale bar are 50 nm). (Insets A-C: T_1 weighted MR images).....129
- Figure 4.13** - (A) Longitudinal rate at 4.7 T versus Gd(III) concentration for two Au shell thicknesses of Gd-NM-PEG: 18 nm (blue; $r_1 = 12.9 \text{ mM}^{-1}\text{s}^{-1}$) and 38 nm (red; $r_1 = 1.2 \text{ mM}^{-1}\text{s}^{-1}$) the Gd(III) concentration per NM was 2.3×10^5 in both cases, (B) T_1 weighted MR images corresponding to the concentrations shown in (A), and corresponding TEM images. (C) extinction spectra of both Gd-NM-PEG nanoparticles as denoted in (A), and (D) the calculated longitudinal relaxivity r_1 versus Au shell thickness (green) using SBM theory (a concentration of 2.3×10^5 Gd(III) chelates per NM is used). The blue and red dots are the corresponding experimental relaxivities.132
- Figure 4.14** - (A) Flow cytometry toxicity analysis using SYTOX® red dead cell stain of RAW 264.7 cells after 24 h of incubation with Gd-NM-PEG (green) and Gd-coated-NM (blue). The percentages were calculated considering

the control as 100%. (B) Bright field microscopy and (C) merged confocal and reflectance images of RAW 264.7 macrophage cells showing the nuclei (blue) and Gd-NM-PEG (red). T₁-weighted MR images of (D) reference (phosphate buffer solution (1x PBS)), (E) RAW 267.4 macrophage cells in PBS, and (F) RAW 267.4 macrophage cells with Gd-NM-PEG in PBS. The cell concentration was $\sim 5.2 \times 10^7$ cells/mL. 134

Figure 4.15 - Dependence of MR relaxation on nanoparticle concentration and Gd(III) concentration in phantom: T₁-weighted MR images of reference (water), agarose, and the equivalent number of Gd-NM-PEG (100 μ L of solution)..... 134

LIST OF TABLES

Table 4.1 - T_1 relaxivity for clinically used contrast agents at 0.47 and 1.41 T.	108
Table 4.2 - T_1 relaxivity of Gd(III) conjugated nanomaterials.	111
Table 4.3 - Hydrodynamic diameter of Gd-NM-PEG and GdPEG-coated NM in water and after dispersion in culture media (FBS 10%) measured by dynamic light scattering (DLS).	127

LIST OF ABBREVIATIONS AND ACRONYMS

ALC	aliphatic alcohol free
AMPL	mobile polar lipids in ketone
APTES	3-aminopropyltriethoxysilane
AuNRs	gold nanorods
BBB	blood-brain barrier
BSA	bovine serum albumin
CM	natural cell membrane
CTAB	cetyltrimethylammonium bromide
CV	crystal violet
DIC	differential interference contrast
DLS	dynamic light scattering
DMEM	Dulbecco's Modified Essential Media
DTPA	Gd(III)-diethylenetriamine pentaacetic acid
EDS	energy dispersive spectroscopy
EPR	enhanced permeability and retention
FBS	fetal bovine serum
FEG-SEM	field-emission Scanning Electron Microscopy
FFA	free fatty acids
FID	flame ionization detection
FTIR	Fourier transform infrared spectroscopy
Gd-DOTA-SCN	S-2(4-isothiocyanatobenzyl)-1,4,7,10-tetraazacyclododecane-1,4,7,10-tetraacetic acid
HC	aliphatic hydrocarbons
ICP-MS	inductively coupled plasma mass spectroscopy
MRI	magnetic resonance imaging
MTT	3-(4, 5-dimethylthiazolyl-2)-2, 5-diphenyltetrazolium bromide
NIR	near infrared region
NM	Au nanomaterials
NQO1	NADP(H):quinine oxidoreductase
NSF	nephrogenic system fibrosis
PBS	phosphate buffer saline

PDT	phodynamic therapy
PEG	polyethylene glycol
PL	phospholipids
PLGA	poly(lactic-co-glycolic acid)
PPPT	plasmonic photothermal therapy
RBC	red blood cell membrane
RF	radiofrequency
SBM	Solomon-Bloembergen-Morgan
SDS-PAGE	polyacrylamide gel electrophoresis
SERS	surface enhanced raman scattering
SPR	surface plasmon resonance
ST	sterol
TAG	triglycerides
TEM	transmission electron microscopy
TEOS	tetraethoxysilane
THPC	tetrakis(hydroxymethyl) phosphonium chloride
TLC	thin-layer chromatography
UV-VIS-NIR	ultraviolet-visible-near infrared
WE/SE	ester
β-Lap	β-Lapachone

LIST OF SYMBOLS

ε	dielectric constant for the metal
ε_m	dielectric constant of the surrounding medium
r_0	intrinsic relaxivity
r_1	longitudinal relaxivity
r_2	transverse relaxivity
r^{IS}	inner-sphere contributions to the total relaxivity
r^{OS}	outer-sphere contributions to the total relaxivity
ω_I	proton Larmor angular frequencies
ω_s	electronic Larmor angular frequencies
A	experimental extinction in arbitrary units
a	length of the nanoparticle
b, c	width of the particle
B_0	external magnetic field
C	constant
C_{abs}	cross-sections of absorption
C_{ext}	total extinction
C_{sca}	cross-sections of scattering
d	distance of closest approach of H ₂ O molecules
D	sum of diffusion coefficients of bulk water and of the complex
$j(\omega)$	spectral density function
l	angular moment
l	optical path of the cuvette in cm
M	net magnetization
M_{xy}	transverse magnetization
M_z	longitudinal magnetization
N	concentration of particles (number of particles/mL)
R	aspect ratio (a/b)
T_1	longitudinal relaxation time
T_2	transverse relaxation time
V	unit of volume of the nanoparticle

γ	gyromagnetic ratio
λ	wavelength of light
ω_0	angular frequency
ω_B	plasmon frequency of the bulk metal
$\omega_{c,l}$	plasmon frequency of the cavity
$\omega_{s,l}$	plasmon frequency of the gold sphere

CONTENTS

1	INTRODUCTION AND OBJECTIVES.....	33
2	SYNTHESIS AND CHARACTERIZATION OF PLASMONIC NANOPARTICLES.....	37
2.1	INTRODUCTION	37
2.1.1	Plasmonic nanoparticles	37
2.1.2	Gold nanorods	39
2.1.3	Gold nanoshells and nanomaterials.....	41
2.2	EXPERIMENTAL SECTION.....	45
2.2.1	Materials	45
2.2.2	Gold nanorods (AuNRs) synthesis	45
2.2.3	Gold nanomaterials (NM) synthesis.....	46
2.2.4	Au-coated Au ₂ S nanoshells synthesis.....	47
2.2.5	Characterization Techniques.....	48
2.3	RESULTS AND DISCUSSION.....	48
2.3.1	Gold nanorods synthesis and characterization.....	48
2.3.3	Au-coated Au ₂ S nanoshells.....	55
2.4	CONCLUSIONS	60
3	PLASMONIC GOLD NANORODS COATED WITH CANCER CELL MEMBRANE AS A MULTIFUNCTIONAL SYSTEM FOR CANCER THERAPY	63
3.1	INTRODUCTION	63
3.1.1	Theranostic nanoparticles	63
3.1.2	Plasmonic Photothermal therapy (PPTT).....	64
3.1.3	Combined therapies.....	67
3.1.4	Cell membrane coated nanomaterials	68
3.1.5	Cell membrane vesicles as carriers	70
3.1.6	β -Lapachone.....	71
3.1.7	Toxicity of nanomaterials.....	72
3.2	EXPERIMENTAL SECTION.....	73
3.2.1	Materials	73
3.2.2	Gold nanorods (AuNRs) synthesis	74
3.2.3	Cell culture	74

3.2.4	Extraction of A549 cancer cell membrane (CM)	75
3.2.5	A549 cancer cell membrane (CM) characterization	75
3.2.6	A549 cell membrane-loaded β -lapachone (CM- β -Lap)	76
3.2.7	A549 cell membrane-loaded β -lapachone-coated PEG functionalized gold nanorods (CM- β -Lap-PEG-AuNRs)	77
3.2.8	Photothermal therapy	77
3.2.9	Characterization	78
3.2.10	Isothermal Titration Calorimetry (ITC)	79
3.2.11	Cellular Uptake	80
3.2.12	Cytotoxicity	81
3.2.13	Detection of Intracellular Reactive Oxygen Species (ROS)	82
3.3	RESULTS AND DISCUSSION	82
3.3.1	CM characterization	84
3.3.2	Synthesis of CM- β -Lap-PEG-AuNRs.....	86
3.3.3	Photothermal properties	92
3.3.4	<i>In vitro</i> photothermal therapy.....	95
3.3.5	Cellular uptake	97
3.3.6	Cytotoxicity	101
3.3.7	Detection of Intracellular Reactive Oxygen Species (ROS)	102
3.4	CONCLUSIONS.....	103
4	Gd(III)-ENCAPSULATING AU NANOMATRYOSKHAS: ENHANCED T₁ MAGNETIC RESONANCE CONTRAST IN A THERANOSTIC NANOPARTICLE	105
4.1	INTRODUCTION	105
4.1.1	Magnetic Resonance Imaging (MRI).....	105
4.1.2	Gd(III) based contrast agents	108
4.1.3	Nanostructured T ₁ MRI contrast agents.....	109
4.2	EXPERIMENTAL SECTION	112
4.2.1	Materials.....	112
4.2.3	Gd-embedded Au nanomategyoshkas (Gd-NM) synthesis.....	112
4.2.4	Polyethylene glycol (PEG)-functionalization of Gd-NM (Gd-NM-PEG)	114
4.2.5	GdPEG-coated gold nanomategyoshkas (GdPEG-coated NM) synthesis	114
4.2.6	Calculation of Nanomategyoshkas Concentration	115
4.2.7	Characterization	115

4.2.8	Inductively Coupled Plasma Mass Spectroscopy (ICP-MS)	116
4.2.9	Gd(III) release.....	117
4.2.10	MRI Analysis	117
4.2.11	Cytotoxicity	117
4.2.12	Fluorescence Imaging	118
4.2.13	Preparations of Cells for MRI.....	118
4.2.14	Phantom preparation for MRI.....	119
4.3	RESULTS AND DISCUSSION.....	119
4.4	CONCLUSIONS	135
5	CONCLUSIONS AND PERSPECTIVES.....	137
	REFERENCES	139

1 INTRODUCTION AND OBJECTIVES

Developments in nanomedicine have offered new hope in fighting cancer, one of the leading causes of death worldwide,(1) mainly in the areas of photothermal and gene therapy, drug delivery, and diagnostic imaging.(2-5) In particular, plasmonic gold nanoparticles have received great attention as theranostic agents (that exhibit both diagnostic and therapeutic functions) due to their unique properties, including intense near infrared optical absorption as a result of their strong localized surface plasmon resonance (SPR), *in vivo/in vitro* stability, biocompatibility, and facile surface conjugation chemistry.(5-6)

Plasmonic photothermal therapy (PPPT), which consists in the transduction of light by specific nanosystems into heat, has emerged as a potential minimally invasive alternative for cancer treatment with reduced side effects.(7) The use of long wavelength laser irradiation, such as in the near infrared region (NIR) around 650-950 nm, is particularly advantageous since it has the maximum radiation penetration and can be used in deeply seated targets.(8) Gold nanorods (AuNRs) provide excellent systems for applications in PPTT due to their localized surface plasmon resonance (SPR) at NIR.(9) Recently Halas' group developed tunable plasmonic Au nanomatryoshkas (NM), a metal-based nanoparticle consisting of an Au core, an interstitial nanoscale SiO₂ layer, and an outer Au shell.(10-11) This nanoparticle possesses a strong optical extinction at 800 nm, tunable by varying its geometry if needed, which makes it a highly attractive candidate for photothermal cancer therapy.

However, despite many studies in this area, significant clinical advances have not been observed. One of the main reasons for this failure is the low accumulation rate of the nanoparticles in the target tissue, which depends on their ability to escape the immune system, cross the biological barriers and accumulate at target tissues.(12) Moreover, the ability to determine the precise anatomical location of theranostic nanoparticles in the body, in real time, before, during, and after treatment is important to guarantee their efficiency and safety.(13)

The functionalization of nanoparticles with polyethylene glycol (PEG) has been the gold standard to extend the *in vivo* blood circulation time of the particles and to improve their passive and active accumulation in the tumor.(14) Although much progress has been made, the accumulation in the target region is still low, reducing the therapeutic effects of nanoparticles and increasing the risk of side effects. In addition, some evidences of anti-PEG immunological response have been reported.(15) To overcome the immune system barriers, as

well as to enhance the accumulation of nanoparticles in the tumor, new strategies to functionalize nanomaterials have been developed. Among them, coating with natural cell membranes has been shown to be an interesting alternative to camouflage the particles and extend their blood circulation time. Red blood cell membrane (RBC)-coated polymeric nanoparticles have been shown to present longer blood circulation time compared to the PEG-coated ones.(16) Also, it has been demonstrated that CD47 proteins, a biomolecule capable of inhibiting the phagocytosis, are transferred to the nanoparticle surface and get exposed, allowing the nanomaterials to establish molecular interactions and reducing their susceptibility to be captured by macrophages.(17) Using a cancer cell membrane, it may also be possible to transfer multiple membrane-bound tumor-associated antigens to the nanoparticles surface,(18) which can be particularly useful for applications in cancer cell targeting (18) and immunotherapy.(19) Furthermore, the cell membrane coating may also be explored in drug delivery systems,(20) allowing the fabrication of multifunctional platforms.

To address the challenge of precise location of theranostic nanoparticles in the body, the development of near-infrared resonant, magnetic resonance imaging (MRI) active theranostic nanocomplexes that enhance visualization by mainstream bioimaging techniques is highly desired. MRI is currently the most universally used biomedical imaging modality.(21) It is a non-invasive technique with contrast versatility, high spatial and temporal resolution, that it not used harmful high-energy radiation (22) There are two main types of MRI contrast agents currently in widespread clinical use. T_2 -weighted contrast agents locally modify the spin-spin relaxation process of water protons, producing negative or dark images (based on materials such as superparamagnetic Fe_3O_4 nanoparticles). T_1 -weighted contrast agents affect nearby protons through spin-lattice relaxation, producing positive or bright image contrast (based on paramagnetic materials such as Gd(III) and Mn(II)).(23)

Despite their utility, T_2 contrast agents have several disadvantages that limit their utility in clinical applications. They can cause reduction in the MRI signal, which can be confused with other pathogenic conditions, such as blood clots and endogenous iron. In the case of tumor imaging, they can induce magnetic field perturbations on the protons in neighbor normal tissues, which can make spatially well-resolved diagnosis difficult.(24) In contrast, T_1 contrast agents increase the specificity and sensitivity of MR image. Among the paramagnetic materials useful for T_1 contrast MR imaging, Gd(III) is the most effective contrast agent currently available for clinical use. However, Gd(III) ions exhibit high toxicity in their uncomplexed state and Gd(III)-chelates such as DOTA and DTPA suffer from poor sensitivity, stability, and rapid renal clearance.(22, 25-27) Considerable efforts have been

devoted to the incorporation of Gd(III) onto or into nanoparticles that will enhance their sensitivity by increasing the concentration of Gd(III) per nanocarrier, prolonging imaging time, and reducing their toxicity.(22, 28-32)

Based on the exposed, this thesis explores three main subjects:

In **Chapter 2**, we present a theoretical introduction and describe the synthesis and characterization of three types of gold based-plasmonic nanoparticles: gold nanorods, gold nanomaterials, and gold-coated gold sulfide nanoshells. We explored the dependence of the surface plasmon resonance on parameters such as shape, size and composition. Gold nanorods were synthesized using the seed-mediated method in presence of cetyltrimethylammonium bromide (CTAB). Gold nanomaterials, consisting in a gold core, an interstitial nanoscale silica (SiO_2) layer, and a thin gold shell ($\text{Au/SiO}_2/\text{Au}$) were synthesized with high control of the thickness of the interstitial silica layer and gold shell. For the synthesis of Au-coated Au_2S nanoshells two methods were investigated: one and two step processes. All particles were characterized by electronic microscopy and spectroscopic techniques. The three systems presented strong absorption in the near infrared region and maximum diameter of 100 nm, two desirable characteristics for medical applications. Moreover, their gold surface allows straightforward conjugation of polymers and biomolecules to the nanoparticle surface, which is important to maintain the particle stability and add new functionalities for applications in medicine.

In **Chapter 3**, we developed a multifunctional nanocarrier for photothermal therapy and drug delivery. In this new nanotheranostic system, PEG-coated gold nanorods were grouped into natural cell membrane vesicles from lung cancer cell (A549) membranes and loaded with β -Lapachone (CM- β -lap-PEG-AuNRs). Our goal was to develop specific multifunctional systems for cancer treatment by using the antigens and the unique properties of the cell membrane combined with photothermal properties of AuNRs and anticancer activity of β -lap. We have chosen A549 cell line, because it is a metastatic cancer type and, consequently, may be good candidates to enhance delivery to the tumor and metastatic sites. The platform was characterized by spectroscopic and scanning electron microscopy techniques and its photothermal properties both in suspension and *in vitro* were investigated using a NIR laser. Further, cytotoxicity experiments were performed to evaluate its safety in the absence of laser irradiation.

In **Chapter 4**, we report a modification of gold nanomatryoskas that transforms them into high-relaxivity MRI-active contrast agents as well as highly efficient NIR photothermal transducers for photothermal cancer therapy. This was accomplished by incorporating Gd(III) into the interstitial silica layer of the NM structure. This strategy adds MRI contrast enhancement to the properties of these nanoparticles so they can be used in both bioimaging diagnosis and therapeutic applications. Surprisingly, the sequestration of Gd(III) within the inner layer of the nanoparticle resulted in increased T_1 relaxivities relative to Gd(III)-based chelates currently in widespread use. The enhanced MRI sensitivity is accompanied by reduced toxicity, since the Gd(III) remains sequestered within the nanoparticle. This combination of MRI active contrast within a photothermal therapeutic transducer with superior properties should facilitate MR-based “see and treat” approaches that will enable increased efficiencies and optimization of photothermal therapy treatment protocols of solid tumors. This project was developed at Rice University (advisor: Dr. Naomi Halas) during the International Research Internship (BEPE-DR FAPESP).

2 SYNTHESIS AND CHARACTERIZATION OF PLASMONIC NANOPARTICLES

2.1 INTRODUCTION

2.1.1 Plasmonic nanoparticles

Plasmonic nanoparticles differ from other nanoplatforms such as semiconductor quantum dots, magnetic and polymeric nanostructures by their unique surface plasmon resonance (SPR). When a metal nanoparticle is exposed to the oscillating electromagnetic field of the light, its conduction band electrons undergo a collective coherent oscillation in resonance with the frequency of light.(33) This results in a strongly enhanced absorption and scattering orders of magnitude higher than the absorption and emission of dye molecules.(33-34) The coherent oscillation of the metal free electrons in resonance with the electromagnetic field is the SPR.

The SPR band intensity and wavelength are theoretically described by the Mie theory and depend on several factors affecting the electron charge density on nanoparticle surface such as particle size, shape, metal type, structure, composition, and dielectric constant of the surrounding medium.(35) Consequently, the resonant photon wavelength is different for different metals, sizes and morphologies. A free Mie theory simulator is available at <http://www.nanocomposix.com/support/tools>, and allows the prediction of the extinction spectra for several types of plasmonic nanostructures, including core-shell systems.

The versatility and possibility to design systems with the desired optical properties by manipulating the composition, shape and size allow the use of plasmonic nanostructures for a wide range of applications. For example, plasmonic nanostructures of noble metals, mainly silver and gold, have shown significant promise in the field of photocatalysis for direct conversion of solar to chemical energy.(36-37) They present higher photocatalytic activity compared to other metal structures when exposed to resonant photons of Sun-like intensities. Some examples of the direct photocatalysis of plasmonic nanostructures include exothermic partial oxidation, selective reduction, and organic decomposition reactions on excited plasmonic Ag and Au nanostructures.(36) Plasmonic nanoparticles have also been successfully incorporated into solar cell devices, where they enhance sunlight absorption and, consequently, the conversion of solar energy into electricity. For example, it has been

demonstrated an increased optical absorption and photocurrent in thin film silicon solar cells by the incorporation of silver and gold nanoparticles.(38-39)

Due to the combination of multiple scattering and optical absorption of light, plasmonic nanostructures can heat a reduced fluid volume and may be used for distillation applications.(40) Broadband light-absorbing plasmonic nanoparticles have also been used as solar photothermal heaters for efficient solar autoclave, which could be useful for sanitation of instruments and materials in resource-limited, remote locations.(41) The electron oscillation around the plasmonic particle surface can also modify the emission properties of fluorophores in their proximity, resulting in fluorescence enhancement or quenching.(42-43)

The biomedical field has been greatly benefited with the advances in nanotechnology. Plasmonic nanoparticles have been used as contrast agents for optical imaging because of their efficient light-scattering properties. Gold-based nanoparticles, for example, have been demonstrated to provide high-contrast images of cancer cells using a variety of optical techniques, including dark-field microscopy,(44) reflectance confocal microscopy,(45) one- or two-photon fluorescence imaging,(46) surface enhanced Raman scattering (SERS),(47-48) and photoacoustic imaging.(49) They also have shown interesting properties for use in sensors for detecting different types of targets, such as proteins,(50) specific DNA sequences (51) or cancer cells.(52)

The use of plasmonic nanoparticles as therapeutic agents has also opened new opportunities for alternative treatments. The use of light as an external stimulus in the presence of plasmonic nanoparticles has enabled the conversion of light into heat and applications in efficient treatments, such as plasmonic photothermal therapy (PPTT) (53-54) and light controlled drug release.(55) Besides the advantages of the high stability, the use of plasmonic nanoparticles as photothermal agents has been proved to enhance the efficiency of near infrared (NIR) light absorption, where maximum radiation penetration through tissue occurs,(8) by several orders of magnitude compared to conventional phototherapy agents.(56) Nanomaterials can take advantage of the enhanced permeability and retention effect (EPR), presenting a higher accumulation in tumor sites compared to small molecules agents.(57) The current trends go beyond the use of plasmonic systems as agents for simultaneous diagnostic and therapy, the so-called theranostic systems.

2.1.2 Gold nanorods

Gold-based nanomaterials have become an important alternative for medical applications due to their unique plasmonic properties combined with their potential non-cytotoxicity and chemical/thermal stability.(58) The possibility of obtaining gold nanoparticles in a wide variety of sizes, shapes and functionalizations allows the control of their properties and open a broad range of possibilities for applications in detection and treatment of diseases.(35, 58-59)

Special attention has been focused on rod-shaped gold nanomaterials, called gold nanorods (AuNRs). As predicted by Gan theory in 1915, when the shape of Au nanoparticles change from spheres to rods, the SPR band is split into two bands related to the coherent motion of the conduction band electrons along the long and short axes of the particle.(35, 59-60) The transversal band occurs in the visible region, while the longitudinal band usually occurs in the near infrared region (NIR), which has maximum penetration through tissue,(8) as shown in **Figure 2.1**.

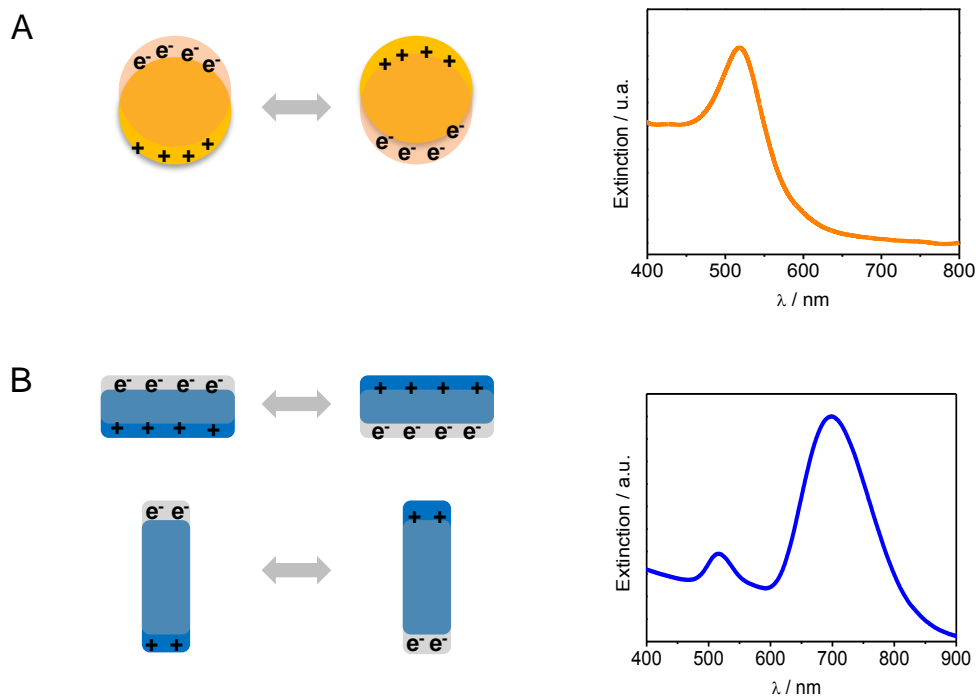


Figure 2.1 - Schematic representation of the SPR oscillation and its respective extinction spectra for gold (A) nanospheres and (B) nanorods.

Source: By the author.

Upon illumination, plasmonic nanoparticles will preferentially scatter or absorb light or a combination of both. In medical applications, scattering is useful for contrast

enhancement in bioimaging, while absorption is desired for photothermal therapy. Quantitative description of the cross-sections of absorption (C_{abs}), scattering (C_{sca}), and total extinction (C_{ext}) for gold nanomaterials are shown in **Equations 2.1, 2.2. and 2.3** according to Gans theory, or Mie-Gans theory, an extension of Mie theory for including spheroidal particles.(33)

$$C_{ext} = C_{abs} + C_{sca} \quad (2.1)$$

$$C_{abs} = \frac{2\pi}{3\lambda} \varepsilon_m^{3/2} V \sum_i \frac{\varepsilon_2 / (n^i)^2}{\left(\varepsilon_1 + \left[\frac{(1-n^i)}{n^i} \right] \varepsilon_m \right)^2 + \varepsilon_2^2} \quad (2.2)$$

$$C_{sca} = \frac{8\pi}{9\lambda^4} \varepsilon_m^2 V^2 \sum_i \frac{(\varepsilon_1 - \varepsilon_m)^2 + \varepsilon_2^2 / (n^i)^2}{\left(\varepsilon_1 + \left[\frac{(1-n^i)}{n^i} \right] \varepsilon_m \right)^2 + \varepsilon_2^2} \quad (2.3)$$

Where λ is the wavelength of light, V is the unit of volume of the nanoparticle, ε_m is the dielectric constant of the surrounding medium, and ε is the dielectric constant of the metal given by $\varepsilon = \varepsilon_1 + i\varepsilon_2$ (ε_1 and ε_2 are the real and imaginary components of the dielectric constant, respectively).(33) Finally, n^i is the depolarization factor defined by:(33)

$$n^a = \frac{2}{R^2 - 1} \left(\frac{R}{2\sqrt{R^2 - 1}} \ln \frac{R + \sqrt{R^2 - 1}}{R - \sqrt{R^2 - 1}} - 1 \right) \quad (2.4)$$

$$n^b = n^c = \frac{(1-n^a)}{2} \quad (2.5)$$

Where a, b, and c are the three axes of the particle, $a > b = c$, and R is the aspect ratio a/b . For spheres, $n^i = 1/3$, resulting in only one SPR band. The SPR occurs when $\varepsilon_1 = -(1 - n^i) \times \varepsilon_m / n^i$ where $i = a$ for the longitudinal and $i = b, c$ for the transverse resonance.(33)

The equations show that the SPR depends not only on the wavelength of the light, but also on the dielectric constant of the surrounding medium as well as some characteristics of the particle such as dielectric constant, size and aspect ratio. Link et al found a linear

relationship between the longitudinal SPR absorption maximum and the aspect ratio of nanorods:(61-62)

$$\lambda_{max} = (53.71 \times R - 42.29)\varepsilon_m + 495.14 \quad (2.6)$$

In aqueous solution ($\varepsilon_m = 1.77$), the equation can be written as following:

$$\lambda_{max} = 95.07 \times R + 420.29 \quad (2.7)$$

The C_{ext} (in cm^2) can be related to Beer-Lambert's law and can be used to calculate the concentration according to **Equation 2.8**. For gold nanorods with aspect ratio around 3 ($a \sim 49$ and $b \sim 16$ nm) the extinction cross section (C_{ext}) of the longitudinal band is around $5 \times 10^{-12} \text{ cm}^2$, while for an aspect ratio of about 3.33 ($a \sim 50$ nm and $b \sim 15$ nm) is $8.4 \times 10^{-12} \text{ cm}^2$.(63)

$$N = \frac{2.303 \times A}{C_{ext} \times l} \quad (2.8)$$

Where N is the concentration of particles (number of particles/mL), A is the experimental extinction in arbitrary units, and l is the optical path of the cuvette in cm. The C_{ext} (in cm^2) can also be related to the coefficient of extinction from Beer-Lambert's law:

$$\varepsilon (M^{-1} \text{ cm}^{-1}) = \frac{10^{-3} N C_{ext}}{2.303} \quad (2.9)$$

2.1.3 Gold nanoshells and nanomatryoshkas

Recent advances in the chemical synthesis of nanomaterials have led to the fabrication of multilayered nanostructures, a unique and important class of nanomaterials of intense technological interest due to their ability to manipulate light. In particular, gold nanoshells, consisting of a silica nanoparticle core surrounded by a thin gold shell layer (SiO_2/Au), have offered exciting potential for applications in a broad range of spectroscopic, photonic, and biomedical applications.(42,47-48,64-66) A schematic of the gold nanoshell and a

representative UV-VIS-NIR spectrum are shown on **Figure 2.2**. Their surface plasmon resonance can be tuned to the near-infrared region by changing the thickness of the gold layer. The shoulder around 600 nm is an indicative of the complete gold shell layer formation.(67)

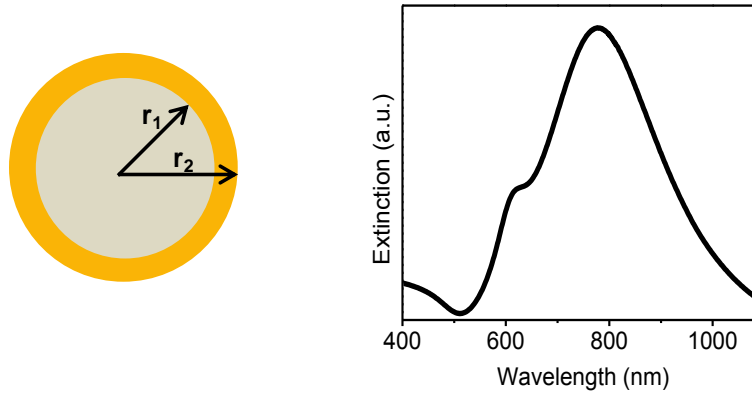


Figure 2.2 - Schematic representation of a gold nanoshell and a representative extinction spectrum for a $[r_1, r_2] = [62, 76]$ nm.
Source: By the author.

For simple gold nanostructures, the absorption and scattering efficiencies depend mainly on nanoparticles size and shape, as described previously. For layered systems, this relationship becomes more complex and geometry dependent.(67) The tunable optical properties of gold nanoshells have been explained by the plasmon hybridization model.(68) This theory deconstructs a complex structure into two elementary structures and analyses the interactions between the individual plasmons in the hybridized structure.(68)

As discussed earlier, Mie theory predicts the extinction spectra of plasmonic systems, and, consequently, their plasmon resonance frequency. For a gold sphere and sphere cavity, the plasmon resonance frequencies predicted from Mie theory can be described as:

$$\omega_{s,l} = \omega_B \left(\frac{l}{2l+1} \right)^{1/2} \quad (2.10)$$

$$\omega_{c,l} = \omega_B \left(\frac{l+1}{2l+1} \right)^{1/2} \quad (2.11)$$

Where $\omega_{s,l}$ and $\omega_{c,l}$ are the plasmon frequencies of the gold sphere and cavity, respectively; ω_B is the plasmon frequency of the bulk metal, and l is the angular moment. The oscillation of

the conduction band electrons in the inner and outer surfaces of the gold shell results in the hybridization of the cavity and sphere plasmons (**Figure 2.3**).

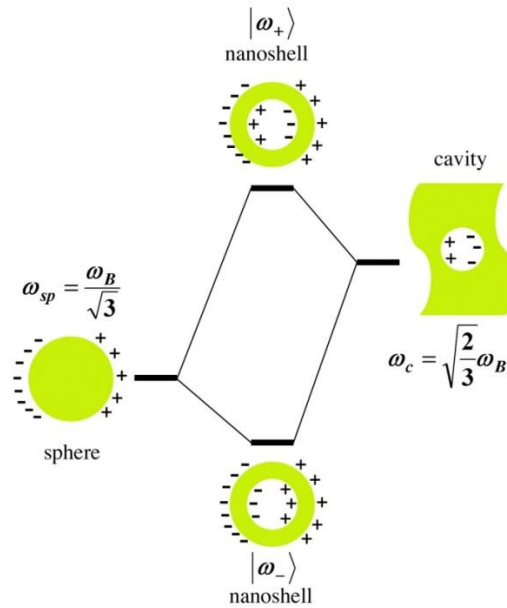


Figure 2.3 - Schematic energy-level diagram describing the plasmon hybridization in gold nanoshells resulting from the interaction between the sphere and cavity plasmons

Source: PRODAN et al.(68)

Prodan et al showed that the interaction of the plasmons on the inner and outer surfaces of the shell gives rise to two hybridized plasmon modes $|\omega_+\rangle$ and $|\omega_-\rangle$ for each $l > 0$, which corresponds to the antisymmetric and symmetric coupling between the two modes, and can be described as:(68)

$$\omega_{l\pm}^2 = \frac{\omega_B^2}{2} \left\{ 1 \pm \frac{1}{2l+1} \left[1 + 4l(l+1) \left(\frac{r_1}{r_2} \right)^{2l+1} \right]^{1/2} \right\} \quad (2.12)$$

From the equation, it is clear that the coupling depends on the ratio r_1/r_2 , which corresponds to the radius of the silica core and entire particle (**Figure 2.2**), and explains the tunable optical properties of gold nanoshells. Consequently, the strength of the coupling between the cavity and sphere plasmon depends on the thickness of the gold shell, i.e., decreasing of the gold shell thickness results in a shift to lower energy of the plasmon resonance.(68) This plasmon hybridization theory can also be extended to understand the plasmon response of more complex metallic nanostructures, such as dimers or nanoparticle

assemblies. As shown previously for gold nanorods, the extinction cross-sections and the respective absorption and scattering cross section of gold nanoshells can also be derived from Mie theory, and be used for determination of particle concentration (**Equation 2.8**). In this case, we have to consider that the particle consist of three regions with distinct dielectric properties: the silica core, the gold shell, and the surrounding medium.(69)

Although many successful applications have been achieved with gold nanoshells,(7) their 150 nm diameter range necessary to have a good NIR activity may limit some of their biomedical applications.(10) Au-coated Au_2S nanoshells present a configuration similar to Au-coated SiO_2 nanoshells, i.e., a dielectric core coated with a metal shell, but usually with a diameter around 50 nm. Analogously to gold nanoshells, this system also present a shift in the plasmon resonance band to NIR, and therefore are of technological interest for many applications.(70)

Recently, multilayered gold nanoparticles, consisting of a gold core, an interstitial nanoscale SiO_2 layer, and a thin gold shell layer ($\text{Au/SiO}_2/\text{Au}$) have offered the possibility to achieve NIR plasmon resonances in the sub-100 nm size range (**Figure 2.4**).(10,53) They were called nanomatyoshka in analogy to matryoshka dolls, and similarly to gold nanoshells, the hydridization theory has been used to explain the optical properties of gold nanomatyoshkas. According to Bardhan et al, the strong coupling between the plasmons supported by the gold core and the gold shell allows the tuning of the plasmon resonance to the NIR region in particles with smaller dimensions than the gold nanoshell.(67)

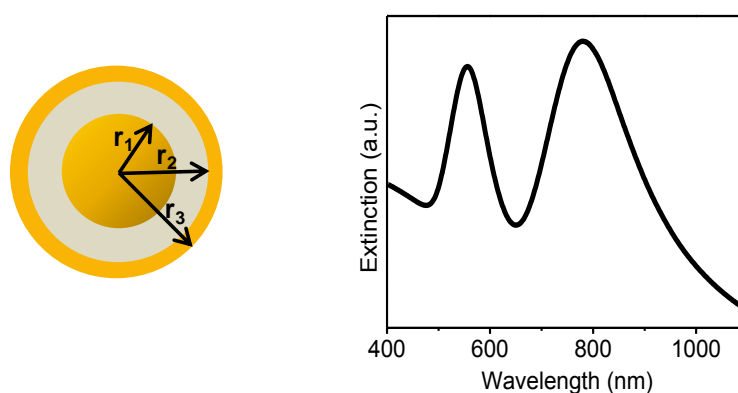


Figure 2.4 - Schematic representation of a gold nanomatyoshka and a representative extinction spectrum for a $[r_1, r_2, r_3] = [24, 34, 44]$ nm.

Source: By the author.

The optical properties of gold nanomatyoshkas (NM) can be tuned by modifying the relative radius (r_1 , r_2 , and r_3) in the particle.(67) For example, maintaining the particle size, an

increase in the gold core diameter and a decrease in the silica layer thickness increase the coupling between the core and shell, resulting in higher absorption efficiency.(67) These properties make them extremely versatile and promising for a broad range of optical and biomedical applications. Besides the biocompatibility, and facile surface conjugation chemistry,(71) this system has shown several advantages compared to others NIR photothermal transducers. Ayala-Orozco et al. demonstrated a 4–5 fold increase in nanomaterial uptake by a triple negative breast tumor model, and consequently nanomaterials presented an improved photothermal therapy efficacy.(53) They attributed this enhancement to a more suitable diameter of nanomaterials (~100 nm) when compared to nanoshells (~150 nm).

2.2 EXPERIMENTAL SECTION

2.2.1 Materials

All reagents were of analytical grade and were used without further purification. The solutions were prepared using ultrapure water (18.2 MΩ cm) and the glassware were cleaned with aqua regia and thoroughly washed with distilled and Milli-Q water. Cetyltrimethylammonium bromide (CTAB), silver nitrate (AgNO₃), tetrachloroauric acid (HAuCl₄), sodium borohydride (NaBH₄) and ascorbic acid were purchased from Sigma-Aldrich. Tetraethoxysilane (TEOS) and 3-aminopropyltriethoxysilane (APTES) were purchased from Gelest. Tetrakis(hydroxymethyl) phosphonium chloride (THPC), chloroauric acid (HAuCl₄·3H₂O, and Na₂S were purchased from Sigma Aldrich; anhydrous potassium carbonate (K₂CO₃) from Fisher, NaOH from Fisher. 50 nm gold colloid citrate NanoXact was purchased from NanoComposix and 200 proof ethanol was purchased from KOPTEC.

2.2.2 Gold nanorods (AuNR) synthesis

Gold nanorods (AuNRs) were synthesized by the seed-mediated method in the presence of the surfactant CTAB.(72) The seeds were prepared by adding 250 μL of HAuCl₄·3H₂O 0.01 mol L⁻¹ in 7.5 mL of CTAB aqueous solution 0.1 mol L⁻¹ under gentle stirring. Next, 600 μL of iced cold NaBH₄ 0.1 mol L⁻¹ was added and the system was kept under vigorous stirring for 10 min. The color of the solution changed from yellow to pale

brown. The solution was kept at 25°C for about 2 hours before using. The final concentrations of the reagents in the final growth solution were adjusted to obtain gold nanorods with different aspect ratios. Briefly, between 3 - 4 mL of 0.01 mol L⁻¹ HAuCl₄·3H₂O were mixed with 47.5 mL of 0.1 mol L⁻¹ CTAB aqueous solution, followed by addition of different amount (300-600 µL) of 0.01 mol L⁻¹ AgNO₃ and 480 µL of 0.01 mol L⁻¹ ascorbic acid solutions. The color of the system changed from dark yellow to transparent, indicating the reduction of Au³⁺ to Au⁺. Finally, different amounts of the seed solution (between 70-100 µL) previously prepared were added and the system was kept under gentle stirring for 20 min. The system was left at room temperature and protected from light for 4 h, and the supernatant was washed by centrifugation twice at 9000 g for 5 min (Spinlab SL-5GR).

2.2.3 Gold nanomatrixoskas (NM) synthesis

Gold nanomatrixoskas (NM) were synthesized by improving a previously Halas group's reported method.⁽¹⁰⁾ Briefly, 21 mL of 0.05 mg/mL 50 nm gold colloid were mixed with 180 mL of 200 proof ethanol, 1.8 mL of 28-30% ammonium hydroxide, 36 µL 10% TEOS solution in ethanol, and 36 µL of 10% APTES in ethanol solution. The reaction was allowed to proceed for 65 min at room temperature under vigorous stirring and then stored in the refrigerator at 4°C for 22 hours. After that, the Au/SiO₂ nanoparticle suspension was dialyzed in 200 proof ethanol for about 16 hours at room temperature. The nanoparticle suspension was cooled to 4°C, centrifuged at 1500 rcf for 35 min and re-dispersed by sonication in a total volume of about 3 mL of ethanol. The Au/SiO₂/Au nanoparticles were prepared by decorating the silica coated nanoparticles with small gold colloid (2-3 nm) fabricated by the method reported by Duff *et al.*⁽⁷³⁾ Briefly, Duff colloids were prepared by mixing 2.4 mL of 1 mol L⁻¹ NaOH and 8 mL of 1.2 mmol L⁻¹ aqueous THPC solution in 360 mL of Milli-Q water. After stirring for 5 min, 13.5 mL of 1% (m/v) HAuCl₄ were added and the solution immediately turned brown. The final Duff colloids were refrigerated for 1 week before use. Next, 1 mL of Au/SiO₂ nanoparticles was mixed with 600 µL of 1 M NaCl and 40 mL of Duff gold colloid (1-2 nm). The precursor particles were left unperturbed for 24 h at room temperature, followed by sonication and centrifugation (950 g, 30 min) to remove the excess of Duff gold colloid. The pellet was dispersed in 2 mL of Milli-Q water and centrifuged two more times at 800 g for 20 minutes. The final precipitate was dispersed in 500 µL Milli-Q H₂O and it is called the seeded precursor. The formation of a continuous metallic

shell around the seeded precursor was performed by mixing 3 mL of plating solution (1% HAuCl_4 - K_2CO_3 solution previously prepared) with 20-40 μL of the seeded precursor and 15 μL of formaldehyde, under a fast shaking for 1 minute. The color of the solution changed from reddish to purple upon the formation of the gold outer shell.

2.2.4 Au-coated Au_2S nanoshell synthesis

One- step synthesis: The synthesis was performed by mixing HAuCl_4 and Na_2S according to an improvement of a previously reported method.(70, 74) Different ratios of HAuCl_4 and Na_2S were tested and the one that gave the best NIR absorption was chosen for the following experiments. In this case, 10 mL of HAuCl_4 2 mmol L^{-1} were mixed with 18 mL of Na_2S 1 mmol L^{-1} , and the system was kept protected from light for 12 hours. The particles were then centrifuged at 200 g for 30 minutes in a 50 mL centrifuge tube containing 14 mL, and resuspended in Milli-Q water.

The separation of the Au-coated Au_2S nanoshells from the plates was carried out in a density gradient according to a previously reported method.(75) For this, 10, 20, 30, 40, 50, and 60 % w/v aqueous solutions of OptiPrep Density Gradient Medium (Sigma-Aldrich) were prepared and carefully placed in a 50 mL centrifuge tube from the most to the least dense (5 mL of each one). The nanoparticles were then placed at the top of the gradient and the system was centrifuged at 22000 g at 23°C for 15 min using a Beckman Coulter Optima L-90k Ultracentrifuge with a SW32 rotor (Swinging Bucket). Finally, the fractions were collected, and each individual fraction was purified by centrifugation and resuspended in Milli-Q water. The fractions were characterized by UV-VIS-NIR spectroscopy and Transmission Electron microscopy (TEM).

Two-step synthesis: First, small gold sulfide (Au_2S) nanoparticles were synthesized by modification of a previously reported method.(76) For this, 5 mL of HAuCl_4 2 mmol L^{-1} were mixed with 100 μL of NaOH 3 mol L^{-1} solution. The solution became immediately colorless indicating the reduction of Au^{3+} to Au^+ . Next, 6 mL of Na_2S 1 mmol L^{-1} were added and the solution became yellowish-brown after one hour, demonstrating the formation of the Au_2S nanoparticles. The second step consisted in the fabrication of the gold shell around the Au_2S particles. We used a procedure similar to that used for fabrication of the Au shell of the gold nanomatryoshkas was employed. In this case, the Au_2S nanoparticles were used as

seeded precursor and the formation of a continuous metallic shell was performed by mixing 3 mL of plating solution (1% HAuCl_4 - K_2CO_3 solution previously prepared) with 100-250 μL of Au_2S nanoparticles, followed by 15 μL of formaldehyde under a fast shaking for 1 min. The color of the solution changed from yellowish-brown to purplish or greenish upon the formation of the gold outer shell and depended on the volume used.

2.2.5 Characterization Techniques

Ultraviolet–visible–near infrared (UV–VIS–NIR) spectroscopy was used to evaluate the optical properties of the nanomaterials. The measurements were carried out on Hitachi U-2900 spectrometer using a 1 cm quartz cell.

Transmission Electron Microscopy (TEM) is an important technique for directly imaging nanomaterials, allowing quantitative measurements of size, distribution and morphology. The images were taken in a JEOL JEM-2100 at 200 kV (LNano, CNPEM, Campinas-SP) or a JEOL 1230 operating at 80 kV (Rice University). For this, one drop of each diluted sample was deposited on a carbon film copper grid 300 mesh (Ted Pella, Inc.) and dried at room temperature. High Resolution TEM coupled with energy dispersive spectroscopy (EDS) was used to obtain the local elemental composition of the Au-coated Au_2S nanoshells.

2.3 RESULTS AND DISCUSSION

2.3.1 Gold nanorod synthesis and characterization

Gold nanorods (AuNRs) were synthesized by the seed-mediated method in presence of the surfactant CTAB,(72) and an overview of the procedure is illustrated in **Figure 2.5**. Small gold nanoparticles (seeds) were initially prepared by rapid reduction of Au^{3+} in presence of CTAB (**Figure 2.5A**). The characterization of the seeds is shown in **Figure 2.6**. From the UV-VIS-NIR spectrum, it is possible to observe a low-intensity band at 515 nm, typical of very small gold nanoparticles.(77) The diameter measured by dynamic light scattering (DLS) and transmission electron microscopy (TEM) image reveals particles with an average diameter of about 2 nm (**Figure 2.6B-C**).

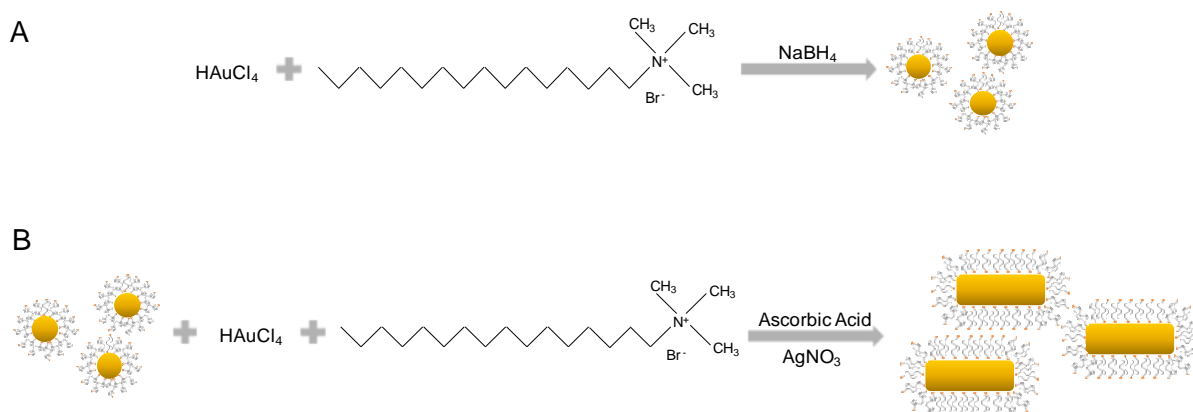


Figure 2.5 - Schematic representation of the gold nanorod synthesis process. (A) First, small gold nanoparticles are synthesized in the presence of CTAB, and (B) used as seeds for the growth of the nanorods.
Source: By the author.

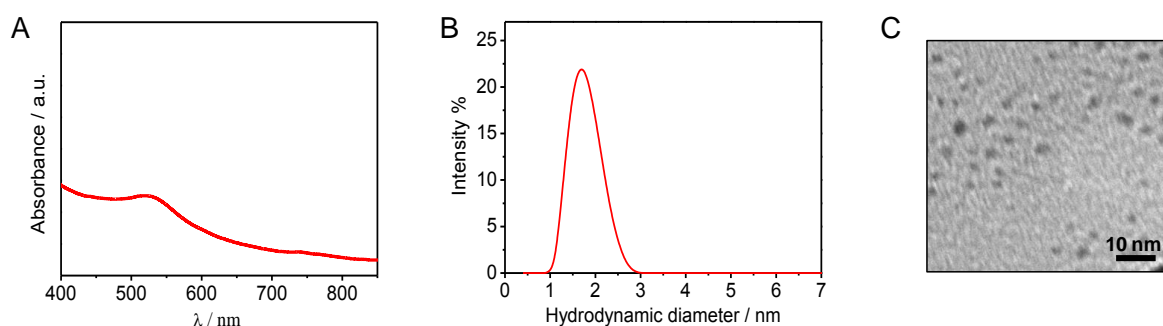


Figure 2.6 - Characterization of the seeds: (A) UV-VIS-NIR spectrum, (B) Hydrodynamic diameter obtained from Dynamic Light Scattering measurements, and (C) TEM image, showing very small particles.
Source: By the author.

Next, the small gold particles were used as seeds for the anisotropic growth (**Figure 2.5B**). **Figure 2.7A** shows the growth kinetics of nanorods monitored by UV-VIS-NIR spectroscopy. The spectrum is typical of AuNRs, which exhibit two surface plasmon resonances (SPR): one around 500 nm due the coherent motion of the conduction band electrons along short axes (transversal band), and the other at higher wavelengths corresponding to the oscillation along long axes of the particle (longitudinal band).^(35, 59, 60) As it can be observed, the longitudinal plasmon band appears in the first minutes and its intensity increases with the time and becomes blue shifted. This shift of the longitudinal band is related to the modification of the aspect ratio during the growth process,⁽⁷²⁾ and after about 40-50 min, the reaction is almost complete (**Figure 2.7B**).

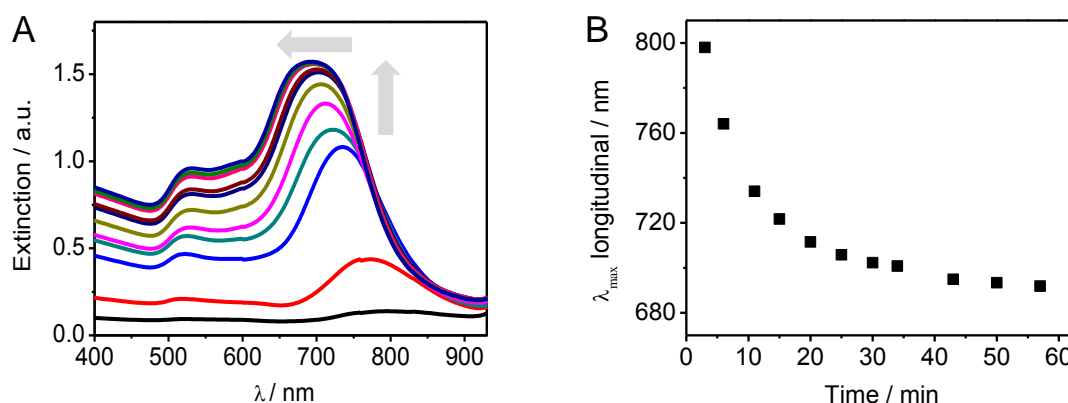


Figure 2.7 - (A) UV-VIS-NIR spectra showing the growth kinetics of nanorods after addition of 100 μL of seeds into the growth solution, and (B) the changing in the maximal wavelength of the longitudinal band as function of time.

Source: By the author.

Figure 2.8 shows the UV-VIS-NIR spectra and their correspondent TEM images of AuNRs obtained using different amount of AgNO_3 . In all cases, we used 100 μL of seed suspension. It is clear that the silver salt plays a significant role in the growth of the nanorods. Higher silver nitrate concentration yields higher aspect ratios (length/width). It is interesting to note that a small variation on the gold nanorods size is enough to cause a significant shift in the longitudinal plasmon band. **Figure 2.9** displays low-magnification TEM images of AuNRs with maximal longitudinal wavelength at 700 nm, revealing a very homogeneous system.

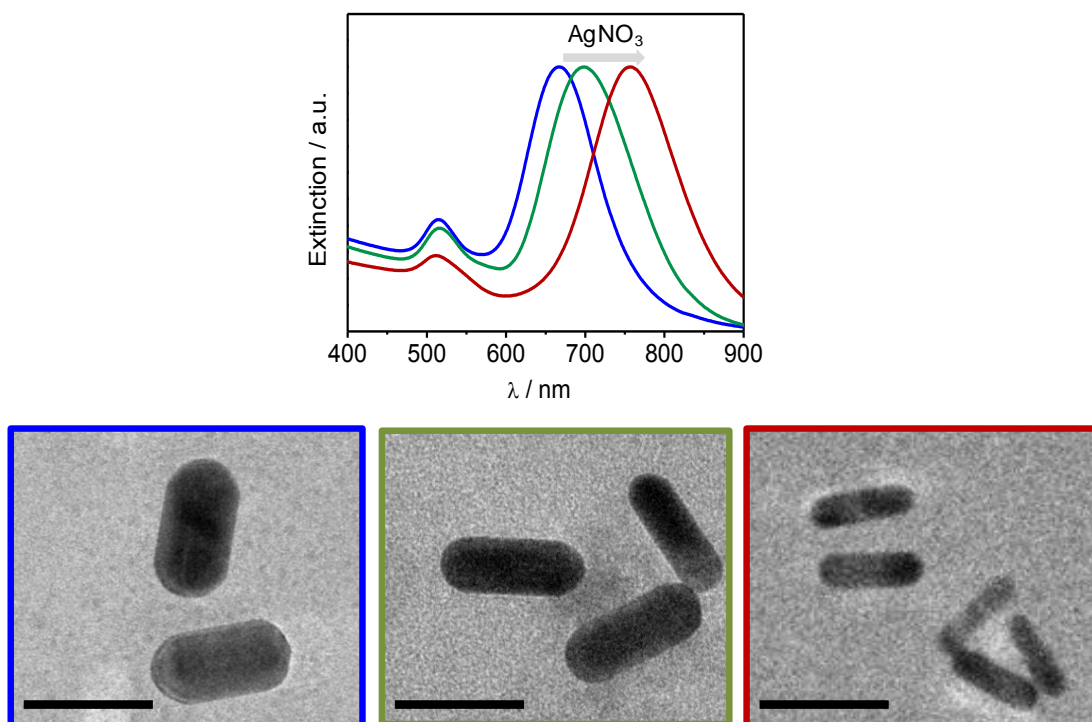


Figure 2.8 - UV-VIS-NIR spectra of AuNRs obtained using different amount of AgNO₃ and the respective TEM images. The aspect ratio are 2.1, 2.8, and 3.5 for blue, green, and red, respectively. Scale bar = 50 nm.

Source: By the author.

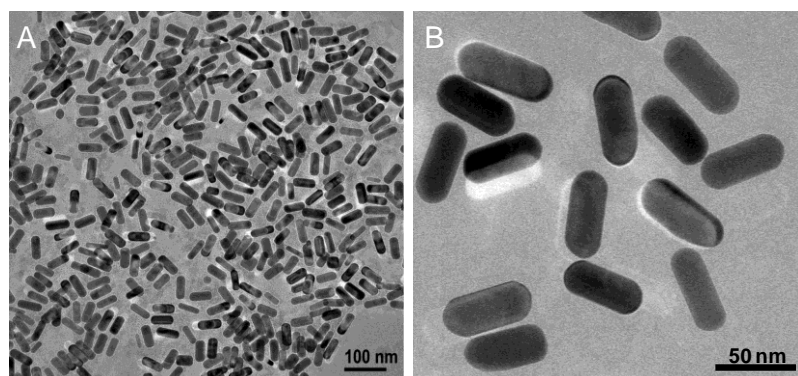


Figure 2.9 - TEM images of the gold nanorods with maximal longitudinal absorption at 700 nm, showing a monodisperse system.

Source: By the author.

We have observed in our experiments and other authors have also reported that the use of AgNO₃ produces not only higher aspect ratio nanorods, but also increases the yield of the reaction.⁽³⁵⁾ In other words, when AgNO₃ is not used in the seed-mediated method, the resulting suspension presents a large amount of spherical gold particles. The mechanism of Ag⁺ ions in the nanorods synthesis has been widely investigated in the last years. It is known

that the silver ions are not reduced in the synthesis conditions, since the ascorbic acid could only reduce the silver in a high pH, which is not the case.(35, 78) Sal et al. proposed that AgNO_3 forms AgBr in the presence of CTAB, which in turn adsorbs differentially in the faces of gold seeds, restricting the growth in one direction.(72) Another study suggest that Ag^+ ions decrease the rate of growth and increase the energy in the sides (110) of monocrystalline gold nanorods, i.e., the ions adsorb preferentially in the sides with specific structures and direct the anisotropic growth.(79) Nikoobakht et al proposed that AgBr decreases the charge density and, consequently, the repulsion between the polar headgroups of CTAB resulting in a template for the growth in that direction.(78)

Recently, a detailed investigation of the mechanism of the anisotropic growth of the gold nanorods by direct observations in the atomic scale using electronic microscopy has been reported.(80) According to the paper, the seeds prepared in presence of CTAB have a cuboctahedral morphology, bound by symmetrically arranged (111) and (100) surfaces. Initially, when these seeds are introduced in the growth solution, they grow isotropically until 4-6 nm in diameter. Then, small truncating surfaces consisting of a few atoms start to form nonuniformly at the intersection of (111) facets. These truncations are a more open atomic structure than the comparatively close-packed (111) and (100) surfaces already present in the nanoparticle, and consequently are potentially preferred sites for Ag^+ underpotential deposition, preventing further Au deposition and resulting in the onedirectional growth.

The aspect ratio may also be controlled by changing the amount of seeds in the growth media and keeping the AgNO_3 amount constant (**Figure 2.10**). As the number of seeds in the media increases, the longitudinal wavelength increases to higher wavelength. However, particles with absorption at higher wavelengths could not be fabricated, which highlights the importance of silver nitrate, especially for high aspect ratio AuNRs.

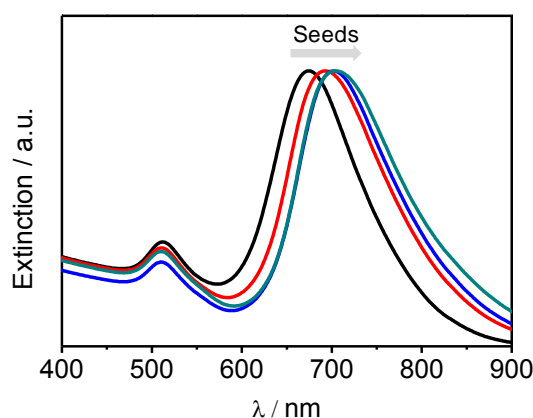


Figure 2.10 - UV-VIS-NIR spectra of gold nanorods prepared with different concentrations of seeds.
Source: By the author.

2.3.2 Gold nanomategyoshkas synthesis and characterization

Gold nanomategyoshkas (NM) were fabricated as shown in **Figure 2.11**. Gold nanoparticles of radius 50 ± 4 nm were initially coated with a ~ 21 nm amorphous silica layer doped with (3-aminopropyl)triethoxysilane (APTES). The SiO_2 layer were growth based on the Stöber method, a condensation reaction of tetraethyl orthosilicate (TEOS) catalyzed by ammonium hydroxide in ethanol:water mixture.(81) The function of the APTES is to introduce amine groups, which in turn will allow the attaching of small gold colloids (2-3 nm diameter) onto the surface of the silica layer in the next step. The small gold colloids were prepared in a separate reaction using tetrakis (hydroxymethyl)phosphonium (THPC) as a reducing agent following the method reported by Duff et. al.(73) To make the complete shell, the SiO_2 -coated gold nanoparticles decorated with Duff colloids, called seeded precursor, were added to the right volume ratio of Au^{3+} aqueous solution containing potassium carbonate (plating solution). Finally, formaldehyde is added under vigorous stirring to reduce the Au^{3+} to metallic gold which grows onto the Duff colloids to form a complete Au layer, ie, the Duff colloids serve as nucleation sites for the formation of Au shell layer.

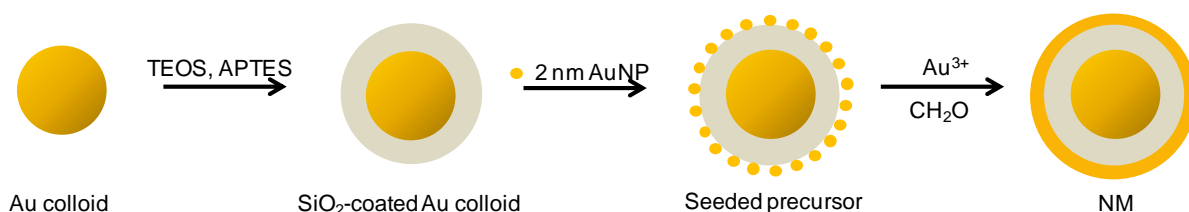


Figure 2.11 - (A) Schematic representation of the gold nanomategyoshka synthesis: 50 nm diameter gold colloids are coated with SiO_2 -APTES shell, followed by a continuous gold shell.

Source: By the author.

The extinction spectra and their respective TEM images corresponding to three stages of the synthesis are shown on **Figure 2.12**. We can see that the resulting nanomategyoshkas present average dimensions of $[r_1, r_2, r_3] = [25, 38, 53]$ nm and plasmon resonance band around 800 nm, which is highly desired for photothermal therapy applications because of the maximum penetration depth of light in biological tissue.(8) The critical step in the synthesis was to obtain the right silica layer thickness to guarantee a controlled hybridized plasmon resonance and consequently the absorption at the desired wavelength. Nanomategyoshkas with different gold shell thicknesses can be fabricated by varying the volume ratio of the seeded precursors and the plating solution. By increasing the seeded precursor from 30 to 34 μL , it resulted in a thinner gold shell and red-shifting of the plasmon resonance (**Figure 2.13**).

However, when the volume of seeded precursor was increased to 40 μL , plasmon resonance band did not change anymore, instead the peak around 600 nm increases, indicating that the amount of seeds was too high, and some NM with incomplete Au shell layer starts to form.

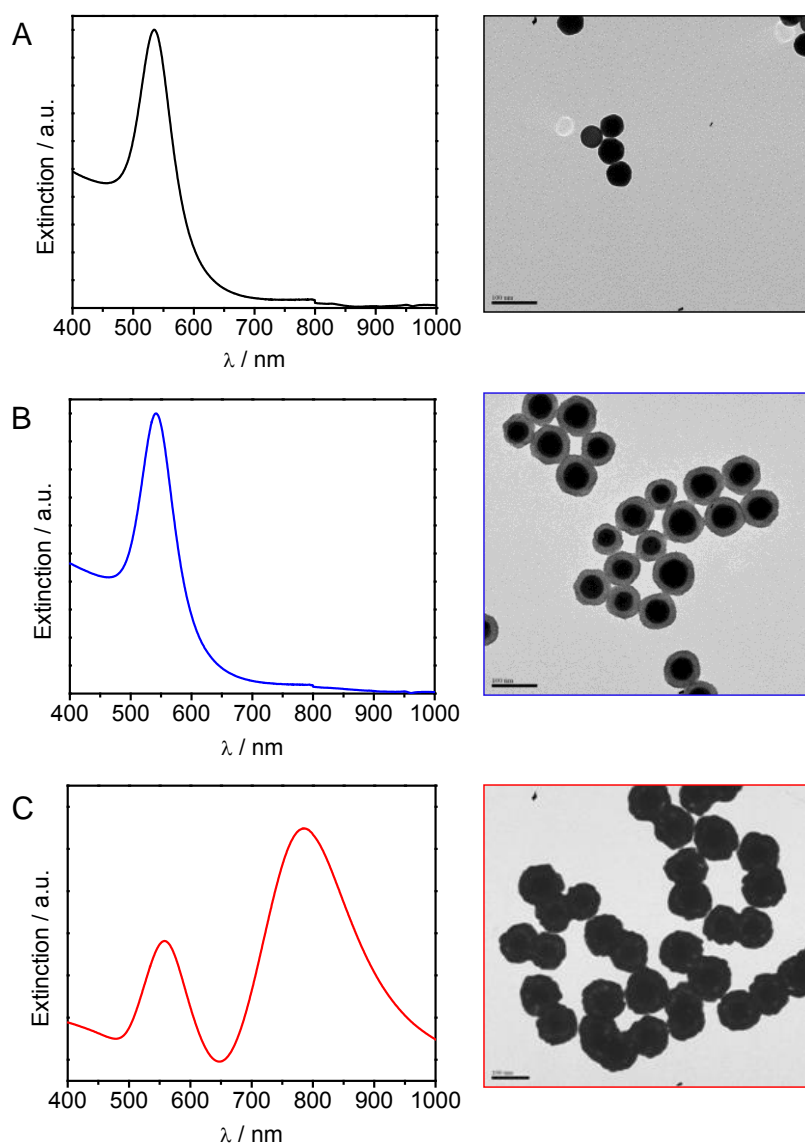


Figure 2.12 - UV-VIS-NIR extinction spectra and their respective TEM images corresponding to (A) Au colloids of about 50 nm, (B) APTES-SiO₂-coated Au colloids, and (C) gold nanomatryoskas.
Source: By the author.

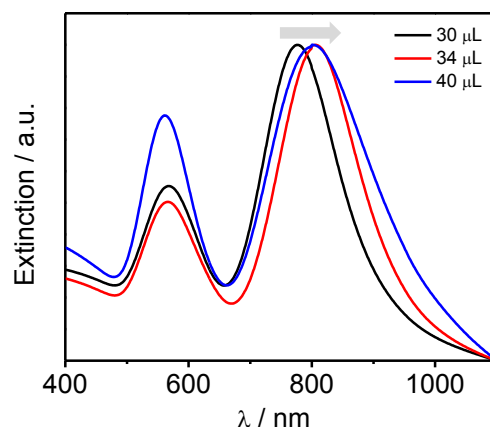
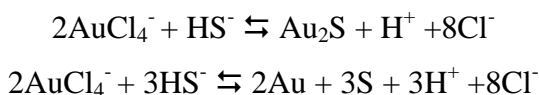


Figure 2.13 - UV-VIS-NIR spectra of gold nanomaterials obtained using different amount of seeded precursor.

Source: By the author.

2.3.3 Au-coated Au₂S nanoshells

Au-coated Au₂S nanoshells were initially prepared according to a previous reported one step method.(70, 74) Averitt et al proposed the following reaction for the reduction process leading to the growth of Au-coated Au₂S nanoshells:(74)



According to the reaction, Au and S will be available for subsequent nucleation and growth, and since the synthesis is performed in one step, it is believed that both Au and Au-coated Au₂S nanoshells grow simultaneously. **Figure 2.14** shows the UV-VIS-NIR spectrum and the respective TEM image. The absorption peak at 520 nm is due to the plasmon resonance of gold colloid, while the second peak has been attributed to the Au-coated Au₂S nanoshells.(70, 74) Au-coated Au₂S nanoshells prepared by this method presented an average diameter of 40 nm. However, the TEM images revealed the presence of not only Au-coated Au₂S nanoshells but also triangular plates. The local atomic composition of the nanoshells and triangular plates were analyzed by High Resolution TEM coupled with energy dispersive spectroscopy (EDS) (**Figure 2.15**). The Figure shows the TEM image and the respective localization of the EDS analysis for Au-coated Au₂S nanoshells and the triangular plates. The column plots correspond to the percentage calculation from the EDS spectrum. The results

show that the spheres are composed by both Au and S, in a proportion suitable for a Au-coated Au_2S , while the triangular plates are only constituted by gold.

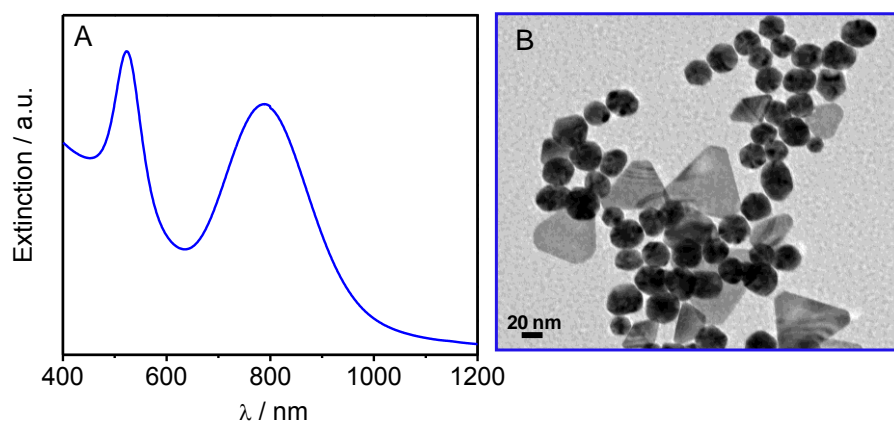


Figure 2.14 - UV-VIS-NIR spectrum of Au-coated Au_2S nanoshells and its respective TEM image.
Source: By the author.

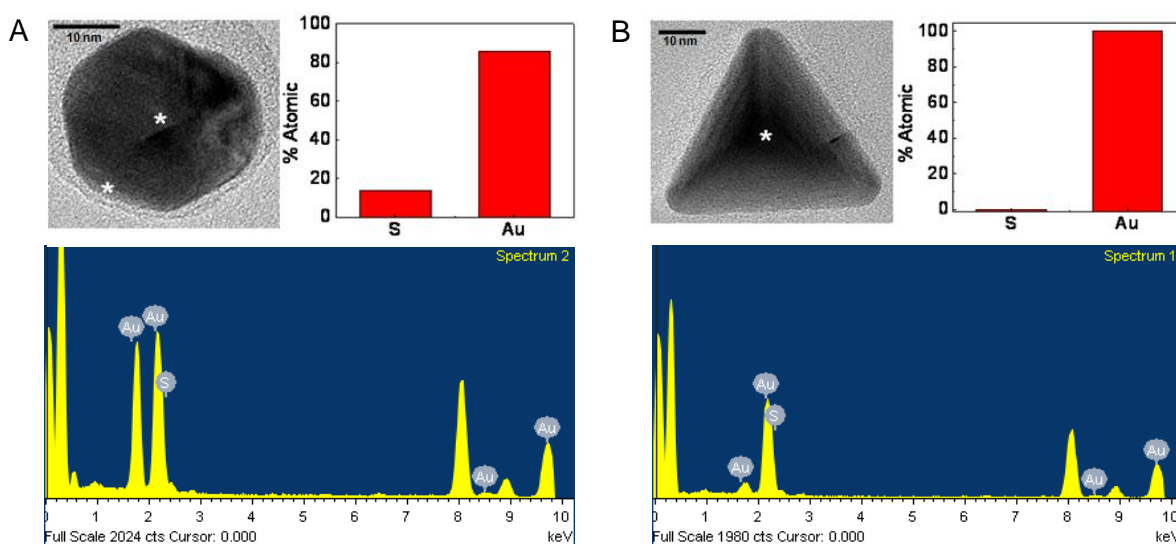


Figure 2.15 - Analysis of the composition of the (A) nanoshells and (B) triangular plates by High Resolution TEM coupled with energy dispersive spectroscopy (EDS).
Source: By the author.

The nanoshells were separated from the plates by a density gradient according to a previously reported method.⁽⁷⁵⁾ Density gradient methods have been shown to be a simple and effective way to separate nanomaterials with different size and shapes.⁽⁸²⁾ **Figure 2.16** shows the pictures of the gradient before and after centrifugation and the TEM images and the respective UV-VIS-NIR spectrum of the two indicated fractions. As it can be seen, the triangular plates are more concentrated in the denser fraction, while the less dense one is

constituted mostly by spherical particles. The UV-VIS-NIR also revealed significant difference between the optical properties of both systems. Although a good separation had been obtained, the difficult to remove the density gradient solution from the nanoparticles has led to the aggregation of the system, limiting their biomedical applications.

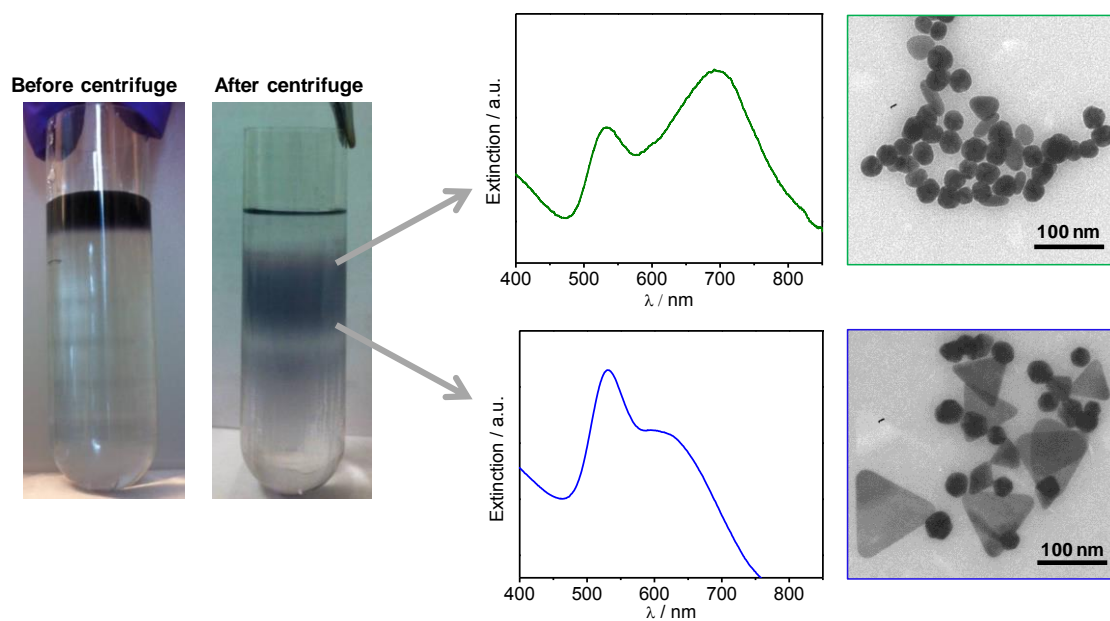


Figure 2.16 - Pictures of the centrifuge tubes before and after the centrifugation showing the separation of the particles through the density gradient, and the UV-VIS-NIR spectra and TEM images of the two indicated fractions.

Source: By the author.

Different strategies to improve the synthesis and overcome the polydispersity problem of the synthesis were tested and are summarized on **Figure 2.17**. The changing of Na_2S to $\text{Na}_2\text{S}_2\text{O}_3$ results in a broader peak in the NIR, and the TEM image revealed the presence of even bigger plates (**Figure 2.17A**). The use of an acid pH or N_2 atmosphere during the reaction improved the homogeneity of the sample; however the absorption at NIR decreased significantly, and, in the case of the acid pH, the particles diameter were bigger than 200 nm (**Figures 2.17B-C**). The addition of Na_2S in two steps was also performed and, although we observed a reduced number of triangular plates in the sample, the NIR band intensity was lower (**Figure 2.17D**).

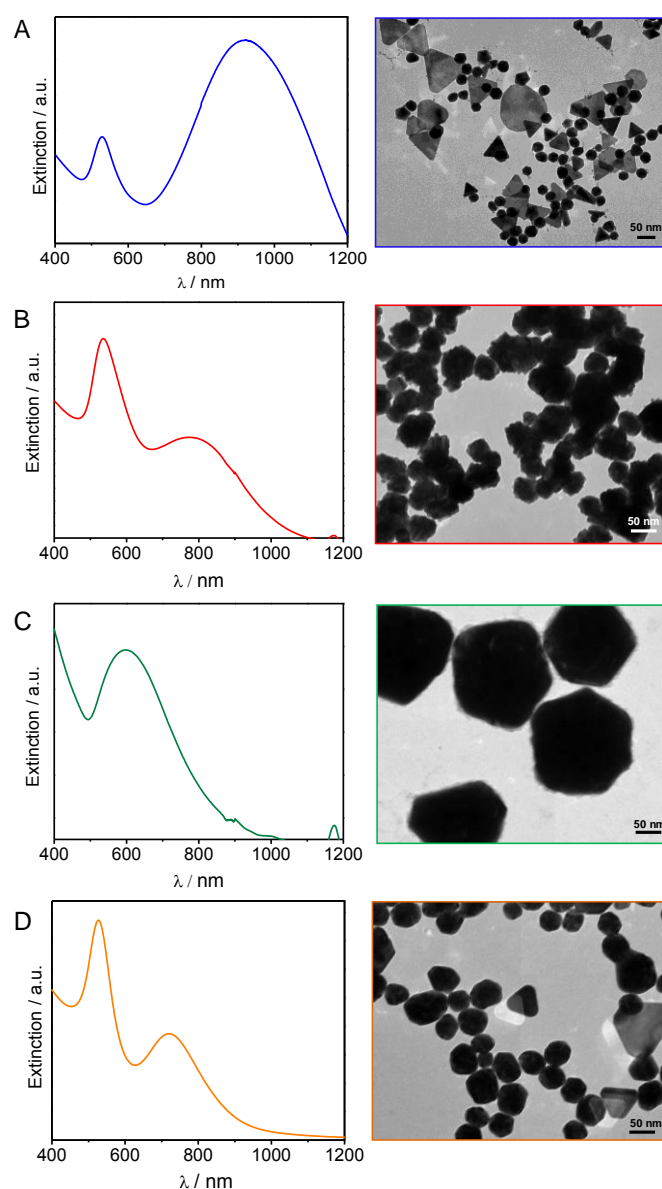


Figure 2.17 - UV-VIS-NIR spectra and their respective TEM images of different synthesis process to synthesized Au-coated Au₂S nanoshells. (A) Na₂S₂O₃:HAuCl₄ (18 mL:10 mL); (B) Na₂S : HAuCl₄ (18 mL : 10 mL) under N₂ atmosphere; (C) Na₂S : HAuCl₄ (18 mL : 10 mL) in pH = 1.6, and (D) Na₂S : HAuCl₄ (10 mL : 10 mL), and after 5 min, more 2 mL of Na₂S were added.

Source: By the author.

The synthesis in two steps seemed to be the best alternative for controlled fabrication of Au-coated Au₂S nanoparticles. In this way, a new strategy of was developed. Basically, the synthesis was performed in two steps: Au₂S nanoparticles were synthesized first, and then coated with a gold shell. The Au₂S NPs synthesis were performed by modification of a previous reported method by Morris et al.(76) They have performed the reaction by mixing 10 mL of 2 mmol L⁻¹ Na₃Au(SO₃)₂ and 12 mL of fresh 1 mmol L⁻¹ solution of Na₂S.9H₂O.(76) Both solutions were coreless before reaction, and after 24 h, the color of the solution had

changed to yellowish-brown. The authors proposed that Au_2S is formed by rapid nucleation to form very small Au_nS_m^- clusters, followed by a very slowly growth. In our experiments, instead of $\text{Na}_3\text{Au}(\text{SO}_3)_2$, we have used HAuCl_4 . The main difference between these two reagents is the oxidation state of the gold, while in $\text{Na}_3\text{Au}(\text{SO}_3)_2$ it is Au^+ , in HAuCl_4 is Au^{3+} . To evaluate the influence of the oxidation state of the gold in the synthesis reaction, the gold ions of the HAuCl_4 were reduced from Au^{3+} to Au^+ in presence of NaOH , the color of the solution changed from yellow to colorless, indication the reduction.(83) Then, Na_2S was added to the solution and, after 1h30min the color of the solution changed from colorless to yellowish-brown (inset of **Figure 2.18**). The Au_2S NPs spectrum is similar to the one obtained by Morries et al, as well as to other metal chalcogen nanoparticles such as Cu_2S and Ag_2S , and it is typical for semiconductor nanoparticles with an indirect optical band gap (**Figure 2.18A**). Therefore, it is clear that the product of the reaction between gold salt and Na_2S critically depends on the oxidation state of the gold salt. The TEM image revealed the production of very small nanoparticles with size around 5 nm.

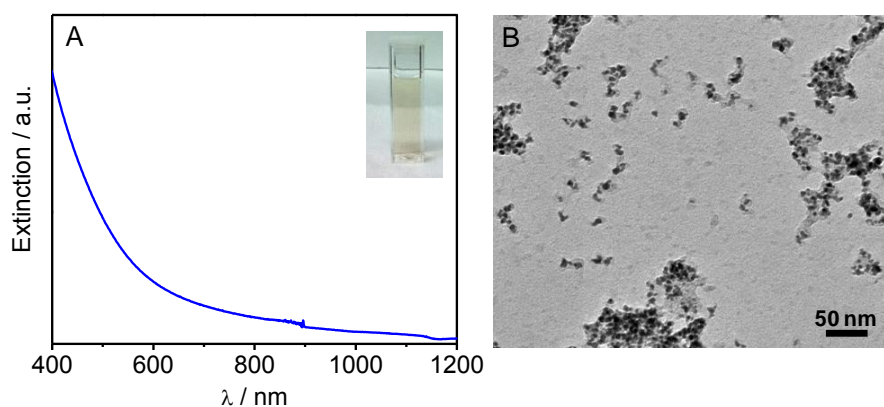


Figure 2.18 - UV-VIS-NIR spectrum and the respective TEM image taken 1h30 after mixing HAuCl_4 with NaOH and then with Na_2S .

Source: By the author.

The resulting Au_2S particles were then coated with a gold shell layer, according to what was described in the experimental section. The UV-VIS-NIR shown in **Figure 2.19** is very similar to the one obtained for Au-coated SiO_2 nanoshells (**Figure 2.2**), and the particles presented an average diameter around 70 nm. The TEM image also revealed that some particles present branches (inset of **Figure 2.19**). This is probably due to the use of NaOH in the reaction, which has been proved to induce the formation of branched gold nanoparticles.(83) Branched nanosystems have received considering attention in the last years due to the interesting and distinctive optical and electronic properties that they present, such

as gold nanostars.(84) By changing the reduction agent of the reaction, we might be able to produce non-branched systems.

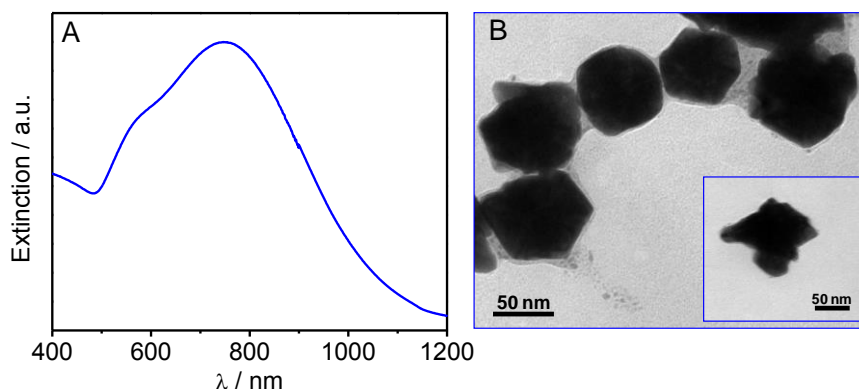


Figure 2.19 - UV-VIS-NIR spectrum and the respective TEM image of the Au-coated Au_2S nanoshells prepared by a new two-step method.

Source: By the author.

2.4 CONCLUSIONS

We have presented the synthesis and characterization of three types of gold based-plasmonic nanoparticles, and the dependence of the surface plasmon resonance with parameters such as shape, size and composition. Gold nanorods were synthesized using the seed-mediated method in presence of CTAB with high control over size and shape. The resulting particles were monodisperse and the longitudinal plasmon resonance wavelength was red-shifted by increasing the ratio length/width, called aspect ratio. Gold nanomatrashkas, consisting in a gold core, an interstitial nanoscale SiO_2 layer, and a thin gold shell layer ($\text{Au/SiO}_2/\text{Au}$) were synthesized with high control over the thickness of the interstitial silica layer and gold shell, and, consequently, their optical properties. The particles were also monodisperse with a final diameter around 100 nm and a strong NIR absorption.

A promising Au-coated Au_2S plasmonic material was also investigated. Our results have shown that the one step synthesis usually used to fabricate these particles do not enable a good control over size, distribution, and composition of the nanoshells. The resulting particles were composed not only of Au-coated Au_2S nanoshells but also of Au triangular plates according to energy dispersive spectroscopy analysis-coupled with transmission electron microscopy analysis. Density gradient was used to separate both systems, and although a good separation had been obtained, the difficult to remove the density gradient solution from the nanoparticles may limit their biomedical applications. Different methodologies were tested to

improve the yield of the synthesis, and the two step method, in which Au₂S small particles are first synthesized and then covered with a gold layer, has provide promising results.

All systems presented strong NIR absorption and maximum diameter around 100 nm, characteristics very relevant for medical applications. Moreover, their gold surface allows straightforward conjugation of polymers and biomolecules to the nanoparticle surface, which is important to maintain the particle stability and add new functionalities for applications in medicine.

3 PLASMONIC GOLD NANORODS COATED WITH CANCER CELL MEMBRANE AS A MULTIFUNCTIONAL SYSTEM FOR CANCER THERAPY

3.1 INTRODUCTION

3.1.1 Theranostic nanoparticles

Cancer has been one of leading causes of death in the world. According to the GLOBOCAN, project of the international agency for research on cancer, 14.1 million cases of cancer were estimated in 2012 and this number is expected to increase to about 19.3 million in ten years.(1) The current treatment for cancer include surgery, chemotherapy or radiation, which led to many side effects.(85) In this scenario, the search for new drugs and methods to enhance the early diagnosis and treatment of cancer is one of the major challenges in medicine today.

The combination between the medicine and nanotechnology has been offered exciting potential in the search for more efficient approaches against cancer. The golden standard in this area is the possibility to fabricate multicomponent nanomaterials with different properties that can be explored simultaneously in multiple applications.(86) In contrast to the traditional approach that uses separate materials and tools for diagnosis and therapy, nanomedicines have the potential to revolutionize the fight against cancer by integrating imaging agents and therapeutic drugs in one nanometer scale complex.(87) These so-called “theranostic”, enable detection and treatment in one single procedure and are emerging as an alternative to independently administered traditional strategies.(87)

The field of theranostics has been rapidly increasing due to the versatility of nanoparticles-based systems. Their unique optical, electronic and magnetic properties combined with the possibility to incorporate multiple types of molecules onto a single nanoparticle surface have enabled the design of many systems with different combined functionalities. The combination of functions can also provide important information about biodistribution and mechanisms, opening opportunities to create more efficient nanoplatforms.

3.1.2 Plasmonic Photothermal therapy (PPTT)

The use of laser light has offered exciting potential for applications in cancer therapy. However, to achieve therapeutic efficacy, high laser power densities are required, leading to the damage of both tumor and normal tissues.(34) To overcome this challenge, some agents are employed to improve the laser efficacy and selectivity, allowing the use of reduced irradiation energy. Transduction of light by specific agents into other types of energy such as chemical and thermal energy has provided the basis for the development of efficient treatment approaches such as photothermal therapy (PTT) and photodynamic therapy (PDT). In PTT, when the agent absorbs the light, electrons make transitions from the ground to the excited state. The relaxation through nonradiative process led to an increased kinetic energy and, consequently, an increase on temperature of the local medium around the absorbing species.(34,88)

Recently, plasmonic photothermal therapy (PPPT), which consists in the transduction of light into heat by plasmonic nanoparticles to generate rapid localized heating, has emerged as a potential, minimally invasive alternative for cancer treatment with reduced side effects.(34) As described in Chapter 2, electromagnetic waves incident on a plasmonic nanoparticle at the surface plasmon resonance (SPR) frequency induce a resonance oscillation on the particle surface.(34) These nanoparticle plasmons can decay by two mechanisms: radiative damping (scattering) and nonradiative dissipation.(55) The absorbed energy is converted into heat by a nonradiative mechanism through consecutive photophysical process that have been studied by ultrafast dynamics.(89) First, the generated surface plasmon resonances transfer their energy to the electrons through Landau damping. These energized electrons undergo rapid electron-electron scattering and within a few femtoseconds establish a nonequilibrium “hot” electron distribution, usually called hot electrons, characterized by an elevated temperature. These hot electrons then thermalize with the lattice via electron-phonon interactions on a picoseconds time scale. The heat is then dissipated to the surrounding medium via phonon-phonon coupling within hundreds of picoseconds, resulting in an increase in temperature of the surrounding medium by tens of degrees.(55,90)

The key factors that led to the PPTT efficacy include: (i) sufficient tissue penetration of the excitation light, (ii) large light-absorption cross section of the agents in the excitation wavelength,(iii) high photothermal conversion efficiency, and (iv) enough accumulation in the target tissue. The excitation light wavelength has to be in a region with maximal penetration through tissue. It is known that hemoglobin and water have their lowest

absorption coefficient in the near infrared region (NIR) region, more specifically from 650 to 900 nm (**Figure 3.1**).⁽⁸⁾ The other region of transparency has been described to be between 1000 and 1350 nm.⁽⁹¹⁾

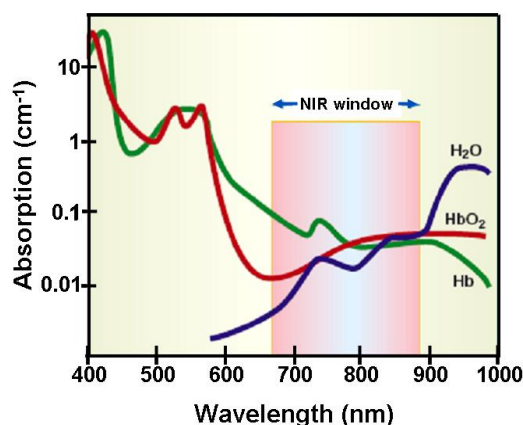


Figure 3.1 - The near infrared region (NIR) window for *in vivo* applications, showing the region of minimal light absorption by hemoglobin and water.

Source: WEISSLEDER et al.⁽⁸⁾

Second, the plasmonic nanoparticles must have large light-absorption cross section in the excitation wavelength. As discussed in Chapter 2, gold-based nanoparticles present interesting optical absorptions, which can be easily tuned to NIR by modifying their structural characteristic such as geometry, size, and shape.⁽⁹²⁾ Therefore, the absorption in the NIR region makes gold nanorods, nanoshells, and nanomatryoshkas suitable for *in vivo* applications and efficient light-to-heat converters due to their large absorption cross-section.^(10, 65) Further, gold nanorods, nanoshells, and nanomatryoshkas present high photothermal transduction efficiency, which represents the ability of a nanoparticle in converting absorbed light into a temperature increase of its surrounding medium, and these systems have proved to have high potential for photothermal therapy.^(10, 55)

Nanostructures NIR transducers agents present several advantages over conventional photothermal agents. Besides the fact that their properties can be adjusted in the synthesis process by controlling their geometry and composition,⁽⁵⁴⁾ gold nanomaterials have shown good chemical/thermal/photo stability and low cytotoxicity.⁽⁵⁸⁾ Their strong absorption cross-section also allows effective laser therapy using lower energies.⁽³⁴⁾ Moreover, the facility to modify the gold surface allows the incorporation of drugs and biologic molecules for applications in drug-delivery and therapy.⁽⁹³⁻⁹⁴⁾ Additionally, they can provide high-contrast images of cancer cells using a variety of optical techniques, including dark-field

microscopy,(44) reflectance confocal microscopy,(45) one- or two-photon fluorescence imaging,(46) surface enhanced Raman scattering (SERS),(47-48) and photoacoustic imaging,(49) which open opportunities for fabrication of theranostic platforms. Furthermore, nanomaterials have demonstrated extension of circulating half-life and higher passive accumulation in tumor sites (EPR effect) when compared to small molecules based systems.(57,95)

Gold nanoshells were the first nanoparticle used to demonstrated PPTT by Halas and co-workers in 2004.(96) Complete regression of the tumor after 10 days of gold nanoshell photothermal treatment has reported, and after 90 days post-treatment, all mice remained healthy and free of tumors, while tumors in control groups continued to grow rapidly.(7) The potential of gold nanoshells for photothermal therapy in tumor together with their low cytotoxicity have led to their current use in clinical trials for head and neck cancer treatment.(97-98) Recently, Ayala-Orozco et al. demonstrated that the tumor uptake of gold nanomaterials was higher than gold nanoshells, and, consequently nanomaterials presented an improved photothermal therapy efficacy. They attributed this enhancement to the more appropriate diameter of nanomaterials (~100 nm) when compared to nanoshells (~150 nm).(53)

The use of gold nanorods for PPTT applications has also been widely explored in the last years.(92) Dickerson et al. demonstrate that PEGylated-AuNRs can be efficiently used for *in vivo* PPTT treatment of deep-tissue malignancies.(9) AuNRs have also been proved to be a non-invasive and efficient procedure for the treatment of lymph node metastasis.(99) Silica-coated AuNRs has also been demonstrated to be a great platform to be used as a dual probe for imaging and cancer therapy.(100)

The mechanism of cell death due to PPTT using gold nanoparticles has been investigated. According to recent studies, it is clear that one single mechanism may not be sufficient to describe the effects of PPTT.(90) Apoptosis and/or necrosis and sometimes also oncosis have been reported. The observation of different cellular responses to the PPTT results from variation in methods of nanoparticle delivery, dosing, and irradiation conditions.(90) Nanoparticle location also influences the toxicity of photothermal heating. For example, Tong et al observed that the cells with internalized AuNRs required 60 mW laser intensity to cause cell damage, while for surface-bound nanorods only 6 mW was necessary.(101) In this case, cell death was attributed to the disruption of the cell membrane. The laser intensity during PPTT also plays a significant role in the cell death mechanism. According to Li et al, for cells irradiated with a femtosecond pulsed scanning laser of 13.9

and 9.5 W/cm^2 the death was caused only by apoptosis. Increasing the laser power to 27.8 W/cm^2 (10 scans) also induced apoptosis, while 30 scans induced necrosis, and 55.6 W/cm^2 resulted in necrosis after only 1 scan.(102) To better understand the mechanism of cell death, Chen et al monitored the EMT-6 breast cancer cells treated overnight with gold nanorods during PPTT in real-time. The nanorods were located in the lysosomes, and irradiation with a femtosecond pulsed laser exploded them; however, cell death was not immediate. According to the authors, photothermal treatment caused the formation of $10 \text{ }\mu\text{M}$ cavities, leading to rupture of the plasma membrane.(103)

3.1.3 Combined therapies

The heating caused by phototherapy may also increase susceptibility of cancer cells to other treatments. Several studies have reported that a synergic toxicity effect resulted from the combination of gold nanomaterials and chemotherapeutic drugs in PPTT.(90) For example, Chen et al developed doxorubicin-conjugated gold nanorods for combined thermal therapy and chemotherapy *in vivo*.(104) The therapeutic effect and tumor inhibition of the multifunctional platform with NIR irradiation was more pronounced than free doxorubicin or only gold nanorods + laser. In another study, gold nanorods and doxorubicin co-loaded polymersomes were developed.(105) It was also found that co-therapy significantly improved therapeutic efficacy compared with chemo or photothermal therapy alone.

Many studies have reported the use of gold nanorods and photosensitizers for a combined effect of PPTT and PDT.(92) When chlorin-p6, a widely used photosensitizer, is conjugated with gold nanorods, the production of singlet oxygen increases significantly.(106) This effect has been attributed to the coupling with the plasmons of the AuNRs. Moreover, the uptake of chlorin-p6 was more efficient in the conjugate compared to free chlorin-p6.(106) In a similar platform, Wang et al. developed a multimodal therapy using gold nanorods conjugated with an aptamer, and the photosensitizer chlorin-e6.(107) They showed that the aptamer changes its structure upon irradiation and release the photosensitizer for production of singlet oxygen, resulting in an enhanced therapeutic effect.(107) Kuo et al proposed the conjugation of gold-based materials with the hydrophilic photosensitizer, indocyanine green.(108) They showed that the combination of PPTT and PDT proved to be more efficient in killing cancer cells compared to both treatments alone. They also described an enhanced photostability of the indocyanine green after conjugation.

3.1.4 Cell membrane coated nanomaterials

Although much progress has been made in applications of nanomaterials for diagnostic and therapy, significant clinical advances have not been observed. One of the main reasons for this failure is the low accumulation rate of the nanoparticles in the target tissue, which depends on their ability to escape the immune system, cross the biological barriers and accumulate at target tissues.(12)

It is known that nanomaterials can accumulate in the tumor by a passive or active mechanism. The passive accumulation is attributed to the enhanced permeability and retention effect (EPR).(57) However, the variety of vascularization degree and permeability of the tumors together with the relative short blood circulation time of nanomaterials have limited this strategy.(20) In the active accumulation, the nanomaterials are functionalized with specific biomolecules, such as antibodies,(109) peptides,(110) aptamers,(111) which specifically recognize the receptors overexpressed on cancer cells membranes.

Recently, it has been shown that the ability of the biomolecules-functionalized nanomaterials to target the cancer cell can be damaged when they are in a biological environmental. Salvati et al. demonstrated that Transferrin-functionalized nanoparticles, a protein that recognizes receptors of transferrin overexpressed in cancer cells, lost their specificity in the biological media.(112) This effect has been attributed to the interaction of the nanocomposite with proteins of the media, called opsonization, which can form a layer of unspecific proteins around the nanomaterial, known as corona.(113) Similarly, Xiao et al demonstrated that the functionalization of gold nanorods with cRGD peptides, which recognized specifically $\alpha_v\beta_3$ integrin, an important biomarker for cancer cells, did not provide a significant advantage in the *in vivo* tumor accumulation.(114)

The functionalization of nanoparticles with polyethylene glycol (PEG) has been widely explored to extend the *in vivo* blood circulation time of the particles and improve their passive and active accumulation. The addition of PEG to the nanoparticle surface can avoid the adhesion of opsonins proteins present in the blood serum, increasing their blood circulation time and consequent tumor accumulation.(14) PEGylation also increases the nanoparticle stability in buffer and serum due to the hydrophilic ethylene glycol repeating units.(14) Although much progress has been made, the accumulation in the target region is still low, reducing the therapeutic effects of nanoparticles and increasing the risk of side effects. Also, some evidences of the immunological response anti-PEG have been reported.(15)

Overcoming the immune system barriers and enhancing the accumulation of the nanoparticles in the tumor are the major challenges in nanomedicine today.(115) These problems have inspired the development of new functionalization strategies. Among them, the coating with natural cell membranes has been shown to be an interesting alternative to camouflage the particles and extend their blood circulation time. Hu et al showed that red blood cell membrane (RBC)-coated polymeric nanoparticles present longer blood circulation time than the PEG-coated ones (**Figure 3.2**).(16) More recently, the authors showed evidences that the CD47 proteins, a biomolecule capable to inhibit the phagocytosis and modulate the immunological response, are transferred to the nanoparticle's surface and get exposed, allowing them to perform molecular interactions and reducing their susceptibility for being captured by macrophages.(17) The ability to transfer to nanomaterials immunomodulatory proteins including CD47 at an equivalent density to that of natural cells has been described as one of the most important characteristic of the cell membrane approach.

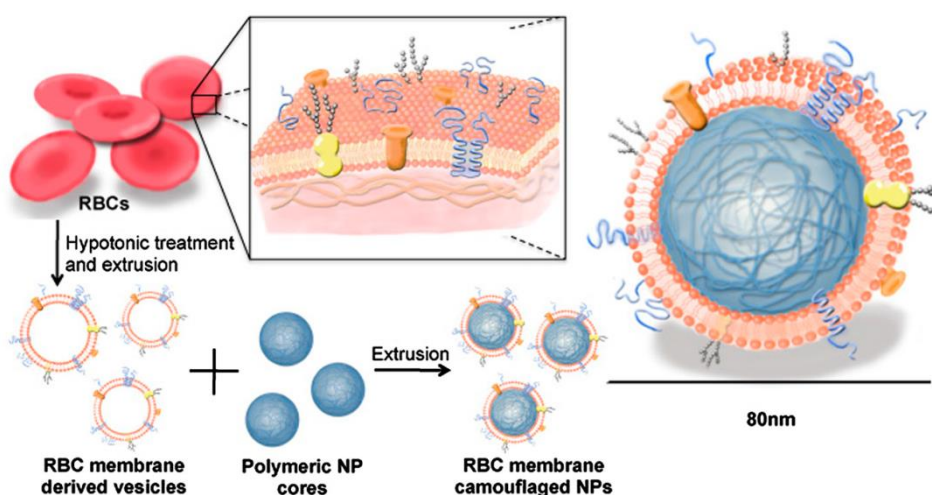


Figure 3.2 - Schematics of the synthesis of the Red blood cell (RBC) membrane-coated polymeric PLGA nanoparticles.

Source: HU et al.(16)

RBC membrane coating has also been used to reduce the phagocytic uptake and extend the blood circulation time of gold nanoparticles,(116) gold nanocages,(117) iron oxide,(118) and upconversion nanoparticles.(119) Similarly, leukocytes cell membrane-coated porous silica nanoparticles have shown lower tendency to be eliminated by immunological system.(12) Ding et al developed erythrocyte membrane-coated upconversion nanoparticles and photosensitizer for NIR-triggered photodynamic therapy applications.(119) Erythrocyte ghosts have been used to encapsulate iron oxide for magnetic resonance imaging

applications.(118) Piao et al also showed that RBC membranes-coated gold nanocages exhibit significantly *in vivo* blood retention and circulation lifetime compared to poly(vinylpyrrolidone) coated ones.(117) As a result, this system demonstrate enhanced tumor uptake when administered systematically, allowing a much more effective photothermal therapy treatment *in vivo*. These new biomimetic systems have demonstrated enhanced tumor uptake with potential for more effective applications in medicine.

The cell membrane coating strategy has been extended to cancer cells. Fang et al showed that the coating of PLGA nanoparticles with cells membranes derived from MDA-MB-435 cancer cells allows particle functionalization with multiple membrane-bound tumor-associated antigens.(18) These systems possess the same adhesion domains of its source cancer cells, responsible for multicellular aggregate formation in tumors, and have demonstrated increasing specificity for cancer cell targeting.(18) This strategy allows mimicking the complex functions of the cells without using engineered antibodies or aptamers, which could have high cost and, as discussed early, may not be effective to target cancer cells. Also, the cancer cell membrane coating strategy may also be explored for cancer immunotherapy.(19) Therefore, this emerging top down approach of functionalization cannot only increase the *in vivo* circulating time of the nanoparticles and, consequently, their accumulation in the tumor, but also can add new functionalizations and properties to nanosystems.

3.1.5 Cell membrane vesicles as carriers

Natural cell membrane vesicles have also shown great potential as drug delivery systems. The use of reconstructed membranes from stem cell as platform for drug-delivery (20) has been reported as well as the loading of indocyanine green into nano-sized vesicles derived from erythrocyte cells for combined optical imaging and phototherapy of tumors.(120) Capsules derived from erythrocytes have exhibited many favorable properties such as efficient drug loading, biocompatibility, and prolonged blood circulation time.(121-122)

Similarly, cancer cells-derived vesicles have emerged as new drug delivery system with increasing specificity. Methotrexate-loaded tumor cells microparticles have proved to effectively deliver therapeutic agents to tumor cells in murine tumor models, killing them without typical side effects associates with the drug.(123) A recent study also have reported

the fabrication of a multifunctional chemo- and photo-thermal agent composed of folic acid (FA)-modified, multi-layered, hollow microcapsules loaded with gold nanorods and the anti-cancer drug doxorubicin.(104)

3.1.6 β -Lapachone

β -Lapachone (β -Lap) is an ortho-naphthoquinone with molecular weight of 242.27 Da (**Figure 3.3**) that has attracted significant interest in the last years. It is a plant-derived anticancer agent, first isolated from the bark of Lapacho tree (genus *Tabebuia*) in South America rainforests.(124) Currently, β -Lap is produced through cyclization of lapachol in sulphuric acid.(125) One of the most advantages of β -lap is the fact that its cytotoxicity is activated by NADP(H):quinine oxidoreductase (NQO1), an enzyme highly expressed (up to 20x) in many human cancers, such as lung, prostate, breast, and pancreas.(126) NQO1 detoxifies harmful quinines by catalyzing two-electron reduction of the quinines to hydroquinones using NADH or NAD(P)H as the electron source. It has been suggested that NQO1 causes a futile redox cycle between β -Lap and its two electron reduced hydroquinone form, leading to a generation of reactive oxygen species, Ca^{2+} -dependent DNA damage, hyperactivation of poly ADP polymerase-1, and decrease in the NAD^+ and ATP, which results in cell death.(127-128) Its anti-cancer effect has been described to be independent of p53, caspase, and cell cycle status, which can minimize drug resistance.(124) Therefore, β -Lap presents very low toxicity to normal cells and can be used as an effective and selective antitumor agent.

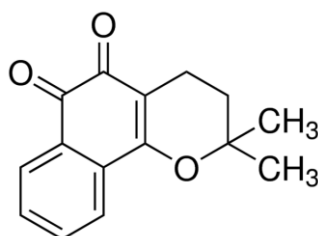


Figure 3.3 - Chemical structure of β -Lapachone.
Source: SIGMA...(129)

The lethal concentration of β -lap has been shown to be around 1 and 30 μM , and for most of cancer cells lines, this value is around 1 to 5 μM .(130) However, its poor solubility, low stability in circulation, short blood circulation time, and poor specificity led to low tumor

accumulation and have limited its therapeutic applications.(124) To overcome these problems, initial studies have focused on increasing the aqueous solubility of β -Lap through complexation with hydroxypropyl- β -cyclodextrin.(131) However, the fast dissociation of this complex, low tumor accumulation and recent observations about cyclodextrin side effects (128) have motivated the search for new alternatives.

Recently, substantial efforts have focused on nanostructured systems. The encapsulation of β -Lap inside polymeric nanostructures has increased its stability while maintaining its NQO1-dependent cytotoxicity.(128, 132) Also, new properties such as optimal size, longer blood circulation time, diffusion-based release kinetics, and multifunctionality can be achieved using a nanostructure platform. Zhang et al coencapsulated paclitaxel, one of the most effective broad-spectrum chemotherapeutic agent, together with β -Lap into PEG-PLA micelles.(124) They demonstrated a strong synergistic cytotoxicity effect against cancer cells, including pancreatic cancer cells. Conjugation of β -Lap with graphene oxide (133) and gold nanoparticles (134) have also been demonstrated. These β -lap nanoconjugates have demonstrated selective cytotoxicity, and represent a potential treatment for a multifunctional strategy against cancer.

3.1.7 Toxicity of nanomaterials

The potential applications of nanoparticles in medicine are highly dependent on toxicology studies to determine their stability and effects in a biological medium.(135) The toxicity of gold-based nanomaterials has been described to be dependent on several parameters such as size, shape, and surface functionalization.(92) For gold nanorods, the high concentrations of cytotoxic cetyltrimethyl ammonium bromide (CTAB) used in the synthesis and the difficulty to displace it efficiently without compromising the properties of particles is a key barrier to guarantee their efficiency and safety.(136) The surfactant may internalize into the cells with and without the AuNRs, damaging the mitochondria, and inducing apoptosis.(137) Many strategies have been developed to overcome this problem. For example, due to the high binding affinity of sulfur-metal bond, thiol-containing molecules have been extensively used to replace CTAB molecules. One of the most used methods consists of replacing CTAB with thiolated polyethylene glycol (PEG),(138-140) because PEG provides high stability in biological media and may extend the blood circulation time of nanomaterials.(141)

The influences of the aspect ratio and the surface functionalization in the toxicity and uptake of gold nanorods have also been investigated.(137) Qiu et al showed that although the cellular internalization is highly dependent of the aspect ratio and surface modification, only the functionalization contributed significantly to the toxicity. Moreover, the formation of a protein around the nanorods have significantly reduced their toxicity.(142) Adura et al. showed that a conjugate containing AuNRs and CLPFFD peptide, that recognizes toxic β -amyloid aggregates present in Alzheimer's disease, has less influence on the cell viability compared to the regular AuNRs coated with CTAB.(143) The protein corona approach has been demonstrated to reduce the toxicity of AuNRs.(142) A comparative analysis of the impact of fetal bovine serum (FBS)-AuNRs and CTAB-AuNRs on the cytoplasmic membrane structure revealed that CTAB-AuNRs aggregates on the membrane of A549 cells (human lung adenocarcinoma epithelial cell line), destroying it. For FBS-AuNRs, the presence of the protein corona facilitated the protein receptor-mediated internalization and translocation of AuNR to endo-/lysosomes, without causing dramatic effects on the membrane structure.(142)

Although much progress has been made regarding nanotoxicology, the variety of nanomaterials, functionalizations, size and shape, combined with the lack of standardization in the assays, have led to some inconclusive results. Lison, D. et al have systematically revised studies related to cytotoxicity of silica nanomaterials to show the gaps and the need for standardization studies in that area.(135)

3.2 EXPERIMENTAL SECTION

3.2.1 Materials

All reagents were used without any further purification and the solutions were prepared using ultrapure water (18.2 M Ω cm). All glassware were cleaned with aqua regia and thoroughly washed with distilled and Milli-Q water. Cetyltrimethylammonium bromide (CTAB), silver nitrate (AgNO₃), tetrachloroauric acid (HAuCl₄), sodium borohydrate (NaBH₄) e ascorbic acid were purchased from Sigma-Aldrich. β -Lapachone (β -lap) and poly(ethylene glycol) methyl ether thiol (mPEG-SH) average M_n 5,000 were also obtained from Sigma-Aldrich.

3.2.2 Gold nanorods (AuNRs) synthesis

Gold nanorods (AuNRs) were synthesized by the seed-mediated method in presence of the surfactant CTAB.⁽⁷²⁾ Briefly, the seeds were prepared by adding 250 μL of $\text{HAuCl}_4 \cdot 3\text{H}_2\text{O}$ 0.01 mol L^{-1} in 7.5 mL of CTAB aqueous solution 0.1 mol L^{-1} under gentle stirring. Next, 600 μL of iced cold NaBH_4 0.1 mol L^{-1} was added and the system was kept under vigorous stirring for 10 min. The color of the solution changed from yellow to pale brown. The solution was kept at 25°C for about 2 hours before using. The growth was performed by adding 4 mL of 0.01 mol L^{-1} $\text{HAuCl}_4 \cdot 3\text{H}_2\text{O}$ in 47.5 mL of 0.1 mol L^{-1} CTAB aqueous solution, followed by 600 μL of 0.01 mol L^{-1} AgNO_3 and 480 μL of 0.01 mol L^{-1} ascorbic acid solutions. The color of the system changed from dark yellow to transparent, indicating the reduction of the Au^{3+} to Au^+ . Finally, 70 μL of the seed solution previously prepared were added and the system was kept under very gentle stirring for 20 min. The system was left at room temperature and protected from light for 4 h, and the supernatant was washed by centrifugation at 10000 g for 5 min. The suspension was cooled at 4°C to crystallize the excess of CTAB and centrifuged at 2000 g for 2 min to remove the crystals.

The resulting nanorods were subsequently functionalized with poly(ethylene glycol) methyl ether thiol (mPEG-SH). For this, mPEG-SH was mixture with the AuNRs in a final concentration of $200 \mu\text{mol L}^{-1}$ and the system was sonicated for 30 minutes. The particles were shaken for more 12 hours at room temperature and then centrifuged (10000 g, 5 min) to remove the excess of mPEG-SH and CTAB. The concentration of the resulting PEG-AuNRs for the experiments was standardized by their optical density at 750 nm.

3.2.3 Cell culture

Human lung adenocarcinoma epithelial (A549) and rat hepatocarcinoma (HTC) cells were acquired from Rio de Janeiro Cell Bank (BCRJ). Human hepatoma (HepaRG) cells were kindly supplied by Dra. Natalia Inada from the Optics Group, Physics Institute of Sao Carlos, University of Sao Paulo, Brazil. All the cell culture reagents were previously autoclaved and the procedures were performed in a laminar flow hood using sterile materials. All the cells lines were cultured in *Dulbecco's modified Eagle's medium* (DMEM) (Vitrocell, Campinas, Brazil) supplemented with 10% of Fetal Bovine Serum (Vitrocell, Campinas, Brazil) and maintained at 37°C and in 5% CO_2 in a humidified incubator. Cells viability was investigated

always before the assays (data not shown) according to the trypan blue (Sigma-Aldrich, USA) exclusion assay, showing viability higher than 95%.

3.2.4 Extraction of A549 cancer cell membrane (CM)

The cancer cell membranes were isolated and purified by ultracentrifugation based on a previous method proposed by Lung et al (144) and reconstructed as vesicles by extrusion. Briefly, three cell culture flasks of 160 cm² containing about 2x10⁷ A549 cells/each were rinsed in PBS and removed from flasks using trypsin solution 2.5 g/L with EDTA (Vitrocell, Campinas, Brazil). The cells were washed three times by centrifugation (1000 g, 5 min) in PBS, and lysed by incubation in a hypotonic buffer (10 mM Trisbase, 1.5 mM MgCl₂, 10 mM NaCl, pH 6.8) for 5 min at 4°C. The lysed cells were centrifuged (300 g, 5 min), resuspended in the gradient buffer (0.25 M Sucrose, 10 mM HEPES, 100 mM Succinic acid, 1 mM EDTA, 2 mM CaCl₂, 2 mM MgCl₂, pH 7.4), and homogenized by 70 strokes (1900 rev/min) using a homogenizer (Glass homogenizer VIRTUS PII), followed by centrifugation at 10000 g for 10 min at 4°C to remove cell debris. The supernatant was collected and centrifuged at 150000 g for 1h20 using an ultracentrifuge Optima MAX-XP (Beckman Coulter, USA) at 4°C. The pellet, containing the membranes, was dispersed in 1 mL of PBS containing Complete Protease Inhibitor (Roche Diagnostics, Mannheim, Germany) and stored at -80°C.

3.2.5 A549 cancer cell membrane (CM) characterization

The membrane was characterized by sodium dodecyl sulfate polyacrylamide 10% gel electrophoresis (SDS-PAGE). The standard BenchMark Protein Ladder (Invitrogen) was used as reference for mass determination and the gel was fixed and stained with silver nitrate (ProteoSilver kit, Sigma-Aldrich). The quantitative determination of protein in the cell membrane was performed by the QuantiPro BCA Assay Kit (Sigma-Aldrich), a colorimetric method for the determination and quantification of total proteins based on the capacity of the proteins to reduce Cu²⁺ to Cu⁺ in an alkaline medium. The purple color results from the interaction of the bicinchoninic acid (BCA) with the ion Cu⁺ and the absorption at 562 nm exhibited by the complex is approximately linear with the increasing of the protein concentration in a wide range (20-2000 µg/mL). The procedure was performed according to the described at the assay's protocol. First, a calibration curve was obtained using known

concentrations of bovine serum albumin (BSA) (**Figure 3.6**) and then different concentrations of the cell membrane were measured and the concentration determined from the calibration curve. All the absorbance measurements were performed in a 96-well plate using a SpectraMax M3 microplate reader (Molecular Devices).

The lipid composition of the cell membrane was analyzed by Iatroscan TLC/FID (Iatroscan MK-VI, Iatron, Japan), which combines thin-layer chromatography (TLC) and flame ionization detection (FID) using hydrogen flow of 174 mL/min and air flow 2000 mL/min. It has been shown to be an important technique in lipid determination.⁽¹⁴⁵⁾ The lipids standards HC (aliphatic hydrocarbons), WE/SE (ester), TAG (triglycerides), FFA (free fatty acids), ALC (aliphatic alcohol free), ST (sterol), AMPL (mobile polar lipids in ketone) and PL (phospholipids) were obtained from Sigma-Aldrich and all other chemicals and solvents were of analytical grade. For this analysis, the A549 cell membranes were resuspended in chloroform after ultracentrifugation using the concentration as previously described. Before the Iatroscan analysis, the samples were homogenized in an ultrasound bath at 4°C for 15 min. The lipids samples were resolved in three steps, which involve subsequent elution stages with increase solvents polarity. These are: solution 1 (98.95% hexane, 1% diethyl ether and 0.05% formic acid), solution 2 (79% hexane, 20% diethyl ether and 1% formic acid), solution 3 (100% acetone) and solution 4 (50% of chloroform, 40% methanol and 10% water).

3.2.6 A549 cell membrane-loaded β -lapachone (CM- β -Lap)

The cell membrane with a protein concentration of 774.9 $\mu\text{g/mL}$ was sonicated in an ice bath sonicator at 4°C for 15 min. Then, β -Lap (0.07 mg, $\sim 0.3 \text{ mmol L}^{-1}$) was added to the system and sonicated in an ice bath sonicator at 4°C for 15 min, followed by gentle shaken for 2 h at 4°C and protected from light. The system was extruded through 200 nm polycarbonate membrane using a miniextruder (Avanti Polar Lipids), and dialyzed against 0.2x PBS buffer at 4°C and protected from light for 3 hours to remove the remnants from cell-membrane extraction and the excess of β -Lap. The result suspension was collected and kept at 4°C.

3.2.7 A549 cell membrane-loaded β -lapachone-coated PEG functionalized gold nanorods (CM- β -Lap-PEG-AuNRs)

The CM/AuNRs ratio was tested and optimized in order to have uniformity, surface stability and reproducibility. After dialysis, CM- β -Lap suspension was extruded 11 times through 200 nm polycarbonate membrane using a miniextruder (Avanti Polar Lipids), followed by more 7 times in 100 nm. The size and distribution of the extruded membrane were evaluated by Dynamic Light Scattering (DLS) (Zetasizer Nano ZS, Marvern). 500 μ L of this suspension was added to 2000 μ L of PEG-AuNRs (optical density at 770 nm = 0.5) and extruded 7 times through polycarbonate membrane of 100 nm. The system was centrifuged (5000 g, 10 min) to remove the excess of membrane or β -Lap and the particles were resuspended in 1x PBS.

β -lap loading concentration in the final system was determined by destabilization of the cell membrane to release the anticancer agent. To this, CM- β -lap-PEG-AuNRs were diluted in ethanol and sonicated for 30 min. The particles were then centrifuged at 10000g for 15 min and the supernatant spectrum was measured using an UV–VIS spectrophotometer (Hitachi U-2900), and the appropriate baseline. The concentration was calculated using the extinction coefficient calculated from the calibration curve (**Figure 3.5**).

For comparison in the cytotoxicity and phototherapy assays, we also synthesized A549 cell membrane-coated PEG-functionalized gold nanorods (CM-PEG-AuNRs), i.e., without β -lap, using the same procedure as described for CM- β -Lap-PEG-AuNRs. The concentration of free PEG-AuNRs, CM-PEG-AuNRs and CM- β -Lap-PEG-AuNRs was set using the same optical density (OD) of the longitudinal plasmon peak.

3.2.8 Photothermal therapy

The optical properties of the CM- β -Lap-PEG-AuNRs were analyzed and compared with the PEG-AuNRs. 700 μ L of each system ($OD_{750\text{ nm}} = 0.59$) in a 3 mL polystyrene cuvette were irradiated using a cw 808 nm diode laser with elliptical beam of diameter $\sim 1.5\text{ mm} \times 3.0\text{ mm}$ (iZi, LASERline). The power at the distance of irradiation was measured and adjusted to have a power density of approximately 1.5 W/cm^2 . The temperature was monitored using an optical thermometer (FOT Lab Kit Fluoroptic Thermometer, LUXTRON). The initial temperature was the room temperature in the laboratory ($\sim 23^\circ\text{C}$).

The release of β -Lap was determined based on previous methods.(128) Briefly, the final CM- β -Lap-PEG-AuNRs sample was divided in four aliquots (400 μ L each), irradiated with the laser with a power density of approximately 1.5 W/cm² at different times (5, 10, 15, 20 min), and centrifuged immediately to separate the released β -Lap from the particles at (5000 g, 10 min at 4°C) using a Microcon centrifugal filters (MW cutoff = 3 kDa). Typical absorbance of the β -Lap at 257 nm was measured in the resulting filtrate and used to calculate the release concentration based on the calibration curve (**Figure 3.5**).

For the *in vitro* photothermal analysis, 5×10^4 A549 cells were seed in a 96-well plate. After 24 h, the media was removed and 140 μ L of media containing of PBS (control), CM- β -Lap-PEG-AuNRs or CM-PEG-AuNRs were added to each well in triplicate. We use the absorbance at the maximum longitudinal peak to standardize the concentrations of both systems. The final OD at 750 nm in cell culture media in both systems was 0.3. The cells were incubated for 4 hours 37 °C and 5% CO₂ and washed twice with PBS. Finally, 100 μ L of media were added to each well and the cells were irradiated using the same cw 808 nm diode laser with elliptical beam of diameter ~ 1.5 mm x 3.0 mm (iZi, LASERline) and power density was also adjusted to have approximately 1.5 W/cm². After exposure to the laser light for 10 min, the cells were incubated for additional 2 h at 37 °C and 5% CO₂, followed by staining with 0.4% trypan blue (Sigma-Aldrich) to evaluate the viability. The images were taken using an inverted light Zeiss microscope.

3.2.9 Characterization

The optical properties of the PEG-AuNRs before and after conjugation with CM- β -Lap were characterized by Ultraviolet-Visible-Near Infrared (UV-VIS-NIR) spectroscopy (Hitachi U-2900). Their size, distribution and morphology before and after laser irradiation were analyzed by Field-emission Scanning Electron Microscopy (FEG-SEM). For this, silicon substrates (P-type/boron-doped silicon, Sigma Aldrich) were cleaned with isopropanol, ethanol and water in an ultrasound bath (2 min each) and dried in a stream of nitrogen gas. The samples were diluted in water, drop-cast onto the substrate and allowed to dry in ambient conditions for 12 h. Field-emission SEM imaging was obtained with a Zeiss Sigma VP FEG-SEM at 3 kV in high vacuum mode.

Dynamic Light Scattering (DLS) was used for characterizing the size and aggregation state of nanomaterials *in situ*, i.e., in suspension. DLS measures the light scattered from a

laser that pass through the colloidal suspension and by analyzing the modulation of the scattered light intensity as function of time, the hydrodynamic size and agglomerates can be determined. Simply, the technique is based on the Brownian motion of the particles in suspension. Therefore, larger particles will diffuse slower than the smaller ones and the time dependence of the scattered light to produce a correlation function can be mathematically linked to the particle size. The analyses were performed in triplicate at 25°C using a Malvern Nano-ZS spectrometer (Malvern Instruments, UK).

Zeta Potential was used to determine the surface charge of nanoparticles in suspension. Nanoparticles have a surface charge that attracts a thin layer of ions of opposite charge to the particle surface, forming the double layer, which diffuses throughout the suspension with the particle. The electric potential at the boundary of the double layer is known as the zeta potential of the particles, whose values typically range from -100 to +100 mV. The magnitude of the zeta potential is an indicative of the electrostatic colloidal stability. The analyses were performed in triplicate at 25°C using a Malvern Nano-ZS spectrometer (Malvern Instruments, UK) and the results are presented as mean \pm standard derivation resulting from three different measurements.

3.2.10 Isothermal Titration Calorimetry (ITC)

ITC has emerged as an useful technique to investigate the thermodynamic interaction between nanoparticles and molecules.(146, 147) Previous studies have shown the use of ITC to evaluate the capacity of nanoparticles to avoid protein adsorption, which is a relevant property to decrease the opsonization and extend the blood circulation time of the nanomaterials.(148) In this study, interactions between BSA, a major representative globular protein present in the serum, and PEG-AuNRs and CM- β -Lap-PEG-AuNRs were evaluated. ITC experiments were performed in a MicroCal ITC200 (Malvern Instruments) at 25 °C with a continuously stirred at 250 rpm by titrating BSA protein solutions (10 $\mu\text{mol L}^{-1}$) into the sample cell containing the nanoparticles. 2 μL of BSA were titrated 18 times with 180 seconds between injections. As a comparison, we also performed the titration of BSA solution into CTAB-coated AuNRs. However, since CTAB-AuNRs presented low stability in buffer solution, CTAB/PEG-AuNRs, which consisted in the PEGylation of the CTAB-AuNRs using a lower concentration of mPEG-SH, just enough to keep the particles stable in 0.1xPBS were used. The zeta potential of CTAB/PEG-AuNRs was around +18 mV. The concentration of the

three nanoparticle systems was kept about the same (OD at 750 nm = 0.6) and all samples were in 0.1xPBS buffer. The heat of dilution of the protein was performed by titrating BSA into buffer at the same concentrations. No quantitative analysis was performed due the difficult to determine exactly the molar concentrations of the particles.

3.2.11 Cellular Uptake

The cell uptake was evaluated using different strategies. First, the CM-PEG-AuNRs were labeled with fluorescent dye molecules for optical tracking. The CMs were stained with CellMask Deep Red plasma membrane stain (Life Technologies) with excitation/emission wavelengths of 649/667 nm. The system was incubated for 30 min at 4°C and protected from light. The next steps of dialysis and conjugation with PEG-AuNRs were performed as described previously. It is important to note that at the end of the conjugation, the CM-PEG-AuNR system is centrifuged, which also allows to remove the excess of the dye molecules. Next, A549 cells were seeded in a μ -Dish 35 mm (Ibidi) and cultured for 24 h at 37°C and 5 % CO₂, following by changing the media by fresh media containing CellMask-labeled CM-PEG-AuNRs and incubated for 4 h. As a control and since no information about CellMask stain is available, we observed the effect of free CellMask stain incubated with A549 cells in the same conditions. The cells were rinsed twice with PBS and fixed with 4% formaldehyde in PBS for 10 min, followed by rinsing with PBS. The cell nuclei were stained by incubating the cells with 5 mg/mL Hoechst 33342 dye solution (Sigma-Aldrich) for 15 min protected from light. Cells were washed in PBS and imaged using a Zeiss LSM 780 Confocal Microscope - Inverted Microscope.

The cellular uptake was also evaluated by UV-VIS-NIR spectroscopy.⁽¹⁴⁹⁾ In this case, cells were plated in 6 well plate and, after 24 h, the media was replaced with fresh media containing PEG-AuNRs or CM- β -Lap-PEG-AuNRs with a final OD at 750 nm of 0.3. At each point time, the cells were rinsed three times with PBS to remove the excess of particles and detached from the wells using trypsin solution 2.5 g/L with EDTA. Next, the cells were centrifuged, resuspended in 1 mL of PBS buffer, and counted using a hemocytometer. The cells were centrifuged again and resuspended in hypotonic buffer (10 mM Trisbase, 1.5 mM MgCl₂, 10 mM NaCl), pH 6.8, for 5 min to lyse the cells, followed by sonication to break big molecular aggregates. The absorption was normalized by the number of cells at each point and is presented as media \pm standard derivation of three measurements.

3.2.12 Cytotoxicity

The cytotoxicity of the CM- β -Lap-PEG-AuNRs was evaluated using the colorimetric assays crystal violet (CV) and 3-(4, 5-dimethylthiazolyl-2)-2, 5-diphenyltetrazolium bromide (MTT). The same doses of PEG-AuNRs, CTAB-AuNRs, CM and CM- β -Lap were also tested in parallel for comparison. Three cell lines were used: the source cell (A549), another cancer cell (HTC) and healthy human hepatoma (HepaRG). All the cell lines were cultured in 96-well plate with a final volume of 200 μ L of media for 24 h at 37°C and 5 % CO₂. After this period, the media was changed by fresh media containing 5, 10 and 15 μ L of the samples in triplicate in a total of 100 μ L in each well and incubated for 24 h at 37°C and 5 % CO₂.

In brief, for the MTT assay, the wells were washed twice with PBS and incubated with 100 μ L of 0.5 mg/mL of MTT solution (Sigma-Aldrich, USA) for 4 h at 37 °C in a 5% CO₂. After, the MTT solution was carefully removed and replaced by 100 μ L of dimethyl sulfoxide (DMSO). Absorbance was measured at 570 nm on microplate reader SpectraMax M3 (Molecular Devices). For the crystal violet assay, after the incubation, the media was removed and the wells were washed twice with PBS, using a multichannel pipette, followed by fixation with ethanol 70% (10 min). The wells were washed twice with PBS and the cells were incubated with 40 μ L of violet crystal 0.5 % solution (Sigma-Aldrich) for 30 min at room temperature. After that, the wells were washed at least 5 times with PBS 1% to remove the excess of violet crystal and, finally, 100 μ L of acetic acid 10% were added and incubated for 30 min. After 1 min of gentle shaking, the absorbance of each well was determined using the microplate reader SpectraMax M3 (Molecular Devices) in 540 nm.

In both, the relative percentage of viable cells was calculated by considering the negative control as 100% of viable cells. For all samples and concentrations, the experiment was performed in triplicate and the assay was repeated two times for each period of incubation, resulting in six measurements for each concentration. The results were analyzed according with the media \pm standard derivation of all measurements for each concentration, and the values were statistically compared using the analysis of variance (ANOVA) and the Turkey test ($p < 0,05$) conducted with OriginPro 8 software.

3.2.13 Detection of Intracellular Reactive Oxygen Species (ROS)

The generation of reactive oxygen species (ROS) was evaluated by 2',7'-dichlorodihydrofluorescein diacetate (H₂DCFDA), a non-fluorescent molecule that is deacetylated by cytosolic esterases to a non-fluorescent compound dichlorodihydrofluorescein (H₂DCF), which in turn can be oxidized by ROS into a fluorescence molecule 2,7' – dichlorofluorescein (DCF). The cells were incubated with the samples for 2 hours, followed by rinsing with PBS. The cells were then incubated with 5 μ M of H₂DCFDA in cell culture media for 30 minutes at 37°C and 5 % CO₂, followed by washing with PBS. The fluorescence was then measured at excitation/emission wavelengths of 485/530 nm using a microplate reader SpectraMax M3 (Molecular Devices). The fluorescence intensity values were normalized by the relative number of cells determined by Crystal Violet and are presented as percentage considering the control as 100%.

3.3 RESULTS AND DISCUSSION

An overview on the different steps of the fabrication of the CM- β -Lap-PEG-AuNRs is shown in **Figure 3.4**. First, the A549 cancer cell membranes (CM) were extracted and purified by ultracentrifugation, followed by incorporation of the anticancer agent β -Lap. The gold nanorods were fabricated by the seed-mediated method in presence of CTAB and covalently functionalized with mPEG-SH. The fusion of the PEG-AuNRs and CM- β -Lap were performed by mechanical extrusion through 100 nm pore membrane.

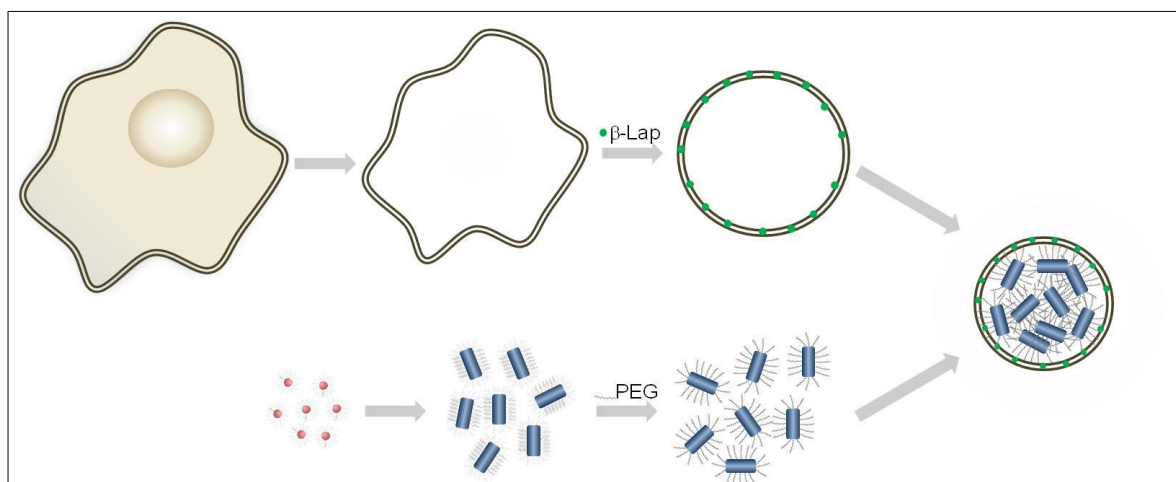


Figure 3.4 - Schematic representation (not to scale) of proposed mechanism for the fabrication of the cancer cell membrane-coated PEG-Gold nanorods and loaded with the anticancer agent β -Lapachone (CM- β -Lap-PEG-AuNRs). First, A549 lung cancer cells are isolated, lysed to remove the internal content and purified by ultracentrifugation. β -Lap is loaded on cell membrane structure and they are extruded through 200 nm porous membrane (CM- β -Lap). In parallel, gold nanorods (AuNRs) are synthesized by the seed-mediated method in presence of surfactant CTAB, followed by covalent functionalization with mPEG-SH. The fusion of the resulting PEG-AuNRs and CM- β -Lap are performed by mechanical extrusion through 100 nm pore membrane.

Source: By the author.

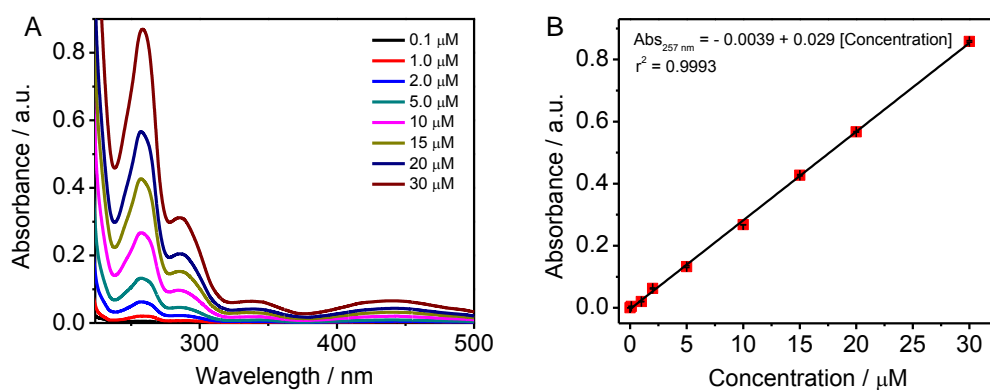


Figure 3.5 - a) Representative spectra of β -Lap in water:ethanol (1:1) in different concentrations and b) Calibration curve of β -Lap at 257 nm made from triplicate of the spectra in different concentrations.

Source: By the author.

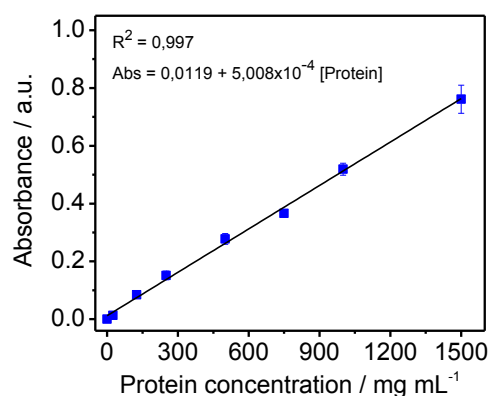


Figure 3.6 - Calibration curve of BSA protein obtained from bicinchoninic acid (BCA) assay and used to determine the protein concentration on the cell membranes vesicles (CM).

Source: By the author.

3.3.1 CM characterization

Cancer cell membrane vesicles (CM) were derived from A549 cancer cells. The reasoning for choosing this cell line as a source lies in their metastatic ability.(150) Cell-membrane-based systems have been shown to have the natural properties and some bio-functions from their parent cells.(151) Taking advantage of the inherent homotypic binding capability among tumor cells (18) and the metastatic characteristic of the A549 cells,(150) their derived membrane vesicles seem good candidates for enhance drug and nanoparticle delivery to the cancer and their metastatic sites.

The internal cell content was eliminated and the cells membrane was purified using hypotonic lysing, mechanical membrane disruption and ultracentrifugation. The removal of the internal components of the cell and the purification by ultracentrifugation is an important step to eliminate the safety concerns regarding the genetic material of cancer cells.(18) The vesicles were then formed by successive extrusion through 200 nm followed by 100 nm porous polycarbonate membrane.

The qualitative analysis of the cell membrane proteins was performed by polyacrylamide gel electrophoresis (SDS-PAGE), shown in **Figure 3.7A**. According to a previous study, the resulting vesicles appear to retain the critical cell membrane proteins.(18) The presence of specific and tumor-associate antigens from the source cancer cell line in the derivative vesicles have been confirmed in a previous study performed by Fang et al.(18) The quantitative analysis BCA of the proteins revealed a concentration of 774.9 µg/mL in the sample, which was used to standardize the amount of CM in the synthesis and experiments.

The analysis of the lipid content of the CM by latroscan TLC/FID revealed that phospholipids are the most abundant in the A549 cell membrane vesicle (**Figure 3.8**).

The next step was the loading of β -Lap into the CM structure. β -Lap is a very promising anticancer agent due mainly to its specific toxicity, which is activated by NADP(H):quinine oxidoreductase (NQO1), an enzyme overexpressed in many human cancers, such as lung, prostate, breast, and pancreas.(126) The loading of β -Lap is expected to overcome the problems associate with this agent, such as short blood circulation time, low stability in and poor specificity.(124) Several strategies have been developed for drug loading in cell membrane vesicles such as lipid fusion,(152) endocytosis,(153) and hypo-osmotic lysis method.(122) According to previous studies on fasudil-loaded erythrocytes nanovesicles, drug loading was significantly higher at 4°C compared to 25°C and 37°C.(122) Also, entrapment efficiency was essentially unaltered when formulations were centrifuged at 5000 rpm, but an increase in centrifugal force to 15000 rpm led to disruption of membrane and released of the drug.(122)

The loading was performed by incubation of the CM with β -Lap at 4°C, followed by extrusion through 200 nm porous membrane and dialysis. The hydrodynamic diameter measured by dynamic light scattering (DLS) after extrusion through 200 nm membrane confirms the formation of vesicles with an average diameter around 150 nm (**Figure 3.7B**). **Figure 3.7C** shows a comparison of the UV-VIS spectra of the CM before and after the loading of β -Lap. The CM spectrum presents a small absorption around 260 and 220 nm, which came from the proteins of the structure. After loading of the β -Lap, the observed spectrum represents a typical β -Lap spectrum with a strong absorption peak at 257 nm.

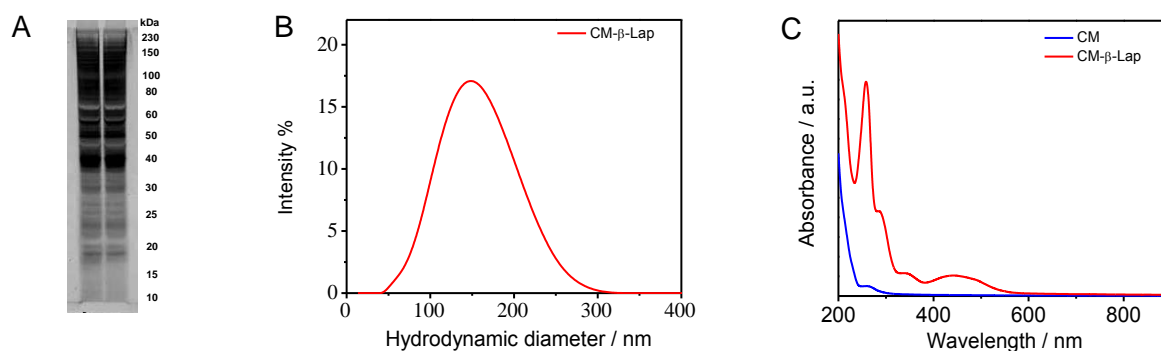


Figure 3.7 - Characterization of the A549 cell membrane (CM). (A) Polyacrylamide gel electrophoresis (PAGE-SDS) of the CM in duplicate. (B) Dynamic light scattering analysis of the CM- β -Lap after extrusion extrusion through 200 nm porous polycarbonate membrane, and (C) UV-VIS spectra of CM with/without β -Lapachone.

Source: By the author.

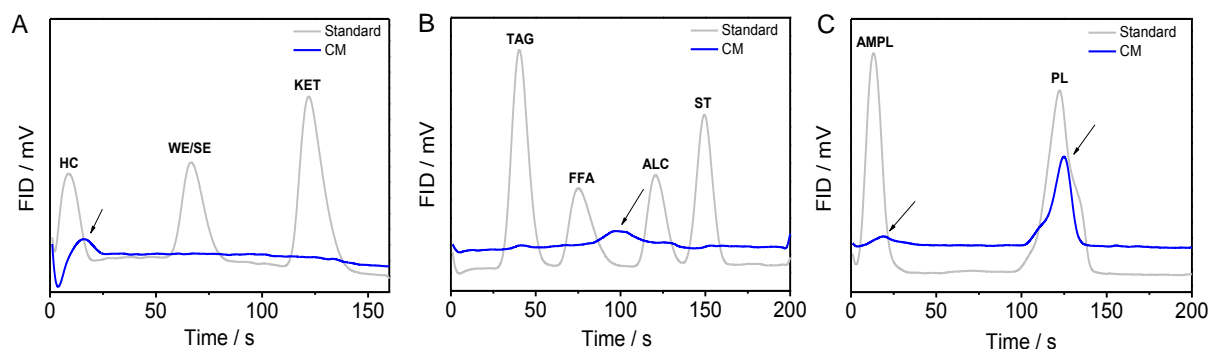


Figure 3.8 - Iatroscan TLC/FID chromatograms of standard lipids and A549 cell membrane (CM) samples.
Source: By the author.

3.3.2 Synthesis of CM- β -Lap-PEG-AuNRs

To synthesize CM- β -Lap-PEG-AuNRs, gold nanorods were first prepared by the seed-mediated method in presence of CTAB (72) and then covalently functionalized with mPEG-SH. PEG coating is highly hydrated and this layer avoid interactions of the nanoparticle with molecular and biological components of the biological media. Furthermore, as we will discuss shortly, the removal of the CTAB is important to avoid cytotoxicity and destabilization of the cell membrane vesicles.

A representative Scanning Electron Microscopy (FEG-SEM) image of PEG-AuNRs and the histograms determined by measuring about 100 particles by SEM images are shown in **Figure 3.9** and revealed no aggregation of the system after the PEGylation process. The calculated average aspect ratio (length/width) was approximately 3.5 and it is consistent with the extinction spectrum of the PEG-AuNRs (**Figure 3.10A**). The spectrum is typical of AuNRs, which exhibit two surface plasmon resonance (SPR). The band around 500 nm is due the coherent motion of the conduction band electrons along short axes (transversal band), while the band in the higher wavelength correspond to the oscillation long axes of the particle (longitudinal band).(35, 59-60)

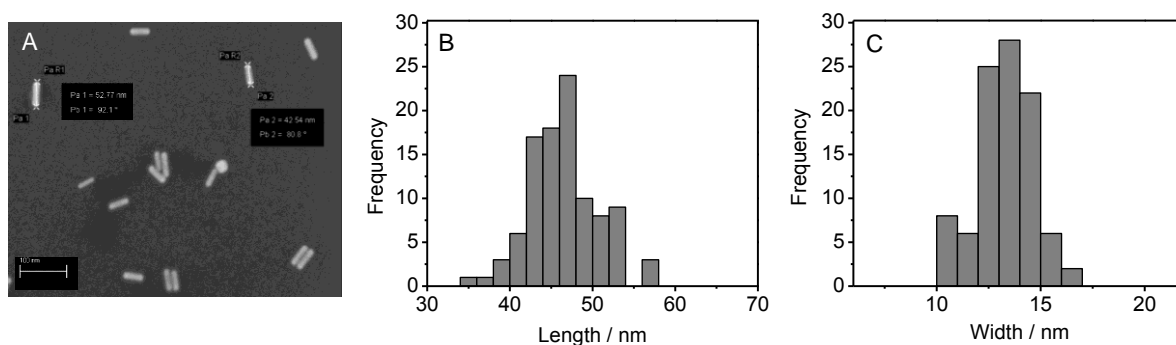


Figure 3.9 - (A) Representative FEG-SEM image of the PEG-AuNRs and (B) Histogram of length and (C) width determined by measuring about 100 particles using the software ImageJ. The average aspect ratio (length/width) calculated from the mean 47.4/13.37 was about 3.5.

Source: By the author.

The resulting PEG-AuNRs were subsequently fused with the CM- β -Lap derived vesicles through mechanical extrusion.(16) For this, CM- β -Lap and PEG-AuNRs were coextruded through a 100 nm polycarbonate membrane several times to guarantee the formation of homogeneous CM- β -Lap shell and completely coated particles. The CM- β -Lap/PEG-AuNRs ratio were varied to adjust the uniformity of the system and to avoid free AuNRs. After fusion, the system was washed by centrifugation to remove an eventual excess of CM- β -Lap and/or β -Lap. The total concentration of β -Lap in the final conjugates ($OD_{750\text{ nm}} = 0.6$) was around 2.5 μM . The low β -lap loading efficiency has also been observed in β -lap-loaded micelles and polymeric particles.(128) Recently, Zheng et al proposed a system for efficient loading and delivery of β -Lap using graphene oxides.(133)

A comparison of the UV-VIS-NIR spectra of PEG-AuNRs before and after the conjugation is shown in **Figure 3.10A**. A slightly red shift is observed in presence of the membrane and indicates the changing in the dielectric nature surrounding the nanorods.(154) More pronounced, however, is the changing in the intensity of the longitudinal plasmonic peak, which was significantly reduced. This effect has been attributed to the plasmon coupling effect, which is typically induced by gold nanorods assembly.(155) This interpretation matches with the FEG-SEM characterization (**Figures 3.10E-F**), which revealed that the AuNRs are grouped inside the cell membrane vesicles. The average diameter of CM- β -Lap-PEG-AuNRs, measured using the software Image J, was approximately 109 nm (**Figure 3.11**). FEG-SEM images of the CM-coated directly CTAB-AuNRs, i.e., without the PEGylation of the AuNRs, show a totally different assembly (**Figure 3.12**) and suggest a CTAB-mediated destabilization of cell membrane structure.

The controlled assembly of the nanomaterials have been shown to be an interesting way to fabricate systems with unique optical, electrical, and magnetic properties.(155-156) This effect has been particularly interesting for sensing applications. For example, Wang et al used controllable assemblies of AuNRs to detect an environmental toxin, called microcystin-LR (MC-LR).(155) For this, side-by-side and end-to-end assemblies were fabricated and when in presence of increasing concentrations of MC-LR, the assemblies were little by little being disrupted. They found a relationship between the size of the assembly and the intensity of the longitudinal peak with the concentration of MC-LR. Furthermore, although individual AuNRs are already considered excellent surface enhanced raman scattering (SERS) platforms with enhancement factors on the order of 10^4 - 10^5 due their anisotropic shape, their assemblies have provided unique SERS enhancing properties.(157) The assembly creates coupled plasmon modes, which results in regions of enhanced electromagnetic field, known as hot spots, at the junctions.(157)

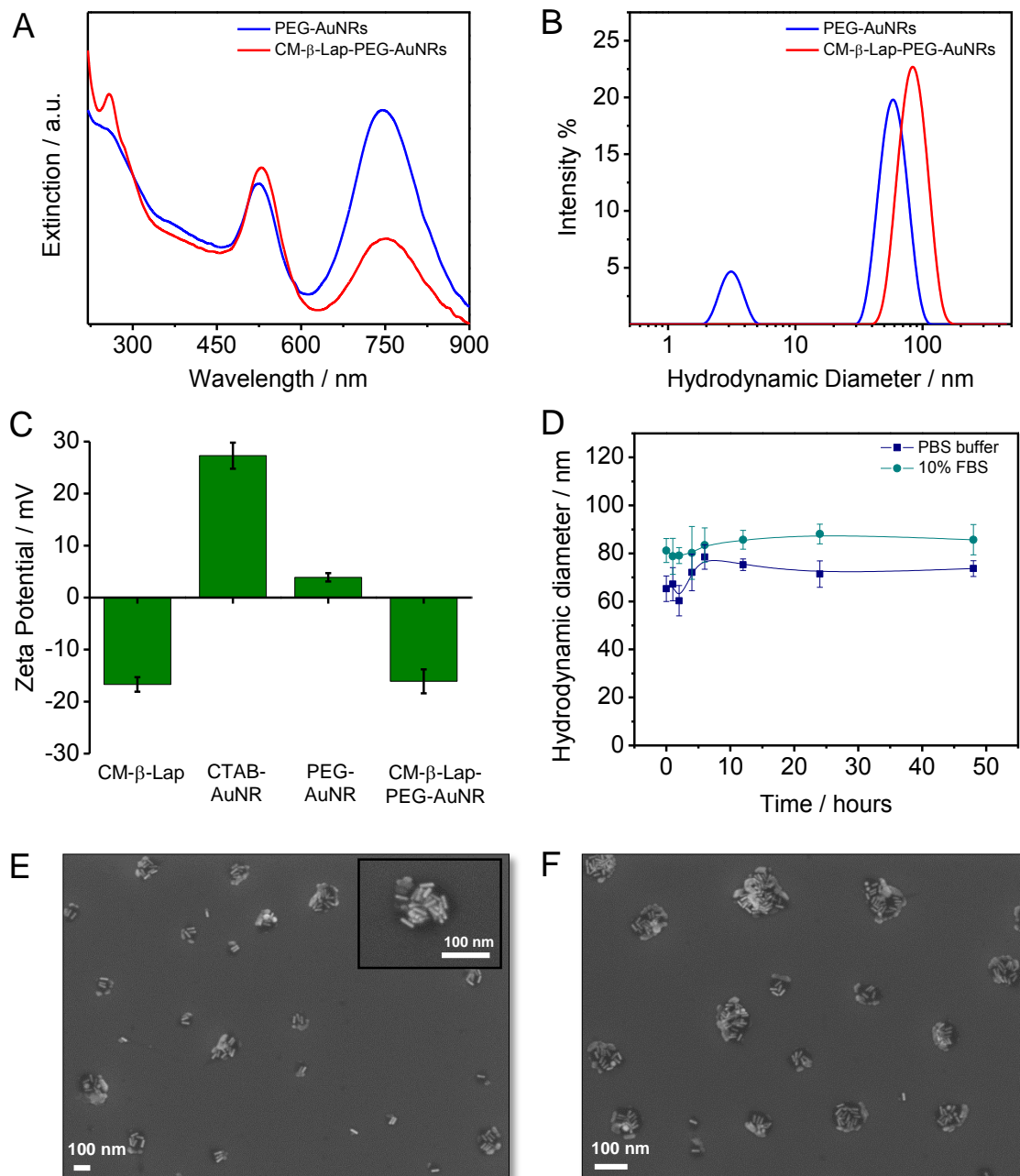


Figure 3.10 - Characterization of gold nanorods coated with cell membrane loaded β -Lapachone (CM- β -Lap-PEG-AuNRs) and comparison with PEG-AuNRs. (A) UV-VIS-NIR spectra and (B) hydrodynamic diameter obtained from DLS measurements of PEG-AuNRs before and after coating with CM- β -Lap. Longitudinal plasma resonance of PEG-AuNRs ($\lambda_{\text{max}} \sim 750$ nm) decreased after the coating. C) Zeta potential of the AuNRs before and after functionalizations, D) stability of CM- β -Lap-PEG-AuNRs in PBS buffer and 10% Fetal Bovine Serum; (E) and (F) FEG-SEM images of CM- β -Lap-PEG-AuNRs showing the PEG-AuNRs grouped inside the cell membrane vesicles.

Source: By the author.

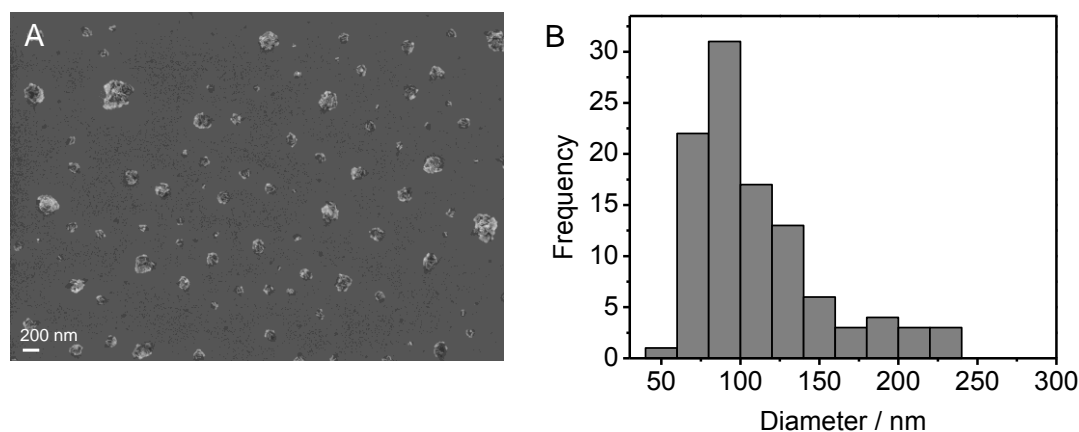


Figure 3.11 - (A) Representative FEG-SEM image of CM- β -PEG-AuNRs and (B) histogram determined by measuring about 100 particles using the software ImageJ. The average diameter calculated was about 109 nm.

Source: By the author.

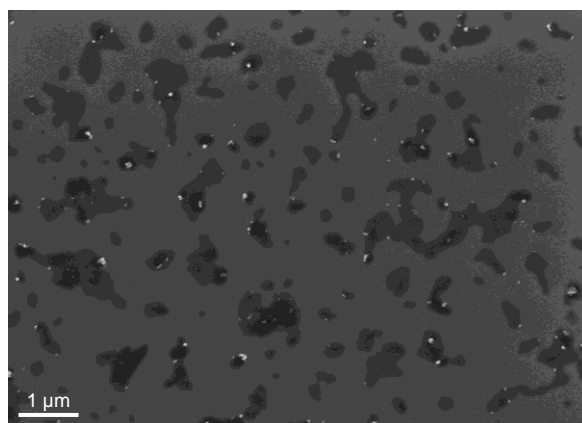


Figure 3.12 - Representative FEG-SEM image of the CM- β -Lap-coated CTAB-AuNRs. No spherical cell membrane vesicles are observed, suggesting their destabilization in presence of the surfactant CTAB.

Source: By the author.

A comparative analysis of the hydrodynamic diameter of PEG-AuNRs with/without CM- β -Lap by DLS measurements is shown in **Figure 3.10B**. The fixed angle of the DLS instrument does not represent the true physical dimensions of the rod-shape particles, because the hydrodynamic diameter can only be calculated by Stokes–Einstein equation for spherical systems. However, the diffusion coefficient determined is still accurate and this technique can be applied for a comparative analysis as demonstrated by Liu et al in the study of nanorod-protein interactions.(158) Before the fusion, the PEG-AuNRs presented two different size

distributions, which is consistent with their anisotropic shape, while the final CM- β -Lap-PEG-AuNRs presented only one size distribution around 100 nm and agrees with the previous results that show the assembly of the PEG-AuNRs inside the spherical vesicles.

The functionalization was further confirmed by zeta potential measurements (**Figure 3.10C**). The cell membrane presented a negative charge due mainly to the presence of phospholipids and proteins. The zeta potential of AuNRs changed from highly positive, due the CTAB stabilization, to close to zero after PEGylation. The surface charge of the PEG-AuNRs upon fusion with CM- β -Lap was about the same of the CM- β -Lap vesicles, suggesting successful coating.

To examine the serum stability of the resulting CM- β -Lap-PEG-AuNRs, they were resuspended in 1x PBS and 100% FBS solution and the hydrodynamic diameter was monitored by DLS. All samples were incubated at 37°C and gently shaken prior the measurements (**Figure 3.10D**). No major change was observed, indicating that the CM- β -Lap-PEG-AuNRs present good stability either in buffer or biological media. The ability of CM- β -Lap-PEG-AuNRs to avoid the binding of proteins from the biological media was evaluated by Isothermal titration calorimetry (ITC) (**Figure 3.13**). The interactions between bovine serum albumin (BSA), a major representative globular protein present in the serum, and PEG-AuNRs, CM- β -Lap-PEG-AuNRs, and CTAB/PEG-AuNRs were evaluated. CTAB/PEG-AuNRs consist in the PEGylation of the CTAB-AuNRs using a lower concentration of mPEG-SH, i.e., just enough to keep the particles stable in 0.1x PBS, resulting in a zeta potential of +18 mV. In the tested conditions, no interaction was observed for PEG-AuNRs and CM- β -Lap-PEG-AuNRs, while the binding between BSA and CTAB/PEG-AuNRs is an exothermic process. It is expected that the PEGylation of nanoparticles would reduce protein adsorption on the nanoparticle surface as a result of steric repulsions and hydrophilization induced by PEG chains, and previous studies have also shown no heat exchange when BSA is added to PEGylated nanoparticles.(148, 159) Since the CM- β -Lap-PEG-AuNRs presented a similar behavior, we can infer that they also have some properties characteristic from PEGylated particles such as stability in physiological media and ability to avoid the BSA binding. These results suggested that the coating of the nanoparticles with cancer cell membrane vesicles may avoid the opsonization. However, further and more detailed studies need to be performed to prove this hypothesis.

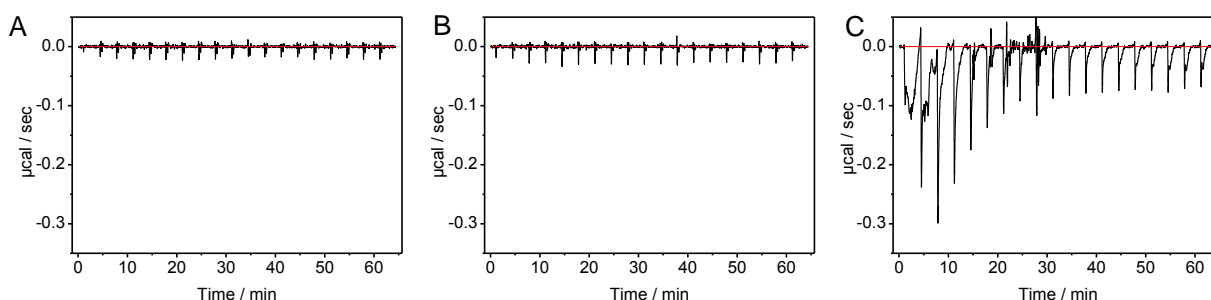


Figure 3.13 - Plots of heat flow vs time of microcalorimetric titration of (a) PEG-AuNRs; (b) CM- β -Lap-PEG-AuNRs and (c) CTAB/PEG-AuNRs by BSA solution. Injections of 2 μ L, at 25 $^{\circ}$ C, of 0.01 mM of BSA solution were made on nanoparticles suspensions. Control of BSA dilution was carried out by injections of BSA solution in buffer.

Source: By the author.

Together, these results demonstrate that the coating was efficient and the gold nanorods are grouped inside the cell membrane vesicles. According to previous studies,(17-18) the coating of nanoparticles with natural cell membrane occurs with the accurate transference of the membrane bilayer structure onto the particle surface, leading to a right-side-out conformation. This is important to maintain the surfaces antigenic diversity and functions of source cells, besides the increased stability in biological media and longer circulation time. Furthermore, the cell membrane vesicles prepared by this approach present some advantages with respect to the exosomes, such as versatility to be made in different sizes and loaded with many types of therapeutic agents, and reproducibility, all clinically relevant characteristics.(20) Also, exosomes may lead to more safety concerns due to their more complex content, such as miRNA.

3.3.3 Photothermal properties

Photothermal therapy has been increasingly investigated as a minimally invasive alternative for cancer treatment.(7) Having verified the formation of the CM- β -Lap-PEG-AuNRs conjugates, we investigated their photothermal properties using a 808 nm laser at a power density of about 1.5 W/cm², which is consistent with earlier experimental conditions used in PPTT to guarantee minimal side effects,(55,105,160) and an optical thermometer to monitor the temperature. The 808 nm wavelength overlaps with the longitudinal absorption band of the AuNRs and it is important due to the low absorption of the tissue in the NIR.(8)

Equal optical densities (OD) have been shown to be an appropriated method to compare the photothermal properties of nanoparticles.(10) **Figure 3.14A** shows that as the suspensions of CM- β -Lap-PEG-AuNRs and PEG-AuNRs, both with OD_{750 nm} of about 0.6,

were exposed to NIR laser, the temperature in both systems increased. Closer examination revealed some slight differences mainly in the initial period (**inset of Figure 3.14A**). First, the curve slope in the first minutes after laser was turned on was greater for PEG-AuNRs than to CM- β -Lap-PEG-AuNRs, but after about 2.5 min, they seem to be almost the same. This could be ascribed to the assembly of nanorods observed on CM- β -Lap-PEG-AuNRs system. Initially, the AuNRs are grouped inside the CM vesicles, which decrease their absorption at NIR region (**Figure 3.10A**). The temperature increases generated by the laser irradiation would destabilize the cell membrane structure and release both PEG-AuNRs and β -Lap, and as they are being released, their photothermal behavior is becoming more likely the free PEG-AuNRs. Besides the assembly of the gold nanorods, the cell membrane layer by itself contributed to the slower temperature rise of CM- β -Lap-PEG-AuNRs compared to their PEGylated counterparts, i.e., the additional biological layer may hamper the heat dissipation into the surrounding media.⁽¹⁶¹⁾ The CM- β -Lap-PEG-AuNRs also take more time to stabilize, which suggest that some changes in their structure still occur even after 10-15 min of irradiation. No significant temperature change was observed when buffer solution (data not shown) or cell culture media were irradiated with the NIR laser at the same conditions.

The FEG-SEM images before and after 10 and 25 min of laser irradiation shown in **Figure 3.14D-F**, respectively, clearly show the gradual release of the PEG-AuNRs from the CM vesicles with the laser irradiation time. It is worth stressing that the laser irradiation did not cause any shape modification, i.e., in size and morphology of the AuNRs. This is important since a laser irradiation sufficient to modify the structure of the nanoparticles is probably able to induce cell death and side effects. Moreover, it has been shown that the smaller nanoparticles resulting from this reshaping process present high cytotoxicity.⁽¹⁶²⁾

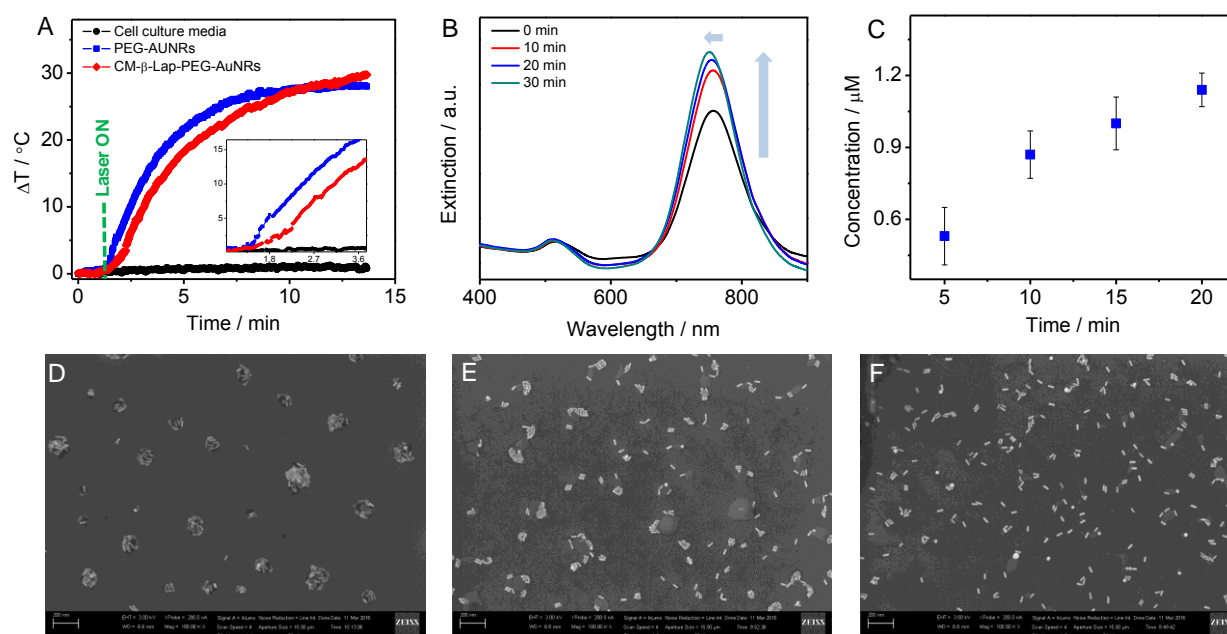


Figure 3.14 – (A) Representative of temperature change vs time in suspensions (optical density at 750 nm = 1) irradiated with 808 nm laser with power density of 1.5 W/cm², (B) Increase of the longitudinal band with the laser irradiation, (C) release of β -Lapachone at different time of irradiation. SEM images of CM- β -Lap-PEG-AuNRs (D) before, (E) after 10 min and (F) after 20 min of laser irradiation. The laser irradiation increases the temperature of the suspension, breaks the vesicles and causes the release of the AuNRs.

Source: By the author.

The increasing in the longitudinal band of the AuNRs with the increasing of the laser irradiation (**Figure 3.14B**) is expected and also revealed the disruption of the cell membrane vesicles and release of the PEG-AuNRs. Taken together, these results show that CM- β -Lap-PEG-AuNRs present a slower temperature rise compared to their PEG-AuNRs, but the disruption of the membrane occurs in the first minutes of NIR irradiation, and their behaviors become equals.

The release of β -Lap was analyzed by dividing the sample in four aliquots, irradiating them with the laser for different times, centrifuging them immediately to separate the released β -Lap from the nanoparticles using centrifugal filters, and measuring the typically absorbance of the β -Lap at 257 nm to calculate the correspondent concentrations. The calculated released concentrations with the laser irradiation time are shown in **Figure 3.14C**. As expected, the amount of β -Lap released increases with the irradiation time, which is in good accordance with previous studies.(55,163) Accordingly, laser-induced release of molecules on surface of gold nanorods is a thermal process and the amount of released molecules is dependent upon the laser power and period of irradiation.(55,163) However the total concentration of β -Lap

released from CM- β -Lap-PEG-AuNRs is very low ($< 1.2 \mu\text{M}$) even after 20 min of irradiation.

3.3.4 *In vitro* photothermal therapy

For the *in vitro* photothermal therapy experiments we have used the same optical density for both samples with/without β -Lap (final $\text{OD}_{750 \text{ nm}}$ in cell culture media = 0.3), which allows quantitative comparison of the photothermal properties for all systems.⁽⁵⁵⁾ The cells were incubated for 4 hours with the particles, washed twice with PBS, and left in cell culture media. After 10 min of irradiation, the cells were incubated for 2 h at 37°C and 5% CO_2 , followed by staining with trypan blue to evaluate the viability (**Figure 3.15, 3.16**). Surprisingly, an increasing number of dead cells stained by trypan blue are observed for cells treated with CM- β -Lap-PEG-AuNRs compared to the cells treated with CM-PEG-AuNRs. Since the only difference between these two systems is the presence of β -Lap, we can infer that even at low concentrations (probably below $1 \mu\text{M}$), the β -Lap is contributing for the toxicity of the CM- β -Lap-PEG-AuNRs and apparently it has been released only after laser irradiation. It is noteworthy that only the cells in the laser spots (highlight areas) were damage.

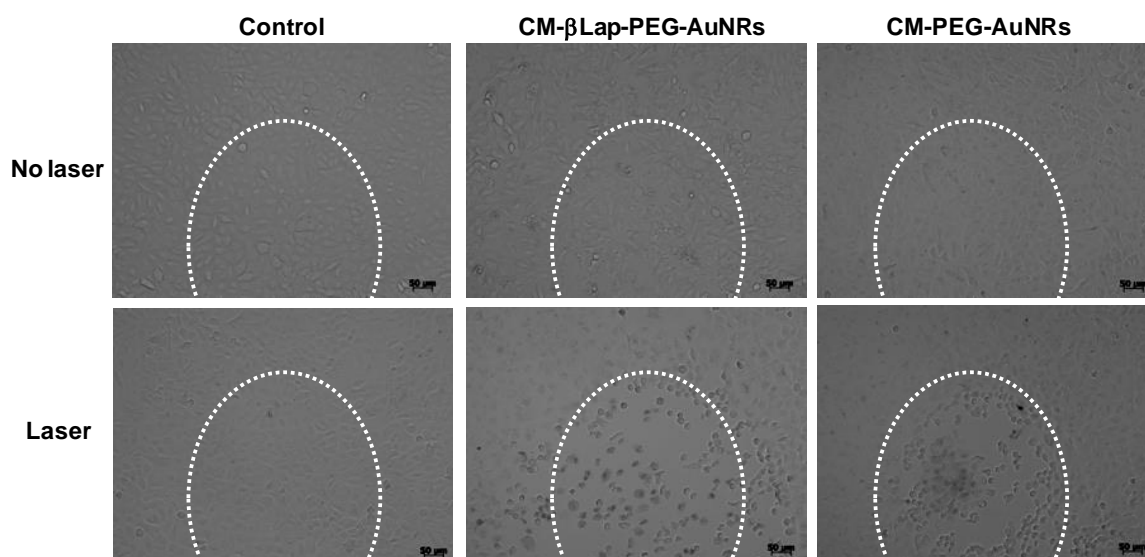


Figure 3.155 - Photothermal therapy of A549 cancer cells treated with CM- β -Lap-PEG-AuNRs and CM-PEG-AuNRs. The highlight areas represent approximately the laser spots ($\sim 1.5 \text{ W/cm}^2$, 10 min) on the samples. Dead cells were stained with Trypan Blue. Cells without the particles are not affected by the laser irradiation while cells incubated with CM- β -Lap-PEG-AuNRs and CM-PEG-AuNRs were visibly injured.

Source: By the author.

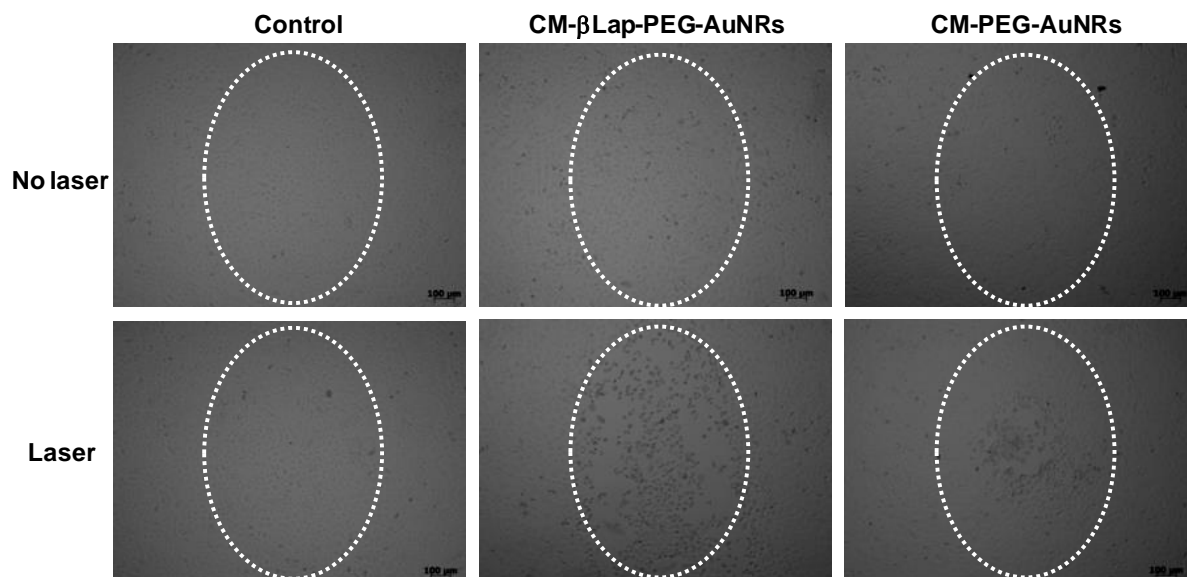


Figure 3.16 - Photothermal therapy of A549 cancer cells treated with CM- β -Lap-PEG-AuNRs and CM-PEG-AuNRs for 4 h. The highlight areas represent approximately the laser spots ($\sim 1.5 \text{ W/cm}^2$, 10 min) on the samples. Dead cells were stained with Trypan Blue. Cells without the particles are not affected by the laser irradiation while cells incubated with CM- β -Lap-PEG-AuNRs and CM-PEG-AuNRs were visibly injured.

Source: By the author.

It is known that the cytotoxicity effect of β -Lap is depending on NAD(P)H:quinone oxidoreductase (NQO1), which is overexpressing in several cancers, including A549 lung cancer cell line.(124) Park et al have been shown that heating the cells at mild temperatures ($41\text{-}42^\circ\text{C}$) elevates NQO1 expression in various cancer cells, including A549, increasing the anticancer effects of β -Lap.(127) Accordingly, heating the cancer cells to 42°C increased the NQO1 level for 1 h and remained elevated for 72 h. This might explain the significant effect of β -Lap in the cytotoxicity of A549 cells, even at very low concentrations. Also, it highlights that more than only two combined effects (photo and chemotherapy), the CM- β -Lap-PEG-AuNRs can act as a synergistic system: the temperature increases resulted from the plasmonic properties of AuNRs may enhance the anticancer properties of the β -Lap.

The delivery of chemotherapeutic drugs and photothermal agents has been shown to be an effective therapeutic approach for combined cancer treatment.(104, 164) The results presented in **Figures 3.15 and 3.16** collectively demonstrated the effectiveness of CM- β -Lap-PEG-AuNRs as a multifunctional agent for combined chemo and photothermal destruction, achieving synergistic cancer treatment.

3.3.5 Cellular uptake

After investigation of the *in vitro* photothermal properties, the ability of the CM- β -Lap-PEG-AuNRs to target and uptake A549 cancer cells were analyzed. First, the uptake was investigated by fluorescence confocal analysis. CM were stained with CellMaskTM plasma membrane stain (Invitrogen), which consists in amphipatic molecules, and then conjugated with the PEG-AuNRs as described previously. For this specific confocal experiment, CM were not loaded with β -Lap, since the goal was observe only the internalization ability and the β -Lap could interfere in the label with the fluorophore. The confocal image of A549 cells incubated with CM- β -Lap-PEG-AuNRs for 4 hours (**Figure 3.17A**) shows that the particles were internalized and localized in the cell cytoplasm. The discrete red spots in the cytoplasm may be an indicative of endosomal uptake of the CM-PEG-AuNRs inside de cells.(46) In **Figure 3.18**, the strong signal observed for CM-PEG-AuNRs when nucleus is in focus (middle rows) confirms the cellular uptake. These observations corroborate a previous study in which MDA-MB-435 cell membrane-coated PLGA nanoparticles were incubated with MDA-MB-435 cells.(18)

Since not much information is available about CellMask stain and to elucidate whether the excess of the fluorophore was removed or whether CellMask could be release from the CM vesicles in the presence of the cells, we performed the same experiment using only the CellMask stain as a control. The cells were treated with high concentrations of CellMask and incubated for 4 hours. Confocal images comparing both systems are shown in **Figure 3.20**, and revealed differences between them. In the 3D images (**Figures 3.20C, 3.20F**), these differences are even more evident, showing that in the A549 cells incubated with only CellMask stain the red dots are in the cell membrane and not in the cytoplasm like CM- β -Lap-PEG-AuNRs.

Since the plasma membrane stain could alter the surface of the CM and, consequently, the uptake, the internalization of CM- β -Lap-PEG-AuNRs was further evaluated by UV-Vis-NIR spectroscopy. This simple method has been shown to be very useful to investigate the uptake of plasmonic nanostructures and, according to previous studies, the concentrations of nanoparticles determined is consistent with those obtained by inductively coupled plasma mass spectrometry (ICP-MS).(149) The cells were incubated with PEG-AuNRs and CM- β -Lap-PEG-AuNRs with a final OD at 750 nm of 0.3. Based on the optical properties of both systems shown in **Figure 3.10A**, we probably have used a higher concentration of AuNRs at

CM- β -Lap-PEG-AuNRs compared to PEG-AuNRs, and therefore this method was used only as a comparative and qualitative analysis. At each point time, cells were lysed in hypotonic buffer, followed by sonication to break big molecular aggregates. The absorption was normalized by the number of cells at each point. **Figure 3.17B** shows time dependence of the extinction at 750 nm of the cells treated with CM- β -Lap-PEG-AuNRs, i.e., extinction at 750 nm increases with the incubation time. In **Figure 3.17C**, which represents the extinction spectra of the cells incubated with PEG-AuNRs and CM- β -Lap-PEG-AuNRs for 4 h corrected by the number of cells and normalized, the extinction of CM- β -Lap-PEG-AuNRs was obviously superior compared to PEG-AuNRs.

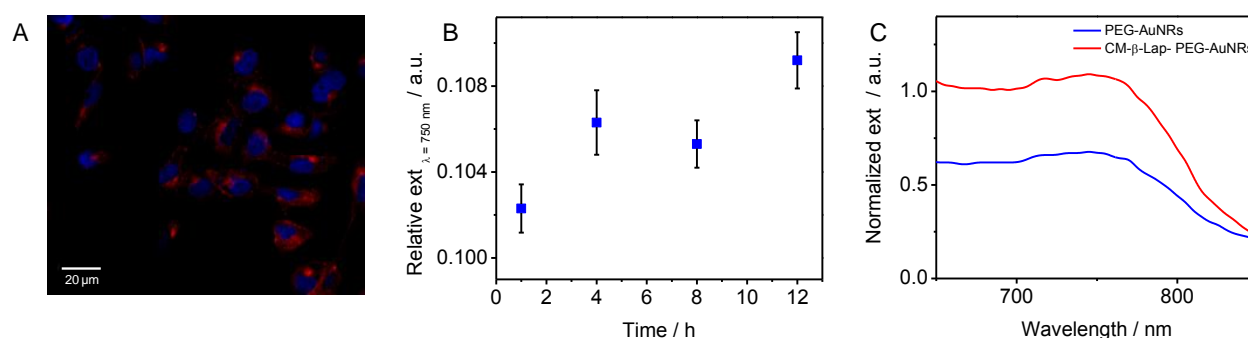


Figure 3.17 - (A) Confocal images of A549 cells after cell exposure to CM-PEG-AuNRs for 4 h. Blue: cell nuclei (Hoechst 33258). red: CellMask Deep Red-labeled CM-PEG-AuNRs (Exc/Em = 649/667 nm). (B) Time dependence of the extinction at 750 nm of the cells treated with CM- β -Lap-PEG-AuNRs, showing the dynamic of the uptake of the particles. The data were corrected by the number of cells (relative ext) and are showed as mean \pm SD of triplicate. (C) Comparison of the uptake of PEG-AuNRs and CM- β -Lap-PEG-AuNRs after 4 h of incubation. The extinctions were corrected by the number of cells and normalized.

Source: By the author.

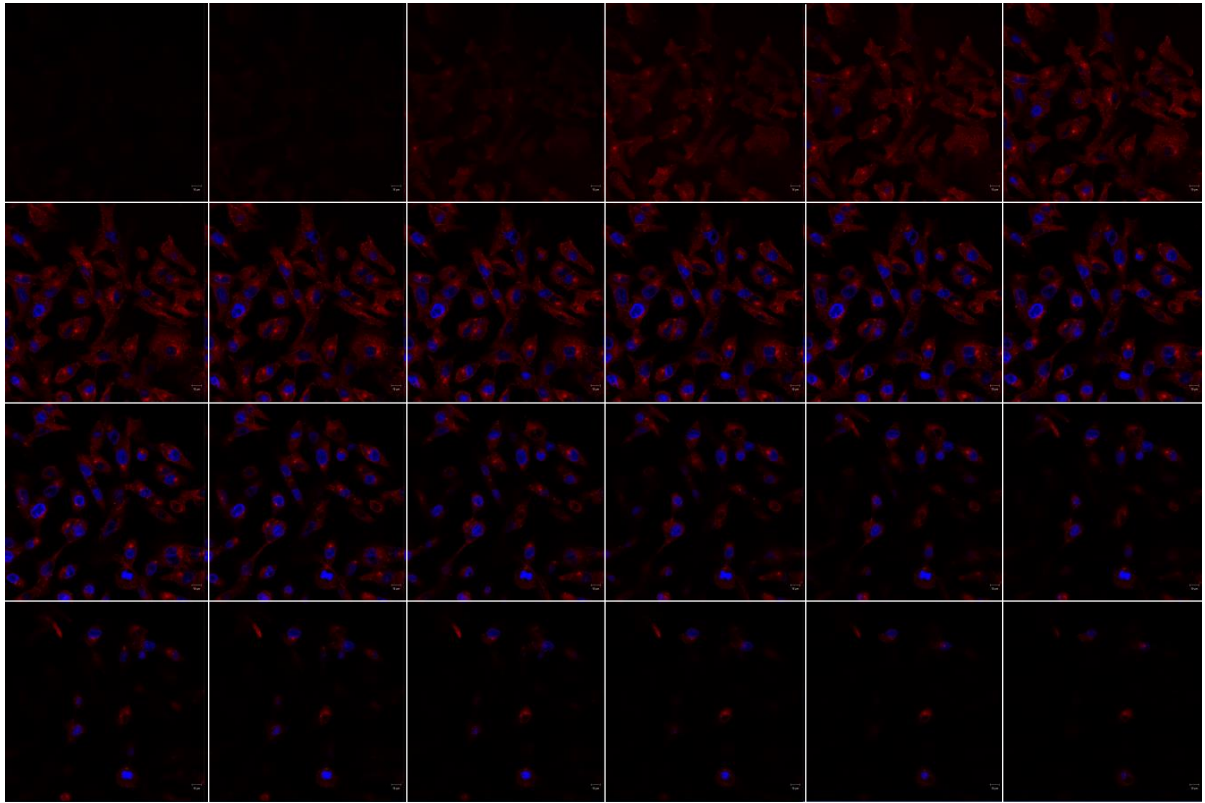


Figure 3.18 - Intracellular uptake of CM-PEG-AuNRs. Samples were incubated with A549 cells for 4 h. Red: CellMask Deep Red-labeled CM-PEG-AuNRs (Exc/Em = 649/667 nm); Blue: nuclei stained with Hoechst 33258. CM-PEG-AuNRs show strong signal when nucleus is in focus (middle row), demonstrating cellular uptake.

Source: By the author.

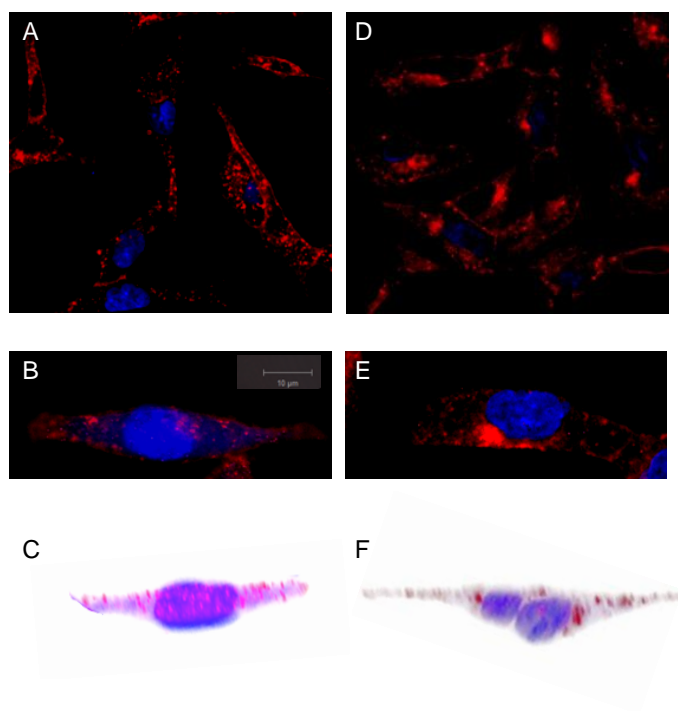


Figure 3.1916 - Confocal images of A549 cells after cell exposure to CellMask Deep Red stain (a, b, c) and CellMask-stained CM-PEG-AuNRs (d, e, f) for 4 h. Blue: cell nuclei (Hoechst 33258).

Source: By the author.

Together, these analyses provide evidence that the functionalization with CM facilitates the uptake in the source cells. This observation is in agreement with previous studies in which it is shown that MDA-MB-435 cell membrane-coated PLGA polymeric nanoparticles presents a significantly higher uptake in MDA-MB-435 cells compared to both bare PLGA nanoparticles and red blood cell membrane-coated PLGA nanoparticles.(18) According to the authors, the coating of nanomaterials with cancer cell membrane can preferentially increase their affinity to the source cancer cells and they attributed this effect to the transference of cell adhesion molecules with homotypic binding properties.(18) Since many cancer cells express surface antigens with hemophilic adhesion domains,(165) which are responsible for multicellular aggregate formation in tumors, we believe that this effect could also be responsible for the increasing uptake of CM- β -Lap-PEG-AuNRs compared to PEG-AuNRs. Furthermore, the applications of this new system could be optimized and extended for other applications, such as radiotherapy, since β -Lap has shown to be a very promising anticancer agent for radiosensitization.(134, 166-167)

3.3.6 Cytotoxicity

To evaluate the safety of the CM- β -Lap-PEG-AuNRs, their cytotoxicity in absence of laser irradiation was investigated using two colorimetric assays: crystal violet (CV) and MTT. Equivalent doses of PEG-AuNRs, CTAB-AuNRs, CM and CM- β -Lap were tested in parallel for comparison. The goal was to analyze the behavior of the CM- β -Lap-PEG-AuNRs against their source cell (A549), another type of cancer cell (HTC), and a healthy one (HepaRG). The results are shown on **Figure 3.20A-B** and reveal a good agreement between both assays. No significant cytotoxicity for any of tested samples was observed, except for CTAB-AuNRs. The cationic surfactant CTAB has been shown to be very toxic to cells at very low concentrations.(168) The complete removal of CTAB from AuNRs and their functionalization with other molecules is a crucial step to guarantee stability and biocompatibility for medical applications. The results proved that PEGylation and CM coating of the AuNRs were efficient to prevent cytotoxicity at the tested concentrations.

In agreement with data in the literature,(124, 128, 130) the specific toxicity of β -Lap for cancer cells was found (**Figure 3.20C**). β -Lap induced cell death of A549 and HTC cells at a concentration of 4 and 8 μ M, while HepaRG showed to be more resistant. For A549 cells, it is possible to observe that while a dose of 8 μ M causes a cell death of more than 50 %, 4 μ M or 2 μ M has almost no effect. These sharp dose-responses of β -Lap have been reported.(169) It is worth to emphasize that neither CM- β -Lap nor CM- β -Lap-PEG-AuNRs present any significant toxicity, which indicates that the concentration of β -Lap released from these structures in absence of laser irradiation is very low.

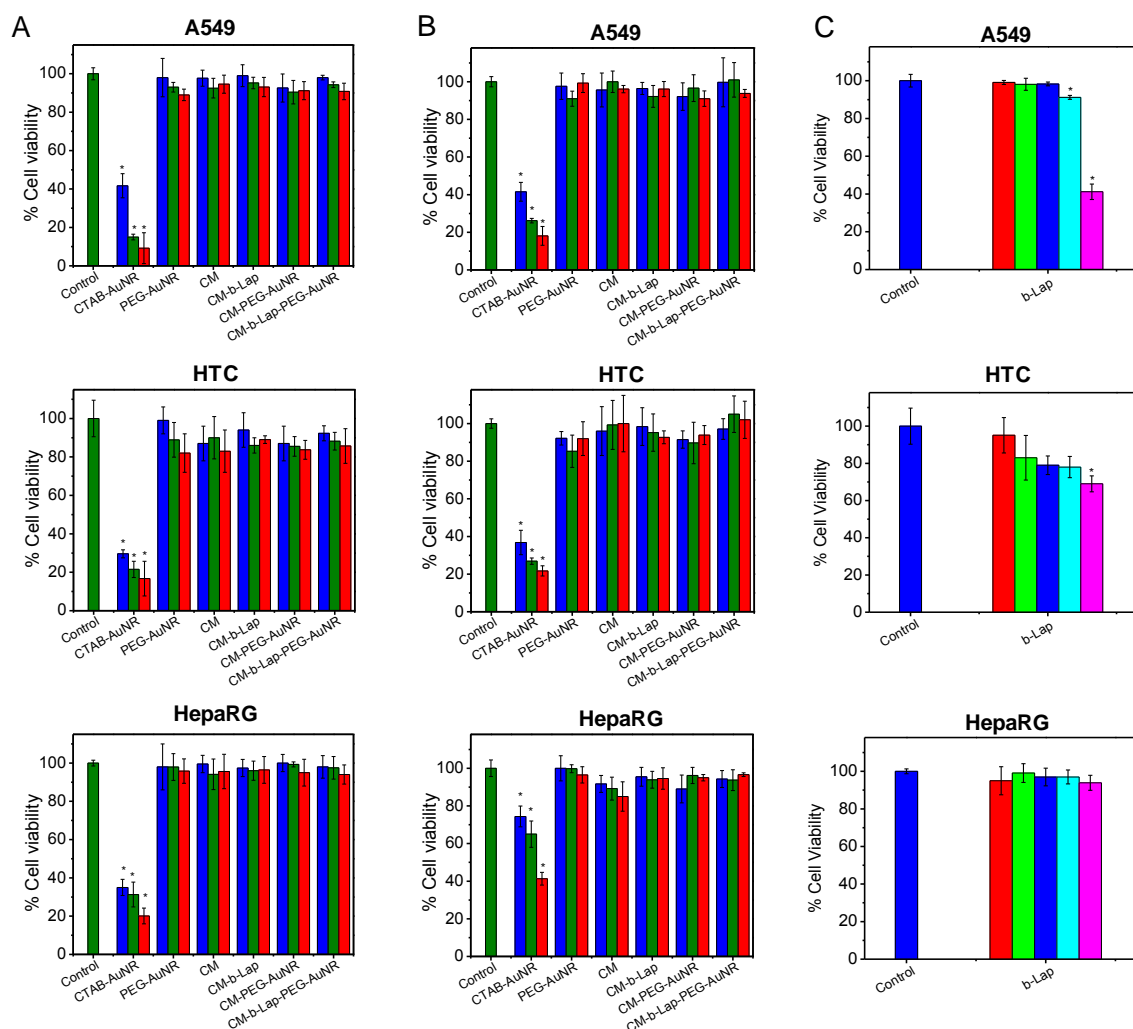


Figure 3.170 - Cell viability, evaluated by (a) MTT; (b) Crystal Violet, and (c) MTT of A549, HTC and HepaRG cells after incubation with the samples for 24 h. In (a) and (b) the columns blue, green, and red represent the quantities of 5, 10 and 15 μL , respectively. In (c) the columns red, green, blue, light blue and pink represents the concentrations of 0.5, 1.0, 2.0, 4.0 and 8.0 μM of $\beta\text{-Lap}$, respectively. The relative percentage of viable cells was calculated by considering the control as 100% of viable cells. The results represent the mean \pm SD of data normalized to untreated controls from two independent experiments in triplicate. * $P < 0.05$ with respect to untreated controls.

Source: By the author.

3.3.7 Detection of Intracellular Reactive Oxygen Species (ROS)

One of the mechanisms of $\beta\text{-Lap}$ toxicity proposed in literature is through the generation of ROS. NQO1 metabolizes $\beta\text{-Lap}$ to a very reactive hydroquinone, which is oxidized back to semiquinone or quinone in a futile cycle metabolism.(169) In this process, semiquinones, free radical generators, initiate the redox cycle, and ROS including superoxide and hydrogen peroxide are then generated.(170) The effect of $\beta\text{-Lap}$ after conjugation with CM- $\beta\text{-Lap}$ or CM- $\beta\text{-Lap}$ -PEG-AuNRs was evaluated by 2',7'-dichlorodihydrofluorescein

diacetate (H₂DCFDA) and compared with free β -Lap (**Figure 3.21**). The data reveal that β -Lap increased the intracellular ROS generation only in A549 and HTC cells, but not in HepaRG cells, and no significant ROS was generated by CM- β -Lap or CM- β -Lap-PEG-AuNRs, which is in good accordance with the cytotoxicity results.

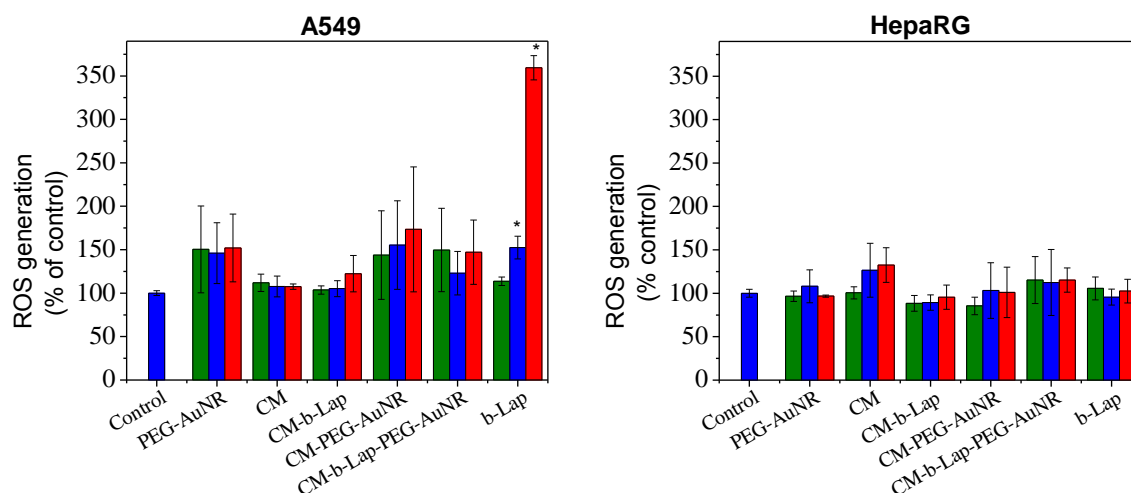


Figure 3.21 - Measurement of generation of ROS in A549 and HepaRG cells. (a) Cells were incubated with the samples for 2 hours and the generation of ROS was measured using the 2',7'-dichlorodihydrofluorescein diacetate (H₂DCFDA) assay. The relative percentage was calculated by considering the control as 100%. Data are expressed as mean \pm SD of triplicate from two independent experiments. * $P < 0.05$ with respect to untreated controls.

Source: By the author.

The effect of the ROS generation by β -lap has been widely investigated. Park et al suggest that upregulation of intracellular ROS is involved in β -Lap induced programmed necrosis, called necroptosis.(170) Early study demonstrated by comet assay that accumulation of ROS such as hydroxyl radicals generated by β -lap-loaded PEG-PLA as well as free β -lap causes severe DNA damage.(128)

3.4 CONCLUSIONS

We have demonstrated the successful coating of PEG-AuNRs into cellular membranes vesicles purified from A549 cancer cells and loaded with the anticancer agent β -Lapachone. The characterization of the system demonstrated the assembly of PEG-AuNRs inside the vesicles and NIR irradiation led to disruption of the vesicles and release of the PEG-AuNRs and β -Lapachone. *In vitro* studies also revealed that this multifunctional noncovalent platform was capable to deliver therapeutic molecules and plasmonic nanostructures upon NIR

irradiation, resulting in an enhanced cytotoxicity against A549 cancer cells. The NQO1-specific cytotoxicity of β -Lap combined with heat generated by laser irradiation of the AuNRs result in a synergic toxicity specific for cancer cells. No cytotoxicity was observed in absence of laser irradiation. Further studies would be focus on the optimization of the loading of β -Lap and a detailed investigation of their *in vitro* and *in vivo* photothermal cytotoxicity mechanism.

The system we describe differ from others that already exists mainly because of the toxicity activated by NIR radiation and the synergic effect demonstrated between the heat generated by laser irradiation and β -Lapachone activity. Its major potential advantages consists in its specific toxicity against cancer cells added to its capability to avoid opsonization and target specific cancer sites, versatility and multifunctionality, allowing the fabrication with different plasmonic systems. The system can mimic the cancer cells properties and represents new opportunities for the development of more efficient methods for diagnosis and treatment of cancer, increasing the chances of a successful therapy with reducing side effects. Furthermore, this multifunctional platform for activated drug release and phototherapy is a promised candidate for applications in personalized medicine. Other potential utilizations may include radiotherapy, photodynamic therapy, and two photon luminescence imaging.

4 Gd(III)-ENCAPSULATING Au NANOMATRYOSKHAS: ENHANCED T₁ MAGNETIC RESONANCE CONTRAST IN A THERANOSTIC NANOPARTICLE

4.1 INTRODUCTION

4.1.1 Magnetic Resonance Imaging (MRI)

Magnetic resonance imaging (MRI) is currently the most used biomedical imaging modality.(21) It is a non-invasive technique with contrast versatility and high spatial and temporal resolution.(22) Unlike X-Ray Computer Tomography, Single-Photon Emission Computed Tomography or Positron Emission Tomography, no harmful high-energy radiation is used in MRI.(171)

MRI derives directly from nuclear magnetic resonance (NMR), a widely used technique to determine molecular structure. MRI focuses in one type of atomic nucleus, the hydrogen in H₂O, termed “H proton”.(21) The ¹H proton can be considered as a charged sphere rotating with a magnetic moment and collinear angular magnetic momentum.(21) Under an external magnetic field (B₀), each proton rotates around its axis with an angular frequency ω_0 , which is proportional to the applied magnetic field strength according to the Larmor equation: $\omega_0 = \gamma B_0$ (γ is the gyromagnetic ratio). This produce a net magnetization in the same direction of B₀ (M), which is described by its components: M_z, parallel to B₀ and called as longitudinal magnetization, and M_{xy}, perpendicular to B₀ and known as transverse magnetization. When radiofrequency (RF) energy is applied in “resonance” with the ω_0 of the protons, the net magnetization can be flipped away from its original axis, a process called excitation.(21, 172) Return to equilibrium results in emission of MR signal proportional to the number of excited protons in the sample. The return of the net magnetization to its original equilibrium state (M_{z(0)}) is known as longitudinal (T₁) relaxation or spin–lattice relaxation (**Figure 4.1**), and consists in the loss of the energy from the excited state (spin) to it surrounding tissue (lattice). The recovery of net longitudinal magnetization is governed by:(172)

$$M_{z(t)} = M_{z(0)} \left(1 - e^{-t/T_1} \right) \quad (4.1)$$

Where T_1 , called longitudinal relaxation time, is defined as the time required for protons to return to 63% of their longitudinal magnetization, and its reciprocal ($1/T_1$) is known as T_1 relaxation rate.(172) Protons from different localizations in biological samples, such as mobile water, tissue-bound water, have different T_1 relaxation rates.(172) Therefore, when a T_1 -weighted MRI image is acquired, tissues containing different types of protons produce images of different signal intensity, and consequently, with different contrast.

The loss of the magnetization in the xy plane is known as T_2 relaxation, or transverse relaxation, and it is an exponential decay due to the spin-spin interactions of precessing nuclei resulting in the loss of phase coherence. In this case, upon excitation of protons by an RF pulse, the 90° RF pulse produces phase coherence of the individual protons and generates the maximum M_{xy} .(172) As the recovery in longitudinal magnetization takes place, the transverse magnetization begins to decrease (T_2 relaxation), called decay (**Figure 4.1**). T_2 relaxation time is defined as the time it takes for the transverse magnetization to decay to 37% of its original value:

$$M_{xy(t)} = M_{xy(0)} e^{-t/T_2} \quad (4.2)$$

In general, T_2 relaxation is faster than that of T_1 . Samples in which protons have a higher degree of translational and rotational freedoms, for example mobile waters compared to tissue bound waters, generally have longer T_2 values, which allows to link T_2 with specific properties of the tissue and it is also very useful in medicine.(172)

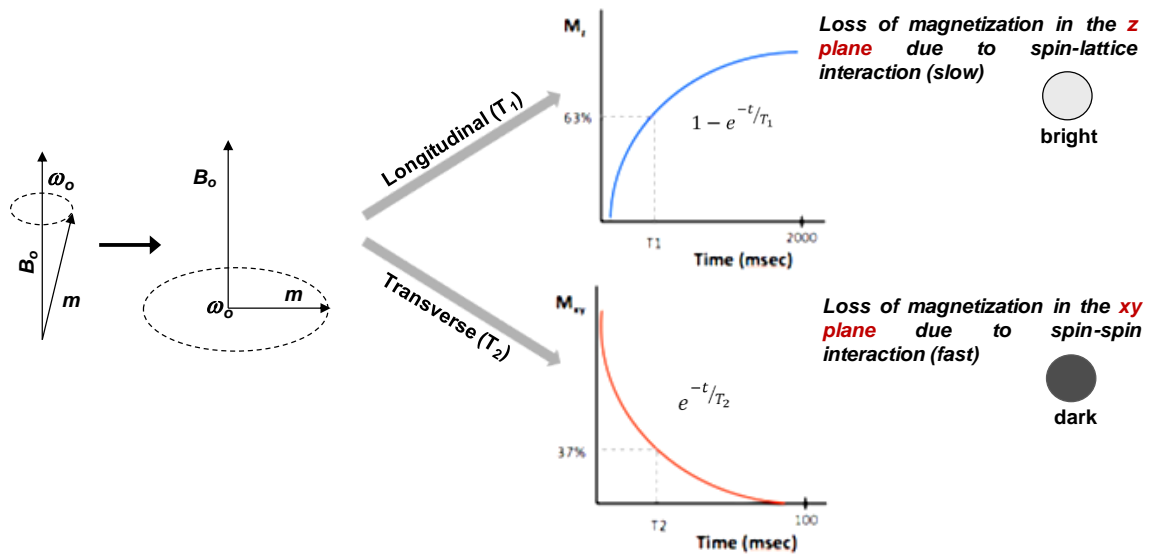


Figure 4.1 - Schematic showing the main differences between T₁ and T₂ relaxation.
Source: Adapted from KHEMTONG et al.(172)

For many MRI applications, a substance is required to induce additional contrast in regions of interest and produce more precise diagnosis, called contrast agents. They are paramagnetic, superparamagnetic, and ferromagnetic compounds that catalytically shorten the relaxation time of water protons.(173) These agents shorten both T₁ and T₂, but they are usually classified as T₁ or T₂ contrast agent based on whether the substance increases in a greater extent the longitudinal or transverse relaxation, respectively. Therefore, T₂-weighted contrast agents locally modify the spin-spin relaxation process of water protons, producing negative or dark images. T₂ contrast agents are based on materials such as superparamagnetic Fe₃O₄, MnFe₂O₃, FeCo, and FePt nanoparticles. T₁-weighted contrast agents affect nearby protons through spin-lattice relaxation, producing positive or bright image contrast. They are based on paramagnetic materials such as Gd(III) and Mn(II).(23) The ability of a contrast agent to change the longitudinal ($1/T_1$) or transverse ($1/T_2$) relaxation rate is represented as r_1 or r_2 , respectively.(173) Relaxivity is defined as the change in relaxation rate after the introduction of the contrast agent normalized to the concentration of the contrast agent [M]:(173)

$$r_1 = \frac{\Delta(1/T_1)}{[M]} \quad (4.3)$$

$$r_2 = \frac{\Delta(1/T_2)}{[M]} \quad (4.4)$$

In T_1 agents, a chemical exchange between bound and free water molecules is required for relaxation process, while T_2 contrast produce much stronger magnetic susceptibility, affecting a large number of water molecules.(172) Despite their utility, T_2 contrast agents have several disadvantages that limit their use in clinical applications. They cause a reduction in the MRI signal (dark images), which can be confused with other pathogenic conditions (such as blood clots and endogenous iron). In the case of tumor imaging, they can also induce magnetic field perturbations on the protons in neighboring normal tissues, which can make spatially well-resolved diagnosis difficult.(24) In contrast, T_1 contrast agents increase the specificity and sensitivity of the MR image by producing bright images. Among the paramagnetic materials useful for T_1 contrast MR imaging, Gd(III) is the most effective contrast agent currently available for clinical use.

4.1.2 Gd(III) based contrast agents

The overwhelming majority of contrast enhanced MRI clinical exams are performed with Gadolinium complexes.(173) Gd(III) possesses seven unpaired electrons, and the spin of which perturbs the proton relaxation in water results in an efficient shortening of longitudinal relaxation time and increases the magnetic signal intensity.(174) However, aqueous gadolinium ions present high toxicity in its free state, and chelation by a co-ligand is required.(175) Gd(III)-diethylenetriamine pentaacetic acid (DTPA) (Magnevist®) is among the most popular clinical agent. It has been used to enhance tissue pathology, detect leaks in the blood-brain barriers (BBB), and in some cases identify physiological changes in tissue.(176) **Table 4.1** shows the r_1 relaxivity for six clinically used Gd(III) chelates at 0.41 T and 1.41 T.

Table 4.1 - T_1 relaxivity for clinically used contrast agents at 0.47 and 1.41 T.

Complex	r_1 (mM ⁻¹ s ⁻¹) $B_0 = 0.47$ T	r_1 (mM ⁻¹ s ⁻¹) $B_0 = 1.41$ T
Gd-DTPA (Magnevist®)	3.8	3.4
Gd-DOTA (Dotarem®)	3.5	3.1
Gd-DTPA-BMA (Omniscan®)	3.8	3.6
Gd-HP-DO3A (ProHamce®)	3.6	3.2
Gd-BOPTA (MultiHance®)	4.8	4.1
Gd-DO3A-butrol (Gadovist®)	3.7	3.2

Source: Adapted from LAURENT et al.(177)

Recently several studies have raised serious concerns regarding the safety of Gd(III) chelates.(178-180) For example, nephrogenic system fibrosis (NSF), a progressive and potentially fatal condition, is associated with gadolinium chelates and occurs mainly in patients with decreased renal function.(178,180) These side effects are aggravated due the low relaxivity of Gd(III) chelates, which makes them effective only at high concentrations (>0.1 mM),(173) as well as their instability and the release of small amount of free Gd(III) ions.(174) Furthermore, they are based on small molecules and present some additional disadvantages such as short blood circulation time and rapid extravasation from the vascular space,(181) limiting their applications, especially for cancer imaging. To overcome these challenges, recent efforts have been focus in increasing the sensitivity and safety of Gd(III)-based contrast agents for MRI. High relaxivity contrast agents can be used at lower doses, or can be used in molecular imaging to detect low concentration targets.(182)

4.1.3 Nanostructured T_1 MRI contrast agents

Nanomaterials provide excellent platforms for the development of MRI contrast agents.(183) Many nanostructured agents have been developed by loading Gd(III) chelates into polymeric nanoparticles,(184) dendrimers,(185) micelles,(186) liposomes,(175) and mesoporous silica nanoparticles.(187) Moreover, Gd-chelates have been conjugated on the surface of gold nanospheres (188-189) or even with gold nanoparticles.(190) The incorporation of Gd(III) onto or into nanoparticles enhance their sensitivity by increasing the concentration of Gd(III) per nanocarrier, prolonging imaging time, and reducing their toxicity.(22, 28-32) Moreover, these systems usually present higher relaxivity compared to free Gd(III)-chelates due both an additive effect of all Gd(III) centers, and the slow global rotational motion that enhances the r_1 .(191) An overview of different types of nanostructured T_1 MRI contrast agents and their respective relaxivity r_1 are shown in **Table 4.2**.

Many are the factors that influence the relaxivity of nanostructured T_1 agents. As can be seen from **Table 4.2**, size and shape play a significant role in the r_1 relaxivity. The position of the Gd(III) chelate also influences the relaxivity. For example, if the chelates are on the surface of the particle, it will be more exposed to the bulk water molecules which eventually results in an enhanced T_1 relaxation effect.(192) Another important factor is the applied magnetic field. Higher magnetic fields, such as 4.7 T, are relevant because they provide not

only a greater signal to noise ratio, but also a higher spatial resolution and reduced acquisition times.(182) Many MRI scanners with higher fields, such as 3, 4.7 or even 9.4 T, have been used clinically. However, T_1 relaxivity of Gd(III) compounds typically decreases as the magnetic field increases.(182, 193) Caravan et al. performed a detailed study to understand the dependence of r_1 and r_2 relaxivity as a function of magnetic field using both experimental and theory.(182) They show that the effect of the magnetic field in the relaxivity is more pronounced for slow tumbling molecules than for fast tumbling molecules. For example, small molecules like Gd-DTPA show a modest decrease in r_1 with field, however, for Gd(III) chelates bound to serum albumin, the relaxivity decrease from $24.3 \text{ mM}^{-1} \text{ s}^{-1}$ at 1.4 T to $11.2 \text{ mM}^{-1} \text{ s}^{-1}$ at 4.7 T.

Compared to traditional small molecular-based contrast agents or therapeutic drugs, these new nanomedicine platforms permit a highly integrated design that can incorporate multiple functions such as imaging, targeting, and therapeutic in one system.(172) These modular systems with theranostic functions have been proved to be essential for overcoming the challenge of tumor heterogeneity and achieving personalized medicine. Moreover, the precise localization of nanomaterials in the body is one important step to evaluate the efficiency and safety of these new therapeutic agents.(115) In this context, Gd(III)-chelates conjugated with near infrared (NIR) photothermal transducers have attracted much attention. Coughlin et al conjugated Gd(III) chelates on the surface of gold nanoshells.(194) The system presented a MRI contrast enhancement efficacy ($37 \text{ mM}^{-1} \text{ s}^{-1}$ at 1.41 T, 37°C) and higher signal intensity *in vivo* after an intratumoral injection in a subcutaneous melanoma tumor. This enhancement was attributed to the high payload of Gd(III) ions and the restricted molecular tumbling of the Gd(III)-chelates when conjugated with the nanoshells. Rotz et al conjugated Gd(III)-chelates to a DNA-functionalized gold nanostars with good high relaxivity of r_1 of $54.7 \text{ mM}^{-1} \text{ s}^{-1}$ at 1.41 T and $9.4 \text{ mM}^{-1} \text{ s}^{-1}$ at 7 T.(195) Besides the high payload of Gd(III) ions and the restricted molecular tumbling of the Gd(III)-chelates, the authors attributed the enhancement of the relaxivity to the surface curvature on the nanostar surface. According to them, the shape affect the organization of conjugated DNAs on the particle surface and, consequently, the sequestration of water molecules in the proximity of the Gd(III) complexes.(195) However, these systems can face many limitations for medical applications. First of all, in the nanoshells case, the size of the particles can difficult their accumulation after an intravenous injection for treatment of other kinds of tumor. Moreover, negatively or positively charged nanomaterials can led to a rapid formation of protein corona when in presence of biological fluids,(196) which can change their pharmacokinetics and

physico-chemical properties. Finally, the fact that the Gd(III) chelates are in the surface of the nanomaterial can lead to the same safety concerns related to the small molecules Gd(III) agents.

Table 4.2 - T_1 relaxivity of Gd(III) conjugated nanomaterials.

Complex	r_1 ($\text{mM}^{-1} \text{s}^{-1}$)	Reference
Gd(III)-conjugated gold nanoparticles (5 nm)	50.0 (1.41 T) 11 (4.7 T)	(190)
Gd(III)-conjugated gold nanoshells	37.0 (1.41 T)	(31)
Gd(III)-conjugated gold nanostar	54.7 (1.41 T) 9.4 (7.0 T)	(32)
Gold nanoparticles@DNA-Gd(III) 30 nm	20.0 (1.41 T)	(188)
Gold nanoparticles@DNA-Gd(III) 13 nm	16.9 (1.41 T)	
DNA-Gd(III)	8.7 (1.41 T)	
Gd(III)-loaded dendrimer	26.0 (2.0 T)	(197)
Core-encapsulated Gd(III) Liposomes	3.8 (1.5 T)	(192)
Surface-conjugated Gd(III) Liposomes	7.9 (1.5 T)	
Gd(III) DOTA-DSPE-based Liposomal	11.8 (1.41 T)	(198)
Gd ₂ O ₃ -D-glucuronic acid	9.9 (1.5 T)	(199)

Source: By the author.

4.2 EXPERIMENTAL SECTION

4.2.1 Materials

Tetraethoxysilane (TEOS) and 3-aminopropyltriethoxysilane (APTES) were purchased from Gelest, S-2(4-isothiocyanatobenzyl)-1,4,7,10-tetraazacyclododecane-1,4,7,10-tetraacetic acid (Gd-DOTA-SCN) was purchased from Macrocyclics, tetrakis(hydroxymethyl) phosphonium chloride (THPC), $\text{Gd}(\text{NO}_3)_3 \cdot 6\text{H}_2\text{O}$, and chloroauric acid ($\text{HAuCl}_4 \cdot 3\text{H}_2\text{O}$) were purchased from Sigma Aldrich; anhydrous potassium carbonate (K_2CO_3) from Fisher, mPEG-Thiol (MW = 10000) and Thiol-PEG- NH_2 (MW = 10000) from Laysan Bio, Inc.; NaOH from Fisher and employed without further purification. 50 nm Gold Colloid citrate NanoXact was purchased from NanoComposix. Dulbecco's Modified Essential Media (DMEM) was purchased from ATCC, fetal bovine serum (FBS), Phosphate Buffer Saline (PBS), Antibiotic-Antimycotic Solution from CellGro and RAW 264.7 macrophage cells were purchased from Sigma-Aldrich. 200 proof ethanol was purchased from KOPTEC. SYTOX® Red dead cell stain was purchased from Invitrogen. Aqua regia was used to clean all glassware and stirring bars, followed by thorough rinsing with distilled water, ethanol and Milli-Q water in the last step. Milli-Q water (18.2 M Ω .cm at 25 °C, Millipore) was used to prepare all solutions.

4.2.3 Gd-embedded Au nanomatryoshkas (Gd-NM) synthesis

The synthesis of Gd-NM developed in this study was adapted from the previously reported synthesis of fluorescent dye encapsulated NM by Ayala-Orozco et al.(200) The 50 nm Au nanoparticles were initially coated with an amorphous SiO_2 layer by the condensation of tetraethyl orthosilicate in an alkaline medium. Briefly, 21 mL of 50 nm Au colloid solution (0.05 mg/mL) was mixed with 180 mL of 200 proof fresh ethanol under magnetic stirring and subsequently, 1.8 mL of ammonium hydroxide were quickly added followed by 36 μL 10% TEOS solution in ethanol and 21 μL of 10% APTES solution in ethanol. The reaction vessel was sealed and allowed to proceed for 75 min at room temperature under vigorous stirring and then stored in the refrigerator under gentle stirring at 4 °C. After 165 min (total reaction time), a mixture previously prepared containing a Gd(III) chelate was added. The mixture contains: 15 μL of Milli-Q H_2O , 5.5 mg of Gd(III)-DOTA-SCN, 125 μL of ethanol, and 8 μL of a 20%

APTES ethanolic solution. This mixture was kept for at least 1 h under gentle stirring at room temperature and protected from light. After the addition of Gd(III) chelate mixture to the nanoparticle suspension, the system was maintained under gentle stirring at 4 °C for a total reaction time of 27 h. The Gd(III) ions were incorporated into the APTES-doped silica layer of the NM by using a covalent strategy. More specifically, the SCN groups of the chelate Gadolinium(III) S-2 (4-isothiocyanatobenzyl)-1,4,7,10-tetraazacyclododecane-1,4,7,10-tetraaceticacid), was bound to the amine groups of the APTES.

In the following day, the Au/SiO₂ nanoparticles were transferred into a pre-washed (200 proof ethanol) dialysis membrane (Spectra/Por 6, MWCO = 10000, Spectrum Labs) and dialyzed in 1 gallon of 200 proof ethanol for 16 h at room temperature to remove the remaining free reagents. The cleaned nanoparticle suspension was cooled to 4°C for at least 2 h and then centrifuged 35 min at 1700 g. The supernatant was removed and the pellets were dispersed in 3 mL of 11 mg/mL Gd(NO₃)₃ aqueous fresh solution. The system was then sonicated for 10 min, kept at room temperature for 100 min, and sonicated again for 10 min. The suspension was centrifuged at 1800 g for 25 min and the pellet was dispersed in 2 mL of water, and then centrifuged one more time at 1500 g for 25 min. The cleaned pellet was dispersed in 1 mL of water and sonicated for 5 min. Gd(NO₃)₃ was added to reload the Gd(III) ions onto the chelate, since the extremely basic conditions, such as high ammonia concentrations, and multiple rinsing steps can remove some ions from the chelates.

The Au/SiO₂/Au nanoparticles were prepared by decorating the silica coated nanoparticles with small gold colloid (2-3 nm) fabricated by the method reported by Duff et al.(73) Briefly, 1 mL of the Gd(III) doped silica coated gold nanoparticle suspension was mixed with 600 µL of 1 M NaCl and 40 mL of Duff gold colloid (1-2 nm). The precursor particles were left unperturbed for 24 h at room temperature, followed by sonication and centrifugation (950 g, 30 min) to remove the excess of Duff gold colloid. The pellet was dispersed in 2 mL of Milli-Q water and centrifuged two more times at 800 g for 20 min. The final precipitate was dispersed in 500 µL of Milli-Q H₂O and was called the seeded precursor. The formation of a continuous metallic shell around the seeded precursor was performed by mixing 3 mL of plating solution (1% HAuCl₄- K₂CO₃ solution previously prepared) with 20-40 µL of the seeded precursor and 15 µL of formaldehyde, under a fast shaking for 1 min. The color of the solution changed from reddish to purple upon the formation of the gold outer shell.

4.2.4 Polyethylene glycol (PEG)-functionalization of Gd-NM (Gd-NM-PEG)

To provide chemical stability, the Gd-NM were functionalized with a thiolated mPEG layer as follows: 3 mL of $\sim 3 \times 10^{10}$ particles/mL aqueous nanoparticles were mixed with a freshly prepared mPEG-Thiol (MW = 10,000, Laysan Bio, Inc) aqueous solution under sonication to a final solution concentration of 100 $\mu\text{mol/L}$. The system was sonicated for 30 min and then kept under gentle stirring and protected from light for 12 h. The system was then centrifuged at 700 g for 20 min and re-suspended in 500 μL of Milli-Q water. For the *in vitro* studies, after conjugation with mPEG-Thiol solution, the mPEG coated Gd-NM solution was diluted in 1 mmol L^{-1} phosphate buffer pH = 7.4, sterilized by filtration through a 0.22 μm filter (Whatman) and then concentrated via centrifugation (700 g, 20 min) to the final concentration of $\sim 10^{11}$ particles/mL.

4.2.5 GdPEG-coated gold nanomatryoskas (GdPEG-coated NM) synthesis

Bare gold nanomatryoskas were also synthesized and then functionalized externally with Gd(III) chelate for comparasion. Initially, bare NM were synthesized. Briefly, 21 mL of 0.05 mg/mL 50 nm Au colloid were mixed with 180 mL of 200 proof ethanol, 1.8 mL of 28-30% ammonium hydroxide, 36 μL 10% TEOS solution in ethanol, and 36 μL of 10% APTES in ethanol. The reaction was allowed to proceed for 65 min at room temperature under vigorous stirring and then stored in the refrigerator at 4 °C for 22 h. The following day, the Au/SiO₂ nanoparticle suspension was dialyzed in 200 proof ethanol for 16 h at room temperature. The nanoparticle suspension was cooled to 4°C, centrifuged at 1500 rcf for 35 min and re-dispersed by sonication in a total volume of about 3 mL of ethanol. The precursor Au silica nanoparticles were coated with small gold colloid (2-3 nm) by mixing 3 mL of Au/SiO₂ nanoparticles with 40 mL of Duff Au colloids, and 600 μL of 1 M NaCl solution. The mixture was sonicated for 20 min and incubated for 24 h at room temperature following which they were sonicated for 15 min and centrifuged at 900 g for 25 min. The pellet was dispersed in 2 mL of Milli-Q water and centrifuged two more times at 800 g for 20 min, the supernatant removed and the final pellet was dispersed in 500 μL H₂O. A continuous gold shell was grown around the Au/SiO₂ nanoparticles following the same procedure of Gd-NM.

The as-prepared NMs were centrifuged at 700 g for 20 min and dispersed in 3 mL of H₂O. The system was sonicated for 10 min and then a solution containing Thiol-PEG-NH₂ was added to a final concentration of 100 $\mu\text{mol L}^{-1}$. After 30 min of sonication and overnight

incubation at 4°C, the system was centrifuged at 700 g for 20 min and resuspended in 3 mL of Milli-Q water. In the next step, the NH₂-PEG-NM was incubated with 300 µL, of 0.01 mg/mL Gd-DOTA-SCN aqueous solution and 20 µL 1 N NaOH solution. The mixture was sonicated for 30 min and incubated overnight at room temperature under gentle stirring. The Gd(III) chelates bind covalently to the NH₂ group of the PEG molecules. The excess of Gd(III) chelate and PEG molecules were removed by centrifugation twice at 700 g for 20 min followed by dispersal with Milli-Q to a final concentration of $\sim 10^{11}$ particles/mL.

4.2.6 Calculation of Nanomaterial Concentration

The concentration of the nanomaterials was determined by the following equation derived from Beer's law: (10)

$$\frac{\# \text{ nanomaterials}}{\text{mL}} = \frac{2.303 \times A}{\epsilon \times l} \quad (4.5)$$

where A = experimental extinction at the peak plasmon resonance

ϵ = theoretical extinction cross section taken from Mie theory

l = path length of the cuvette (1 cm)

The calculation of the extinction cross section by Mie theory was discussed in Chapter 2. The constant parameters used in the calculation were: dielectric constant of the SiO₂ of 3.0, dielectric constant of the medium (H₂O, 1.77), dielectric constant of gold, and theoretical extinction efficiency of $Q\epsilon = 5.53$. The calculated value of the extinction cross section for the typical Gd-NM used in this study with dimensions of $[r_1, r_2, r_3] = [25, 38, 53]$ nm was $\epsilon = 6.89 \times 10^{-10} \text{ cm}^2$. This value was substituted in **Equation 4.5** and the concentration of particles was calculated based on the experimental extinction (A) measured in a Cary 5000 UV-VIS-NIR Varian spectrophotometer.

4.2.7 Characterization

The size and morphology of both Gd-NM and GdPEG-coated NM in each step of the synthesis were evaluated by transmission electron microscopy (TEM) using a JEOL 1230 operating at 80 kV. For this, one drop of the diluted samples were deposited on a carbon film

copper grid 200 mesh (Ted Pella, Inc.) and dried at room temperature. For a further detailed investigation, the particles were also imaged in a high resolution JEOL 2010 TEM operating at 200 kV.

Fourier transform infrared spectroscopy (FTIR) was used to investigate the interactions between the Gd-DOTA-SCN and the amine groups from the APTES-doped silica layer. For this, FTIR spectra of Gd-DOTA-SCN solution, silica-coated Au colloids and Gd(III)-embedded silica-coated Au colloids deposited on silicon substrates were obtained with a resolution of 4 cm^{-1} in absorbance mode using a Vertex 80v FTIR Spectrometer (Bruker).

The investigation of the optical properties was performed by ultraviolet-visible-near infrared (UV-VIS-NIR) spectroscopy using a Cary 5000, Varian spectrometer. Dynamic light scattering (DLS) was used to measure the *in situ* hydrodynamic size distribution of the nanostructures in suspension in each step of the synthesis process. The analyses were always performed in triplicate at room temperature using a Malvern Nano-ZS spectrometer (Malvern Instruments, UK). The surface change around the particles due the functionalization was evaluated by zeta potential. The measurements were performed in triplicate at room temperature using a Malvern Nano-ZS spectrometer (Malvern Instruments, UK).

4.2.8 Inductively Coupled Plasma Mass Spectroscopy (ICP-MS)

The concentration of Gd(III) in the particles were determined by ICP-MS, which is able to detect metals in a sample at concentrations as low as 1 ppm. The technique consists in two primary components: the inductively coupled plasma (ICP) and the mass analyser (MS). The samples are digested in acid solution and introduced into ICP using a nebulizer. The ICP is an electrically conductive Argon gas at very high temperatures ($\sim 10000\text{ K}$) which evaporates the solvent and atomizes and ionizes the sample before it is analyzed in the MS. The MS used was a quadrupole mass spectrometer that consists of two parts of electrically conductive rods connected in series. The charged samples travel through the quadrupole at a rate that is determined by the mass to charge (m/z) ratio of the ionized atoms. Only the selected m/z ratio will reach ion detector with all other ions colliding with the quadrupole rods allowing sensitive and selective detection. The measurements were performed in a Perkin Elmer Nexion 300. First, the Gd-NM or GdPEG-coated NM samples were mixed with concentrated aqua regia ($\text{HNO}_3\text{:HCl } 1\text{:}3$) solution overnight. The resulting solution was

diluted by 500 times with a solution consisting of 1% v/v aqua regia, and 2% v/v HNO₃ solution was used for ICP-MS analysis. The Gd(III) concentration was determined using a calibration curve made with Gadolinium ICP/DCP standard solution (Fluka).

4.2.9 Gd(III) release

The release of Gd(III) from both Gd-NM-PEG and GdPEG-coated NM was investigated. For this, the concentration of Gd(III) in each system was determined by ICP-MS. Then, the particles were dispersed in PBS buffer and serum media (10% FBS) and kept at 37°C for 48 h. After that, the particles were centrifuged at 1000 g for 15 min, and the concentrations of Gd(III) in both the supernatant and the pellet were determined by ICP-MS.

4.2.10 MRI Analysis

The MRI relaxation measurements were performed on a 4.7 T Biospec spectrometer (Bruker Biospin MRI, Billerica, MA) with a 30 cm bore horizontal imaging system, using imaging gradients with an inner diameter of 60 mm and a volume resonator with 35 mm inner diameter. Dilutions of the particle solution were sealed in 200 µL PCR tubes and placed in a holder. Spin-lattice (T₁) relaxation times were measured using a RARE (Rapid Acquisition Relaxation Enhanced) variable TR sequence (TE = 10.5 ms; with 10 TRs from 15000 to 400 ms). Spin-spin (T₂) relaxation times were measured using a multi-echo sequence (TE_{min} = 10 ms, with 10 ms echo spacing over 30 echoes; TR = 5000 ms). All images were acquired with matching slice geometry (1 mm axial sections, 32 mm x 32 mm field-of-view over a 256 x 256 image matrix). Relaxation time constants for each sample were measured by fitting signal decay curves to a standard model in ParaVision 5, the operating software for the Biospec platform.

4.2.11 Cytotoxicity

The RAW 264.7 macrophage cells (Sigma-Aldrich) were cultured in Dulbecco's Modified Essential Media (DMEM, ATCC) supplemented with 10% fetal bovine serum (FBS, CellGro) and 1% Antibiotic-Antimycotic Solution (CellGro) and maintained at 37°C with 5% CO₂. This type of cell has been included in nanomaterial toxicity investigations as an

inflammatory cell type.(201) Cells were initially seeded in 6-well plates at a density of 5×10^5 cells/well and incubated for 24 h prior the introduction of Gd-NM-PEG and GdPEG-coated-NM. The particles were added to the serum containing media in a NM:Cell ratio of 3000:1 and 10000:1. After 20 h of incubation with NMs, the media was removed. Cells were rinsed with PBS solution and detached from the plate using a sterile cell scraper and washed by centrifugation twice in buffer to remove the excess of media. The cells from each individual well were dispersed in a final volume of 500 μ L of PBS, stained with SYTOX® Red dead cell stain, and analyzed by flow cytometry using an Ex: 635 nm laser. The measurements were performed on an LSRFortessa X20 cell analyzer (BD Biosciences).

4.2.12 Fluorescence Imaging

Differential interference contrast (DIC) and confocal images were taken to investigate the Gd-NM-PEG cellular internalization. Briefly, the cells were cultured for 24 h in a μ -Slide 8 well (Ibidi) and, then incubated with the particles. After 20 h, the cells were rinsed three times with PBS and fixed with a 4% paraformaldehyde solution. The cells were washed twice with PBS and incubated with a Hoechst 33342 solution to stain the cell nucleus. After an incubation of 10 min protected from light, the cells were rinsed twice with PBS. All images were collected on a Nikon A1-Rsi Confocal microscope and the particles were imaged in the reflection mode (Excitation and Emission at 640 nm).

4.2.13 Preparations of Cells for MRI

RAW 267.4 macrophages cells $\sim 5 \times 10^5$ cells/well were seeded in a 6 well plate for 24 h, then the media was removed and the cells were incubated with media containing Gd-NM-PEG for 20 hours. The cells were rinsed in PBS three times to remove the excess of non-internalized nanoparticles, detached from plate using a cell scraper and centrifuged. The cells were dispersed in a final volume of 200 μ L PBS with a final concentration of $\sim 5.2 \times 10^7$ cells/mL. The T_1 -weighted MR images of the cells were obtained at 4.7 T and 25°C.

4.2.14 Phantom preparation for MRI

Phantoms of 1% agarose gel were prepared in 200 μL centrifuge tubes. Briefly, the agarose gel was heated until the complete solubilization, and the Gd-NM-PEG was subsequently transferred to the warm agarose and allowed to cool in ambient conditions to form the gel, ensuring that no air bubbles were formed during cooling. The final Gd(III) concentrations were: 0.6, 2.5, 5, 10, and 20 μM , correspondent to a 0.14, 0.6, 1.14, 2.3, and 4.6×10^9 in number of Gd-NM-PEG. The final volume was 100 μL for all concentrations. The T_1 -weighted MR images of the phantoms were obtained at 4.7 T and 25°C.

4.3 RESULTS AND DISCUSSION

Gd-NM nanoparticles were fabricated as shown in **Figure 4.2A**. Transmission electron microscope images corresponding to each stage of the synthesis are shown in **Figure 4.2Bi-iv**. Au nanoparticles of radius 50 ± 4 nm (**Figure 4.2Bi**) were initially coated with a ~ 21 nm amorphous silica layer doped with Gd(III) chelates (**Figure 4.2Bii**). The isothiocyanate ($\text{N}=\text{C}=\text{S}$) group of the Gd-DOTA-SCN chelate is believed to bind covalently to the NH_2 group of the APTES molecules within the silica network. This results in the formation of a thiourea ($\text{NH}-(\text{C}=\text{S})-\text{NH}$) bond that was monitored by FTIR measurements (**Figure 4.3**). As a result of the formation of this bond, the peak at 2100 cm^{-1} (attributed to the $\text{N}=\text{C}=\text{S}$ vibration in the Gd(III) chelate molecules) disappears and the peak at 1100 cm^{-1} (attributed to the $\text{C}=\text{S}$ bound in the thiourea) appears after incorporation of the chelate into the silica layer.(202)

In the next step, Gd-DOTA-SCN-doped APTES silica-coated Au colloid were incubated with $\text{Gd}(\text{NO}_3)_3$ to reload the Gd(III) ions, since the extremely conditions, such as high ammonia concentrations during the silica growth, can take out some ions from the chelates. The Gd(III) loaded within the SiO_2 layer before and after incubation with $\text{Gd}(\text{NO}_3)_3$ was examined by high resolution TEM (**Figure 4.4**). The TEM images reveal that the $\text{Gd}(\text{NO}_3)_3$ etches the silica layer and promotes some darkening of the contrast as well, which is probably due the incorporation of many Gd(III) ions. The $\text{Gd}(\text{NO}_3)_3$ solution may also affect the porosity and accumulation of H_2O molecules in the silica layer.

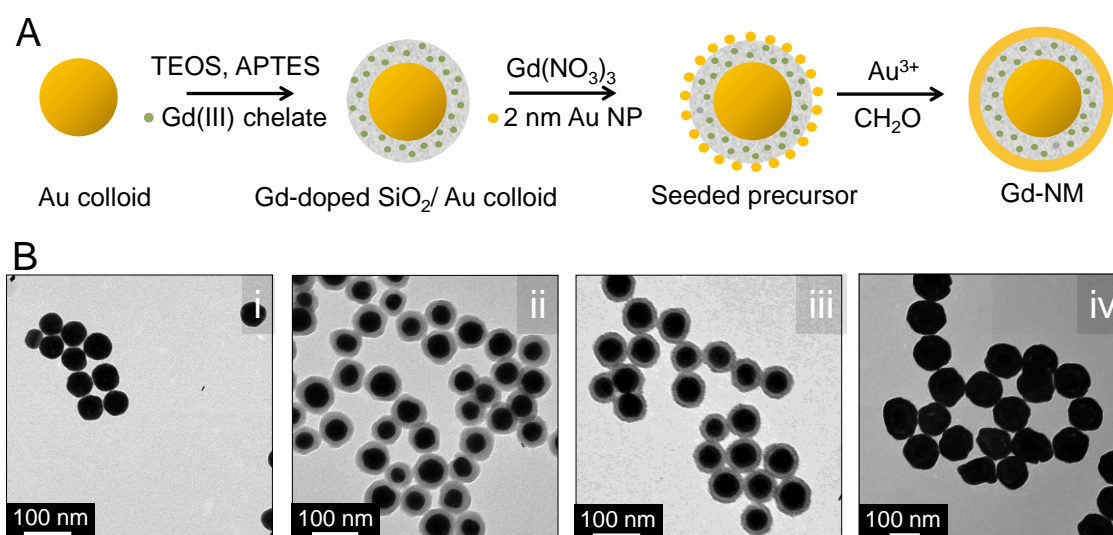


Figure 4.2 - (A) Schematic representation of the MRI active nanomatrix synthesis showing the stepwise synthesis process: the 50 nm diameter gold colloids are coated with Gd(III) chelates embedded in a SiO₂ shell and then a continuous Au shell. (B) TEM images corresponding to each step in the process; scale bars are 100 nm.

Source: By the author.

After growth of the Gd(III)-embedded silica layer, 2-3 nm diameter Au colloidal nanoparticles were attached to the outer surface of the silica layer. At this stage we refer to the nanoparticles as the “seeded precursor”. The ultrasmall Au nanoparticles serve as nucleation sites for the electroless plating of the outer Au shell layer (**Figure 4.2Biii**). This results in Gd-NMs with average dimensions of $[r_1, r_2, r_3] = [25, 38, 53]$ nm (**Figure 4.2Biv**). From the TEM image, we can see that this multistep synthesis produces stable, monodisperse Gd-NM with a continuous outer Au layer. The final Au shell also allows direct conjugation of polymers and biomolecules to the nanoparticle surface.

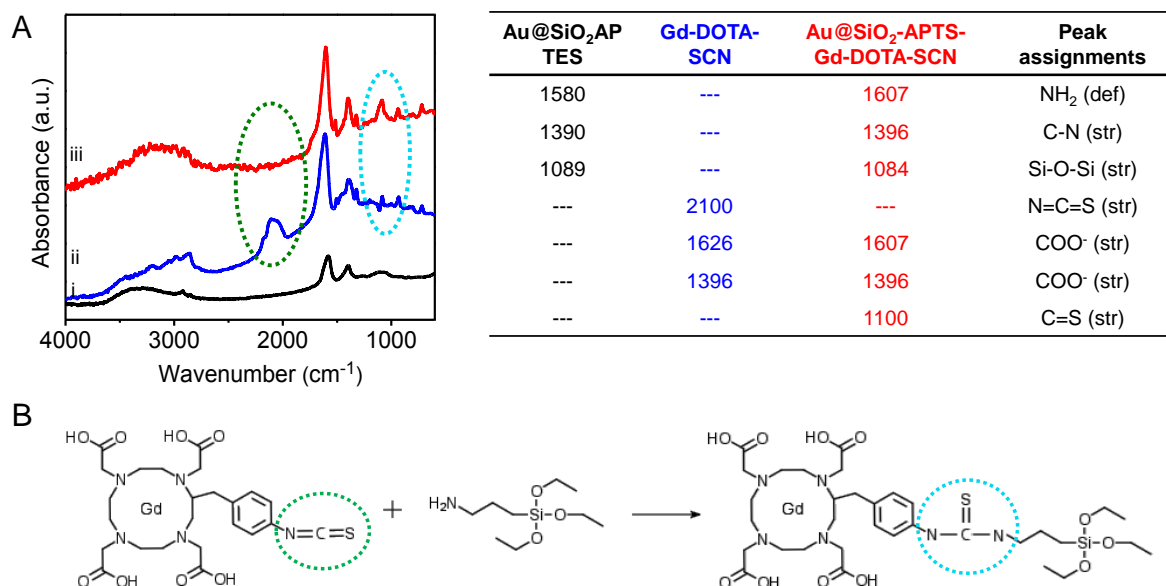


Figure 4.3 - (A) FTIR spectra of (i) Au@SiO₂-APTES, (ii) Gd-DOTA-SCN, and (iii) Gd-doped SiO₂-coated Au colloid. The disappearance of the 2100 cm⁻¹ peak, attributed to the N=C=S vibration, is an indicative of the bond between Gd-DOTA-SCN and the amine groups from APTES (B) the chemical reaction showing the bond formation. The table shows the FTIR peak assessments corresponding to each spectrum.

Source: By the author.

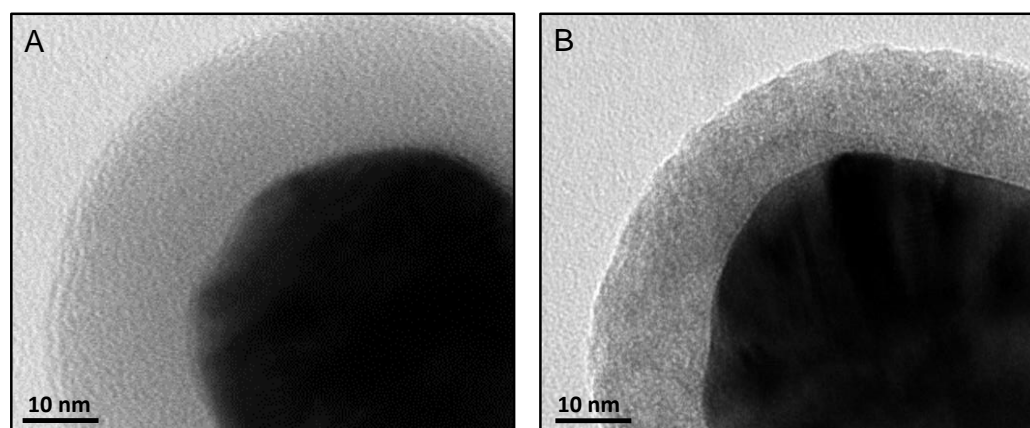


Figure 4.4 - High resolution TEM images of: (A) SiO₂-coated Au colloid and (B) Gd-doped SiO₂-coated Au colloid.

Source: By the author.

To optimize the MRI contrast of the Gd-NMs, the concentration of Gd(III) per particle was varied by modifying the Gd chelate concentration and reaction time. The MRI relaxivity as a function of Gd(III) concentration is shown in **Figure 4.5A**. The relaxivities r_1 were

calculated from the $1/T_1$ versus Gd(III) concentration data. The T_1 relaxivity curves for three representative concentrations are shown in **Figure 4.6**. We observed that at low Gd(III) concentrations, the MRI relaxivity r_1 increased with increasing Gd(III) concentration per NM. For example, the relaxivity of 0.7×10^5 Gd(III) ions/NM was $8 \text{ mM}^{-1} \text{ s}^{-1}$ and increased until a maximum of $14.6 \text{ mM}^{-1} \text{ s}^{-1}$ at 2.5×10^5 Gd(III) ions/NM was reached. As the amount of Gd(III) per NM was increased further, to 8.2×10^5 Gd(III)/NM, the relaxivity decreased to $5.3 \text{ mM}^{-1} \text{ s}^{-1}$.

This type of quenching effect has been observed in other nanoparticle-based Gd(III) systems developed for MRI.(175, 203, 204). In these cases, quenching was attributed to the packing of Gd(III) into a limited volume, which could restrict the access of H_2O molecules to the coordination sphere of the Gd(III). However, as we will discuss shortly, our results indicate that, in the case of Gd-NMs, the inner coordination sphere H_2O molecules do not likely play a significant role in the enhanced T_1 relaxivity. It has also been proposed that systems with an excessive payload of Gd(III) may lead to a disproportionate weight of T_2 effects, which might have some negative effects on T_1 weighted images(175, 204-206). We did observe an increase in T_2 relaxivity by increasing the number of Gd(III) per nanoparticle. For example, for a system with 2.3×10^5 Gd(III) per nanoparticle, the r_2 was nominally $54.7 \text{ mM}^{-1} \text{ s}^{-1}$, while for 4.7×10^5 it was $93.6 \text{ mM}^{-1} \text{ s}^{-1}$. This increase in T_2 relaxivity has, in other nanoparticulate systems, been attributed to the geometric confinement of Gd(III) with increased dipolar interaction between neighboring Gd(III)-Gd(III) ions and/or Curie spin relaxation.(207)

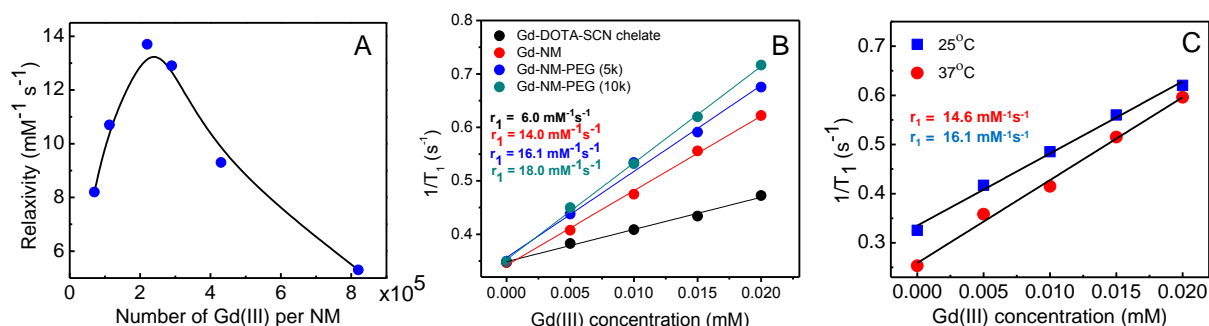


Figure 4.5 - (A) The r_1 relaxivity of Gd-NM as a function of the number of Gd(III) per NM measured at 4.7 T. (B) The r_1 relaxivities of Gd(III)-DOTA (for comparison), Gd(III)-NM, and Gd(III)-NM-PEG; error bars represent standard deviation of three independent experiments at 25°C. (C) Thermal variation of T_1 for Gd-NM-PEG at 25°C (blue, $r_1 = 14.6 \text{ mM}^{-1} \text{ s}^{-1}$) and 37°C (red, $r_1 = 16.1 \text{ mM}^{-1} \text{ s}^{-1}$). The r_1 values were extracted from the slopes.

Source: By the author.

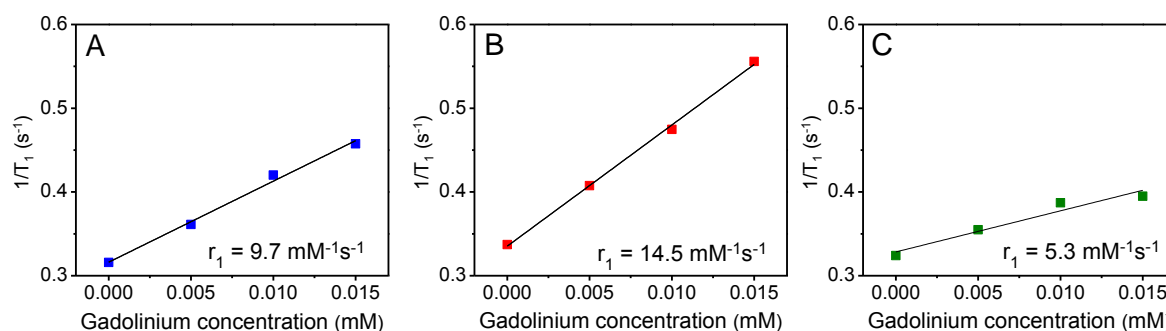


Figure 4.6 - T_1 (longitudinal) rate of Gd-NM for: (A) 0.8×10^5 , (B) 2.7×10^5 , and (C) 8.2×10^5 numbers of Gd(III) ions per particle at 4.7 T and 25°C. The r_1 values were extracted from the slopes.

Source: By the author.

The nanoparticle relaxivity can also be affected by nanoparticle aggregation, which can in turn be influenced and controlled by nanomaterial surface chemistry. To prevent aggregation, the Gd-NMs were functionalized with thiolated PEG molecules of 5,000 and 10,000 MW. PEG functionalization also improves NM dispersion in media, and is known to increase circulation time *in vivo*.(208) The increasing in the hydrodynamic diameter and the reduction of zeta potential to close to zero shown in **Figure 4.7** confirm the coating of the particles. The Gd-NM relaxivity increased significantly with PEG functionalization, from $14.0 \text{ mM}^{-1}\text{s}^{-1}$ to 16.1 and $18.0 \text{ mM}^{-1}\text{s}^{-1}$ for 5 and 10 kDa, respectively (**Figure 4.5B**). We can infer from this increased relaxivity that the presence of PEG molecules on the surface of the nanoparticles facilitates the approach of water protons to the NM surface, closer to the internally encapsulated Gd(III) ions. The diffusion of water in the proximity of the Gd(III) is known to play an important role in the enhancement of proton relaxivity.(195, 209-210) For example, Cho et al evaluated the effect of the surface coating of Gd_2O_3 nanoparticles in the r_1 relaxivity.(211) They showed that the surface modification with poly(acrylic acid) enhanced the r_1 relaxivity, it was attributed to the modulation of water molecules diffusion by the surface coating. Similarly, Sun et al. attributed the longitudinal relaxivity enhancing, among others, to an increase number of outer coordinated water molecules via entrapment by the polysaccharide for the polysaccharide-Gd-DTPA.(212)

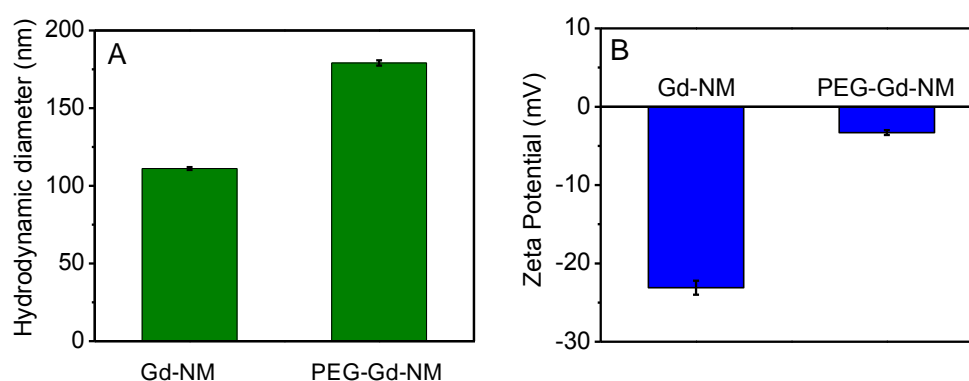


Figure 4.7 - (A) Dynamic Light Scattering and (B) Zeta potential for Gd-NM before and after PEG surface functionalization.

Source: By the author.

Besides Gd(III) concentration and surface functionalization, temperature can also strongly affect the relaxivity, which can have a major impact *in vivo*.⁽²¹³⁾ We compared the relaxivity measurements of Gd-NM-PEG at 37 °C and at room temperature (**Figure 4.5C**). The relaxivity was found to increase from $r_1 = 14.6 \text{ mM}^{-1} \text{ s}^{-1}$ when the ambient temperature of the nanoparticles was increased from room temperature to $r_1 = 16.1 \text{ mM}^{-1} \text{ s}^{-1}$ at physiological temperature. This effect has been reported for other nanostructured gadolinium system, such as liposomal structures.⁽²⁰⁴⁾ However, the opposite is observed for small molecular weight Gd(III)-based compounds, i.e., the relaxivity decreases with increasing the temperature.⁽²¹⁴⁾ This is expected because the rotational correlation time is a limiting parameter parameter for small molecules.⁽²¹⁴⁾

In the following experiments, Gd-NM-PEG was compared to a “control” NM, where Gd(III) was not incorporated inside the nanoparticle but was instead attached to the outside of the NM through conjugation of Gd-DOTA-SCN to aminated PEG linker molecules. **Figure 4.8** shows the schematic representation of the bare NM synthesis and functionalization. The increase in the hydrodynamic size and the positive zeta potential confirm the functionalization of NM with the Thiol-PEG-NH₂ (**Figure 4.9**). After conjugation with Gd-DOTA-SCN, the hydrodynamic diameter had a small decrease, which is probably related to the removal of polymer excess during the several steps of centrifugation. The negative zeta potential confirms the conjugation with the Gd-DOTA-SCN (**Figure 4.9B**). These nanoparticles will be referred as GdPEG-coated-NMs.

Since the presence of biologically active molecules in serum can impact the stability of complex nanostructures,⁽²¹⁵⁾ the amount of Gd(III) released from both types of

nanoparticles was measured after incubation at 37 °C for 48 h in both 10% fetal bovine serum (FBS) and in H₂O by ICP (**Figure 4.10**). For the Gd-NM-PEG system, only 2.7% of Gd(III) was released, while for the GdPEG-coated-NM suspended in H₂O 48.6% of the Gd(III) ions dissociated from the nanocomplex (**Figure 4.10**). In fetal bovine serum, only 5.1% Gd(III) was released from Gd-NM, while 97.5% of the Gd(III) dissociated from the GdPEG-coated-NM. These results clearly indicate that the confinement of Gd(III) between the Au core and the Au shell prevents the release of Gd(III) from the nanoparticle under these conditions.

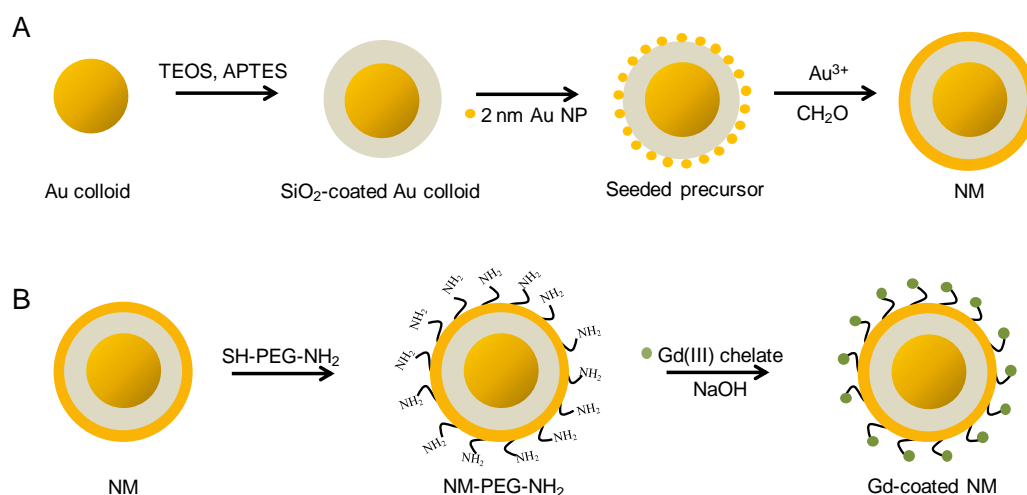


Figure 4.8 - (A) Schematic representation of (A) the regular nanomatryoshkas synthesis and (B) the functionalization of the NM with Gd(III) chelate (GdPEG-coated-NM).

Source: By the author.

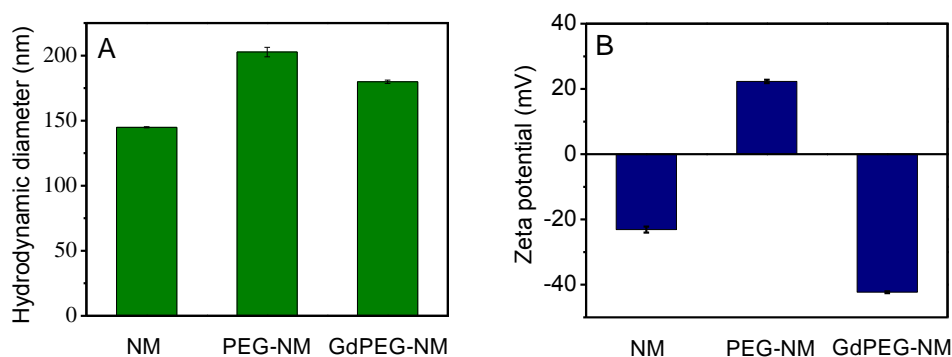


Figure 4.9 - (A) Dynamic Light Scattering and (B) Zeta potential for regular NM before and after conjugation with PEG-NH₂ and Gd chelates (GdPEG-coated-NM).

Source: By the author.

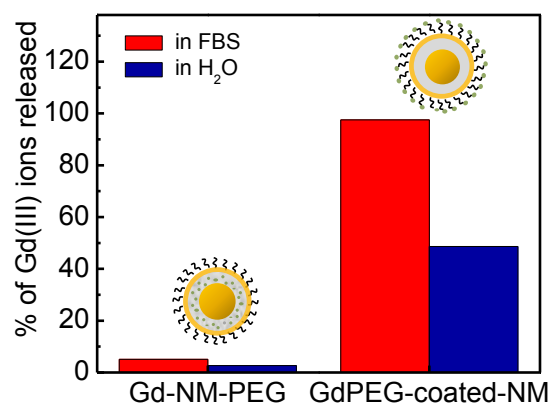


Figure 4.10 - Percentage of Gd(III) ions released from Gd-NM-PEG, where the Gd(III) is located inside the NM which is then functionalized using PEG, versus GdPEG-coated NM, where the Gd(III)-DOTA-SCN is attached outside the NM through a thiol-PEG-amine linker, after 48 h of incubation at 37°C in 10% FBS (red) and H₂O (blue). Gd(III) concentration was quantified using ICP-MS.

Source: By the author.

The physiological environment also play an important role in the MRI efficiency of the contrast agent.(213) In this way, the impact the serum dispersion (10% FBS) on the relaxivity and the plasmon resonance of both Gd-NM-PEG and GdPEG-coated-NM (Figure 4.11) were compared. Following 24 hr incubation, little change in either r_1 relaxivity or extinction spectrum for Gd-NM-PEG was observed, while the GdPEG-coated-NM showed changes in both relaxivity and in extinction spectrum (**Figure 4.11**). Since particle aggregation (176) was not observed (**Table 4.3**), the release of the Gd(III) ions (**Figure 4.10**) may be the responsible for inducing the observed changes in the GdPEG-coated NM case. Also, the increasing in the hydrodynamic diameter for GdPEG-coated NM indicate nonspecific protein binding, which is probably due the high surface charge originated from the Gd(III) chelates on the particle surface.

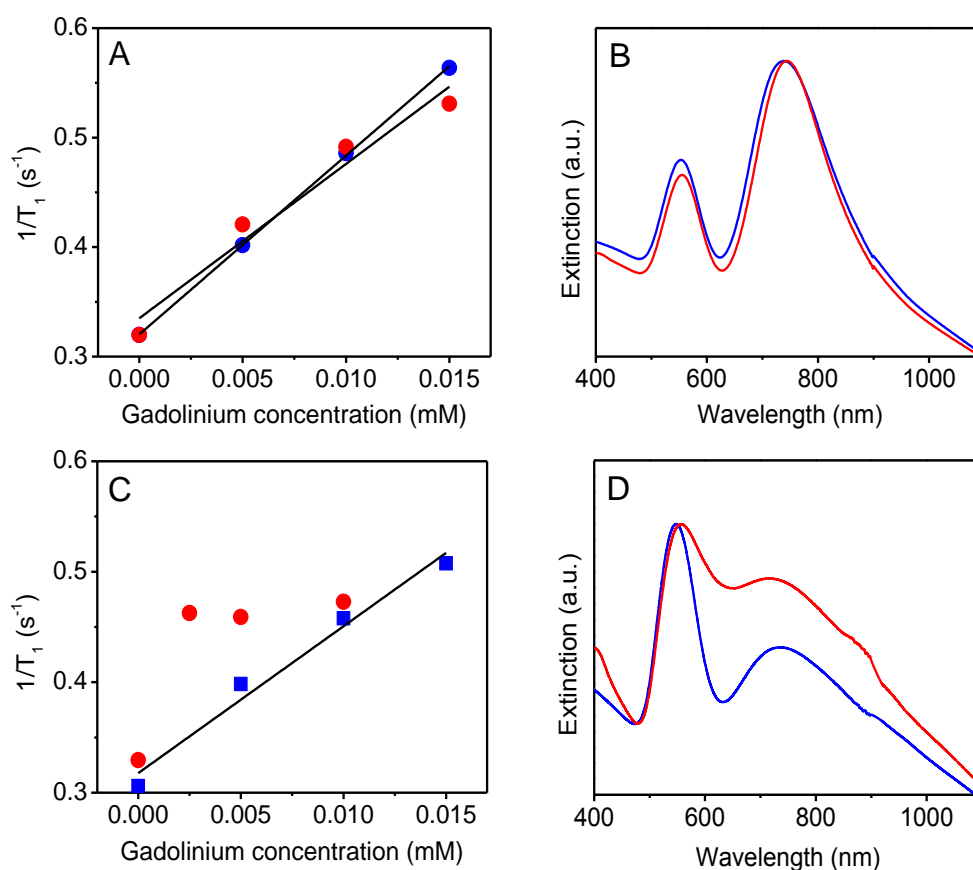


Figure 4.11 - (A) T_1 (longitudinal) rate and (B) extinction spectra for Gd-NM-PEG in water (blue) and 10% serum (red). (C) T_1 (longitudinal) rate and (D) extinction spectra GdPEG-coated NM in water (blue) and 10% serum (red). The T_1 measurements were performed at 4.7 T and 25°C.

Source: By the author.

Table 4.3 - Hydrodynamic diameter of Gd-NM-PEG and GdPEG-coated NM in water and after dispersion in culture media (FBS 10%) measured by dynamic light scattering (DLS).

Sample	In water	In FBS 10%
Gd-NM-PEG	167.0 ± 2.7 nm	168.1 ± 2.3 nm
GdPEG-coated NM	152.7 ± 2.1 nm	161.4 ± 2.4 nm

Source: By the author.

To better understand how this specific geometry impacts the Gd-NM relaxivity, we examine how the relaxivity is modified at two stages of Gd-NM synthesis. The comparative relaxivity study was performed for the seeded precursor (**Figure 4.12A**), the complete Gd-NM-PEG (**Figure 4.12B**), and the GdPEG-coated-NM (**Figure 4.12C**). For each structure, this information is accompanied by the corresponding extinction spectrum (**Figure 4.12D, E, F**) and TEM image (**Figure 4.12G, H, I**). All measurements were performed at 4.7 T and

25°C. The r_1 values were calculated to be $21.5 \text{ mM}^{-1}\text{s}^{-1}$, $17.9 \text{ mM}^{-1}\text{s}^{-1}$, and $13.6 \text{ mM}^{-1}\text{s}^{-1}$ for the seeded precursor, Gd-NM-PEG, and GdPEG-coated-NM, respectively. We find that the addition of the Au outer shell to the seeded precursor nanoparticle decreases its relaxivity, since the growth of a continuous metal shell layer limits the access of water molecules to the coordination spheres of the Gd(III) within the interior silica layer. However, the relaxivity of the GdPEG-coated-NM particles was lower than the one observed for the Gd-NM-PEG. Two effects contribute to this reduced relaxivity: (1) the Gd(III) concentration per nanoparticle for the Gd-coated-NM nanoparticles was slightly lower than for the Gd-NM-PEG, $3.9 \pm 0.7 \times 10^4$ vs. $1.5 \pm 0.4 \times 10^5$ Gd(III)/nanoparticles, and (2) additional confinement effects due to the incorporation of the Gd(III) into the silica layer in the Gd-NM-PEG case. Taking into the number of Gd(III) per nanoparticle, the relaxivity per nanoparticle was calculated to be approximately $2.7 \times 10^6 \text{ mM}^{-1} \text{ s}^{-1}$ and $5.3 \times 10^5 \text{ mM}^{-1} \text{ s}^{-1}$ for Gd-NM-PEG and GdPEG-coated-NM, respectively. For comparison, molecular chelate Gd(III) contrast agents in current clinical use typically have relaxivities r_1 of nominally $4 \text{ mM}^{-1} \text{ s}^{-1}$ per Gd(III) at 1.5 T and 37 °C.⁽²¹⁶⁾ As shown in the T_1 -weighted MRI images (**Insets of Figure 4.12A, B, and C**), the Gd-NM-PEG produced consistently brighter images than the GdPEG-coated NM, supporting its use as a T_1 agent for MRI applications.

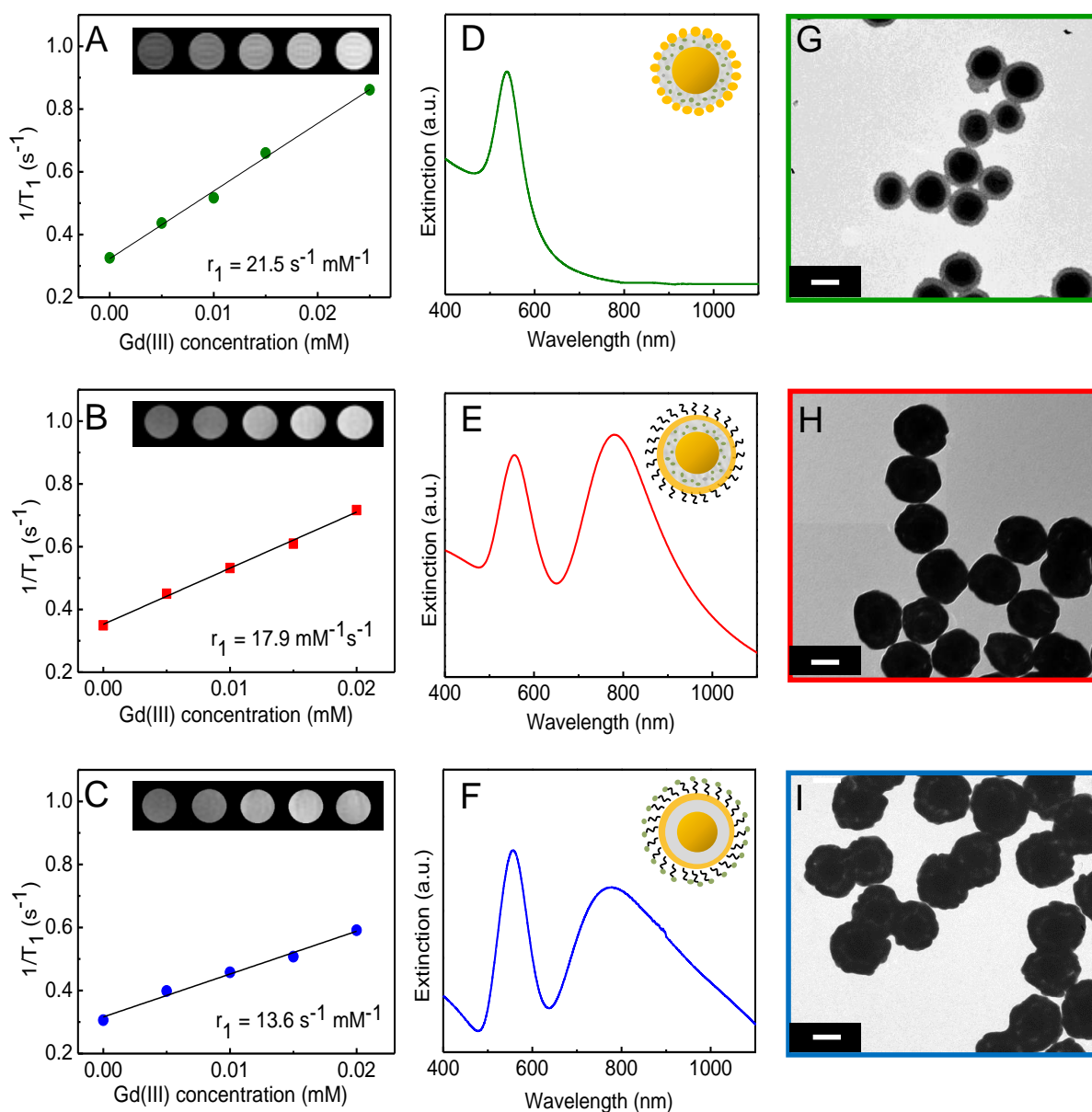


Figure 4.12 - T_1 (longitudinal) rate versus Gd(III) concentration at 4.7 T for (A) seeded precursor, (B) Gd-NM-PEG, and (C) GdPEG-coated-NM; and the corresponding (D,E,F) extinction spectra and (G,H,I) TEM images; (scale bar are 50 nm). (Insets A-C: T_1 weighted MR images).

Source: By the author.

The enhanced relaxivities of Gd(III)-containing nanostructures relative to molecular chelates can be attributed not only to the additive effect of many Gd(III) centers, but also to their slower rotational motion.(23,217) According to the Solomon-Bloembergen-Morgan (SBM) theory of paramagnetic relaxation, the main factors that affect the relaxivity of Gd(III)-based contrast agents are molecular diffusional and rotational times, number of coordinated water molecules, water proton residency lifetime and water exchange rate.(218) In general, a decrease in the molecular diffusion and rotation times leads to an increased T_1

relaxivity, especially at low magnetic fields.(23,213) Therefore, the incorporation of Gd(III) into nanostructures decreases its molecular tumbling rate, and, consequently, reduces its diffusional and rotational correlation time, increasing relaxivity.(218) Besides the enhanced T_1 relaxivity, another important advantage of nanostructured systems is the increased accumulation of carriers in target tissue, for example, exploiting the enhanced permeability and retention effect in tumors,(219) which increases the local concentration of the contrast agent in the nanoparticle case.(218)

It is worth emphasizing that our measurements were performed at 4.7 T. Higher magnetic fields provide not only a greater signal to noise, but also a higher spatial resolution and reduced acquisition times.(213) MRI scanners with higher fields, such as 3, 4.7 or even 9.4 T, have been in use clinically. However, the T_1 relaxivity of molecular Gd(III) compounds typically decreases as the magnetic field increases.(213, 220) The effect of the magnetic field on the relaxivity was shown to be more pronounced for slowly tumbling molecules than for rapidly tumbling molecules.(213) Small molecules such as Gd-DTPA show a modest decrease in r_1 with field; however, for gadolinium chelates bound to serum albumin, the relaxivity decreases from $24.3 \text{ mM}^{-1} \text{ s}^{-1}$ at 1.4 T to $11.2 \text{ mM}^{-1} \text{ s}^{-1}$ at 4.7 T. Similarly, Gd(III)-chelate-functionalized gold nanostars showed a r_1 relaxivity of $54.7 \text{ mM}^{-1} \text{ s}^{-1}$ at 1.41 T that was reduced to $9.4 \text{ mM}^{-1} \text{ s}^{-1}$ at 7 T.(32) Therefore, it is a major challenge to develop MRI contrast agents that have good r_1 and can also be used at higher magnetic fields. Gd-NMs appear to be an attractive candidate for higher-field MRI applications.

The MRI contrast mechanism depends not only on the T_1 or T_2 relaxation rate, but also on the proton density in the surrounding medium and the distance between the proton nuclei and the Gd(III). To investigate the effect of the distance between the proton nucleus and the encapsulated Gd(III) on the T_1 MRI mechanism, Gd-NM-PEG structures with two different outer Au layer thicknesses were fabricated and investigated. The T_1 longitudinal rates at 4.7 T for the Gd-NM-PEG nanoparticles with the thinner outer shell ($[r_1, r_2, r_3] = [25, 38, 56 \text{ nm}]$), and the thicker shell ($[r'_1, r'_2, r'_3] = [25, 38, 73 \text{ nm}]$) are shown in **Figure 4.13**. For the thinner shell (blue), the r_1 relaxation was $12.9 \text{ mM}^{-1} \text{ s}^{-1}$, while for the thicker shell (red), a significant decrease in r_1 relaxation, to $1.2 \text{ mM}^{-1} \text{ s}^{-1}$ (**Figure 4.13A**). A dramatic reduction in T_1 contrast for the Gd-NM-PEG with the thicker outer layer was observed (**Figure 4.13B**). In the case of the thinner Au shell, small pinhole defects in the outer layer may be present that would slightly increase the H_2O proton interaction with the internal Gd(III), enhancing the r_1 relaxivity in this case. However, we would anticipate that this enhancement could be no more than the 20% increase observed in relaxivities when

comparing the Gd-NM-PEGs with the seeded precursor nanoparticles, which represent an extremely porous outer Au layer (**Figure 4.12**). The corresponding TEM images and extinction spectra of the thin-layer and thicker-layer Gd-NM-PEG are shown (**Figure 4.13B-C**). The shifts in the extinction spectra from 747 nm to 705 nm and from 550 nm to 560 nm correspond to the reduced interlayer plasmon coupling resulting from increasing the thickness of the outer Au shell layer.(221-222)

To further investigate the observed MRI enhancement of the Gd-NM geometry, Solomon, Bloembergen and Morgan (SBM) theory (28,223) was adopted to estimate the relaxivity r_1 of the Gd-NM (**Equation 4.6**). This analysis was performed by Hui Zhang and prof. Dr. Peter Nordlander (Rice University).

$$r_1 = r_0 + r^{IS} + r^{OS} \quad (4.6)$$

where: r_0 is the intrinsic relaxivity and r^{IS} and r^{OS} are inner-sphere and outer-sphere contributions to the total relaxivity, respectively. The intrinsic relaxivity and inner-sphere contributions are assumed to be negligible, since the Gd(III) chelates are embedded within the SiO_2 shell where few H_2O molecules are present relative to the NM surroundings. According to SBM theory,(28) the outer-sphere contribution is given by:

$$r^{OS} = \frac{C}{dD} \text{Re}[3j(\omega_I) + 7j(\omega_s)] \quad (4.7)$$

Here C is a constant (for Gd(III) chelates it is $C = 5.8 \times 10^{-19} \text{m}^6 \text{s}^{-2} \text{mol}^{-1}$) and d is the distance of closest approach of H_2O molecules, here taken to be the outer Au shell thickness. D is the sum of diffusion coefficients of bulk water and of the complex is $D = 3.3 \times 10^{-9} \text{m}^2 \text{s}^{-1}$, (224) $j(\omega)$ is the spectral density function(28), and ω_I , ω_s are, the proton and electronic Larmor angular frequencies, respectively. For our calculations, the parameters of Gd-DOTA were selected(28) in accordance with the experimental conditions and the magnetic field of 4.7 T. In **Figure 4.13D** we use this analysis to plot the longitudinal relaxivity r_1 as a function of Au shell thickness for the Gd-NM nanoparticle geometry. The theoretical longitudinal relaxivity r_1 decreases with increasing Au shell thickness. The relaxivity for a Gd-NM with a 18 nm thick Au shell was measured to be $12.9 \text{mM}^{-1} \text{s}^{-1}$ while the SBM theoretical value is just slightly smaller, $\sim 9 \text{mM}^{-1} \text{s}^{-1}$; for the 38 nm shell the relaxivity was measured to be $1.5 \text{mM}^{-1} \text{s}^{-1}$, while the theoretical value for this larger shell thickness is $0.7 \text{mM}^{-1} \text{s}^{-1}$. The results are in good qualitative agreement with the theoretical model. The slightly larger value of the experimentally observed longitudinal relaxivity

relative to the theoretical analysis may indicate an enhancement due to a combination of effects not included in the SBM model. Gd(III) is weakly ferromagnetic(225) and so are Au nanoparticles under certain conditions.(226) Therefore, the interplay between Gd(III) and Au spins can give rise to a small magnetization within the outer Au shell. Nearby H₂O molecules may experience additional magnetization at a reduced distance, leading to an enhanced r_1 relaxivity.

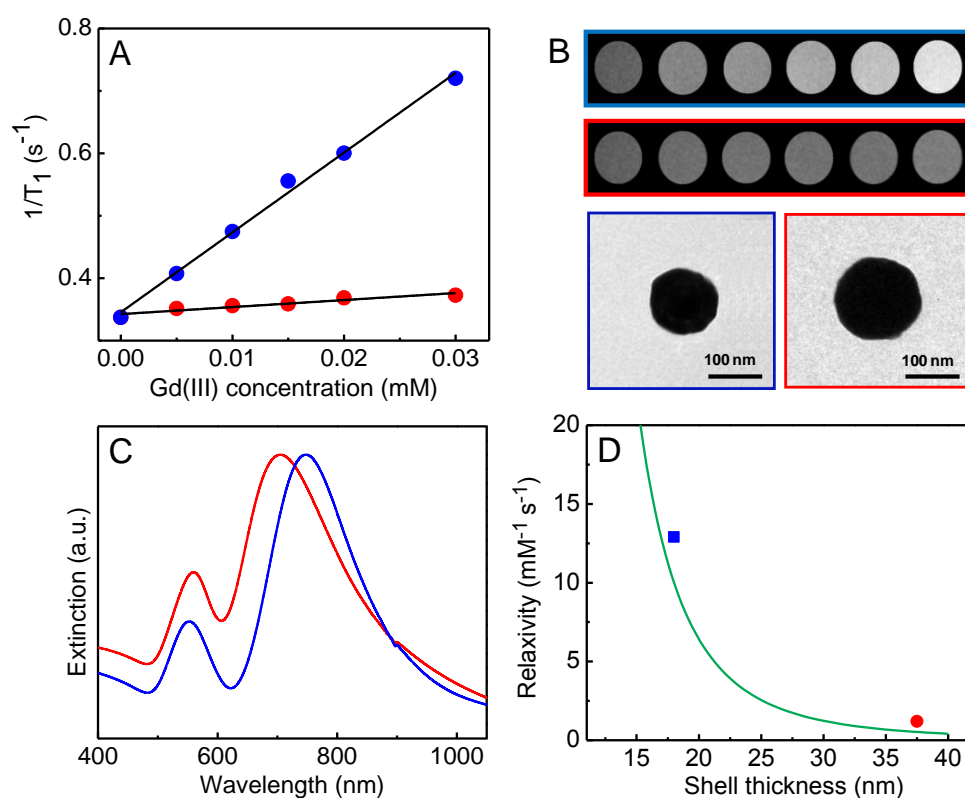


Figure 4.13 - (A) Longitudinal rate at 4.7 T versus Gd(III) concentration for two Au shell thicknesses of Gd-NM-PEG: 18 nm (blue; $r_1 = 12.9 \text{ mM}^{-1}\text{s}^{-1}$) and 38 nm (red; $r_1 = 1.2 \text{ mM}^{-1}\text{s}^{-1}$) the Gd(III) concentration per NM was 2.3×10^5 in both cases, (B) T₁ weighted MR images corresponding to the concentrations shown in (A), and corresponding TEM images. (C) extinction spectra of both Gd-NM-PEG nanoparticles as denoted in (A), and (D) the calculated longitudinal relaxivity r_1 versus Au shell thickness (green) using SBM theory (a concentration of 2.3×10^5 Gd(III) chelates per NM is used). The blue and red dots are the corresponding experimental relaxivities.

Source: By the author.

The cytotoxicity of Gd-NM-PEG and GdPEG-coated-NM in RAW 264.7 murine macrophage cells was evaluated by flow cytometry (**Figure 4.14**). The percentage of cell viability was calculated by normalizing the control (zero NM concentration) as 100%. Significant differences between control cells and cells incubated with the nanoparticles were only observed for the highest concentration of GdPEG-coated-NM (ANOVA 0.05

significance level), verifying extremely low toxicity levels under biological conditions. Differential interference contrast (DIC), reflectance (emission and excitation at 640 nm; **Figure 4.14B**) and confocal (**Figure 4.14C**) imaging were used to investigate cellular nanoparticle internalization. Clear diffraction-limited dark spots corresponding to Gd-NM-PEG complexes can be observed, verifying that the nanoparticles are internalized within the cell (**Figure 4.14B**). Z-series stacks of confocal images were obtained at various depths of field. **Figure 4.14C** corresponds to a single image slice near to the center of the cell, clearly showing that the Gd-NM-PEG (red) are internalized within the cell. The Gd-NM-PEG accumulates in high concentration in the cytoplasm close to the nucleus, and no significant morphological changes in the cells were observed.

Higher T_1 -weighted MRI signal enhancement was found in the sample of RAW 267.4 macrophage cells in PBS treated with Gd-NM-PEG (**Figure 4.14F**) compared to cells without Gd-NM-PEG (**Figure 4.14E**) and buffer reference (**Figure 4.14D**). In addition, phantoms, which have been shown increasingly importance for standardizing and optimizing scanner performance, were prepared using agarose (**Figure 4.15**). The main idea was to determine the minimal concentration of Gd-NM-PEG necessary for MR contrast in an environment more likely *in vivo* tissues. As can be seen, the MRI contrast increases as the Gd-NM-PEG concentration increases. Also, phantoms containing 2.3×10^9 nanoparticles, which corresponds to a Gd(III) concentration of $10 \mu\text{mol L}^{-1}$, was enough to produce a substantial contrast.

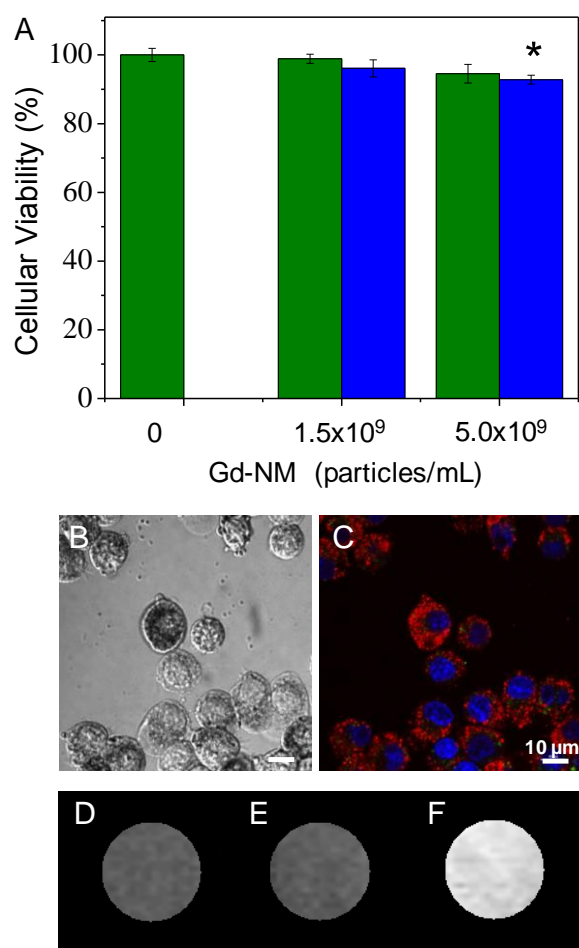


Figure 4.14 - (A) Flow cytometry toxicity analysis using SYTOX® red dead cell stain of RAW 264.7 cells after 24 h of incubation with Gd-NM-PEG (green) and Gd-coated-NM (blue). The percentages were calculated considering the control as 100%. (B) Bright field microscopy and (C) merged confocal and reflectance images of RAW 264.7 macrophage cells showing the nuclei (blue) and Gd-NM-PEG (red). T₁-weighted MR images of (D) reference (phosphate buffer solution (1x PBS)), (E) RAW 267.4 macrophage cells in PBS, and (F) RAW 267.4 macrophage cells with Gd-NM-PEG in PBS. The cell concentration was $\sim 5.2 \times 10^7$ cells/mL.

Source: By the author.

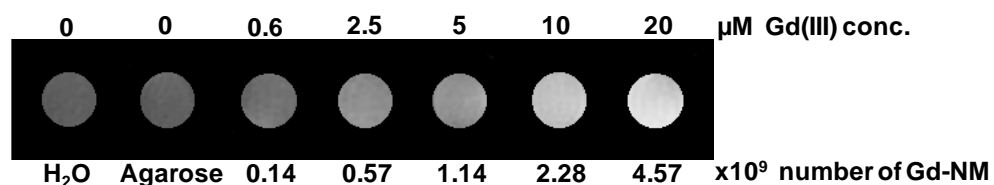


Figure 4.15 - Dependence of MR relaxation on nanoparticle concentration and Gd(III) concentration in phantom: T₁-weighted MR images of reference (water), agarose, and the equivalent number of Gd-NM-PEG (100 μL of solution).

Source: By the author.

4.4 CONCLUSIONS

The Gd(III)-encapsulating nanomatryoshkas that we have designed and synthesized provide a strong MRI T_1 enhancement. The relaxivity was enhanced even further by PEG functionalization, and increased at higher magnetic fields, a very attractive property for state-of-the-art MRI applications. The retention of the Gd(III) within the interior of the NM is excellent, unlike the case of functionalizing Gd(III) chelates on the nanoparticle surface. The enhanced relaxivity is due to longer-range interactions than are responsible for the relaxivities of molecular Gd(III) chelates, and are well-described by SBM theory. The biocompatibility, low toxicity, long term stability, and cellular uptake have been demonstrated in this study using RAW 264.7 macrophage cells. The T_1 -weighted MR image of Gd-NM internalized within RAW 264.7 macrophage cells show a substantial contrast. Given the photothermal properties that have been shown for NM in previous studies, the Gd-NM-PEG have potential applications as multifunctional agents for both diagnosis and therapy. Most importantly, the incorporation of Gd(III) into the NM structure may allow the tracking of the particles *in vivo* and investigation of their biodistribution, which is essential to develop safer and more efficient nanomaterials for medical applications.

5 CONCLUSIONS AND PERSPECTIVES

In this thesis, we have presented the fabrication of multifunctional gold based-plasmonic nanoparticles for medical applications. We have included new compounds and functionalizations into these systems, which allowed the combination of their unique optical property as phototherapeutic actuator with activated chemotherapy or diagnostic properties. Specifically, the research was focused on improving three main aspects of the gold nanomaterials for photothermal therapy: 1) synthesis of gold nanoparticles with high control of size, shape, and geometry, 2) specific cytotoxicity and enhance accumulation in tumor cells, and 3) addition of MRI agents that would allow their *in vivo* tracking and their use as diagnostic agents.

First, three types of gold based-plasmonic nanoparticles were synthesized, and the dependence of the surface plasmon resonance with parameters such as shape, size, and composition were investigated. All systems presented strong NIR absorption and diameter size less or around 100 nm, characteristics very relevant for medical applications. Their gold surface also allows conjugation of polymers and biomolecules. Gold nanorods were synthesized using the seed-mediated method in presence of CTAB with high control of size and shape. By increasing their aspect ratio, it was possible to tune the longitudinal plasmon resonance wavelength. Gold nanomatryoshkas, consisting in a gold core, an interstitial nanoscale SiO₂ layer, and a thin gold shell layer (Au/SiO₂/Au) were synthesized with high control of the thickness of the interstitial silica layer and gold shell, and, consequently, their optical properties. Further, a promising Au-coated Au₂S plasmonic material was also investigated. Since the one step synthesis usually used to fabricate these particles has not enabled a good control of the size, distribution, and composition, we proposed a two step process, in which Au₂S small particles are first synthesized and then covered with a gold layer. This strategy showed promising results with higher control of morphological parameters.

Second, we have demonstrated the successful coating of PEG-AuNRs into cellular membranes vesicles purified from A549 cancer cells and loaded with the anticancer agent β -Lapachone. The NIR irradiation led to disruption of the vesicles and release of the PEG-AuNRs and β -Lapachone, and *in vitro* studies revealed that this multifunctional noncovalent platform was capable to deliver therapeutic molecules and plasmonic nanostructures upon NIR irradiation, resulting in an enhanced cytotoxicity against A549 cancer cells. The NQO1-specific cytotoxicity of β -Lap combined with heat generated by laser irradiation of the AuNRs

result in a synergic toxicity specific for cancer cells, and no cytotoxicity was observed in absence of laser irradiation.

Finally, Gd(III)-encapsulating nanomatrixes were synthesized. The retention of the Gd(III) within the interior of the NM provide several advantages, unlike the case of functionalizing Gd(III) chelates on the nanoparticle surface. They provide a strong MRI T_1 enhancement while maintaining the strong near infrared optical properties useful for photothermal cancer therapy. The relaxivity was enhanced even further by PEG functionalization, and increased at higher magnetic fields, a very attractive property for state-of-the-art MRI applications. The enhanced relaxivity is believed to be due to longer-range interactions that are responsible for the relaxivities of molecular Gd(III) chelates, and are described by SBM theory. The biocompatibility, low toxicity, long term stability, and cellular uptake have been demonstrated in this study using RAW 264.7 macrophage cells. Most importantly, the incorporation of Gd(III) into the NM structure may allow for tracking of the particles *in vivo* and investigation of their biodistribution, which is essential to develop safer and more efficient nanomaterials for medical applications.

Given the photothermal properties that have been shown for gold nanorods and nanomatrixes, the systems developed here have potential applications as multifunctional agents for activated drug release and phototherapy, diagnosis and treatment, being strong candidates for applications in personalized cancer medicine. Further studies would be focus on the optimization of the parameters of the novel two-step synthesis process of Au-coated Au₂S nanoshells, increasing the loading of the anticancer agent β -Lap in the CM- β -Lap-PEG-AuNRs structure with a detailed investigation of their *in vitro* and *in vivo* photothermal cytotoxicity mechanism, and *in vivo* MIR investigation of Gd-NM.

REFERENCES

- 1 FERLAY, J. et al. GLOBOCAN 2012 v1.0, cancer incidence and mortality worldwide: IARC cancerbase No. 11. Lyon, France, 2013. Available from: <http://globocan.iarc.fr/>. Accessibile at: 23 Jan. 2016.
- 2 SALEM, A. K. et al. Multifunctional nanorods for gene delivery. **Nature Materials**, v. 2, n. 10, p. 668-671, 2003.
- 3 TASCIOTTI, E. et al. Mesoporous silicon particles as a multistage delivery system for imaging and therapeutic applications. **Nature Nanotechnology**, v. 3, p. 151 - 157, 2008.
- 4 NA, H. B. et al. Inorganic Nanoparticles for MRI Contrast Agent. **Advanced Materials**, v. 21, n. 21, p. 2133–2148, 2009.
- 5 O'NEAL, D. P. et al. Photo-thermal tumor ablation in mice using near infrared-absorbing nanoparticles. **Cancer Letters**, v. 209, n. 2, p. 171-176, 2004.
- 6 BARDHAN, R. et al. Theranostic Nanoshells: From Probe Design to Imaging and Treatment of Cancer. **Accounts of Chemical Research**, v. 44, n. 10, p. 936-946, 2011.
- 7 O'NEAL, D. P. et al. Photo-thermal tumor ablation in mice using near infrared-absorbing nanoparticles. **Cancer Letters**, v. 209, n. 2, p. 171-176, 2004.
- 8 WEISSLEDER, R. A clearer vision for in vivo imaging. **Nature Nanotechnology**, v. 19, n. 4, p. 316-317, 2001.
- 9 DICKERSON, E. B. et al. Gold nanorod assisted near-infrared plasmonic photothermal therapy (PPTT) of squamous cell carcinoma in mice. **Cancer Letters**, v. 269, n. 1, p. 57-66, 2008.
- 10 AYALA-OROZCO, C. et al. Au Nanomaterials as Efficient Near-Infrared Photothermal Transducers for Cancer Treatment: Benchmarking against Nanoshells. **ACS Nano**, v. 8, n. 6, p. 6372-6381, 2014.
- 11 AYALA-OROZCO, C. et al. Sub-100 nm gold nanomaterials improve photo-thermal therapy efficacy in large and highly aggressive triple negative breast tumors. **Journal of Controlled Release**, v. 191, p. 90-97, 2014. doi: 10.1016/j.jconrel.2014.07.038.
- 12 PARODI, A. et al. Synthetic nanoparticles functionalized with biomimetic leukocyte membranes possess cell-like functions. **Nature Nanotechnology**, v. 8, n. 1, p. 61-68, 2013.
- 13 SANHAI, W. R. et al. Seven challenges for nanomedicine. **Nature Nanotechnology**, v. 3, n. 5, p. 242-244, 2008.
- 14 OWENS, D. E.; PEPPAS, N. A. Opsonization, biodistribution, and pharmacokinetics of polymeric nanoparticles. **International Journal of Pharmaceutics**, v. 307, n. 1, p. 93-102, 2006.

- 15 KNOP, K. et al. Poly(ethylene glycol) in drug delivery: pros and cons as well as potential alternatives. **Angewandte Chemie International Edition**, v. 49, n. 36, p. 6288-6308, 2010.
- 16 HU, C. M. J. et al. Erythrocyte membrane-camouflaged polymeric nanoparticles as a biomimetic delivery platform. **Proceedings of the National Academy of Sciences of the United States of America**, v. 108, n. 27, p. 10980-10985, 2011.
- 17 HU, C. M. J. et al. 'Marker-of-self' functionalization of nanoscale particles through a top-down cellular membrane coating approach. **Nanoscale**, v. 5, n. 7, p. 2664-2668, 2013.
- 18 FANG, R. H. et al. Cancer cell membrane-coated nanoparticles for anticancer vaccination and drug delivery. **Nano Letters**, v. 14, n. 4, p. 2181-2188, 2014.
- 19 SHAO, K. et al. Nanoparticle-Based Immunotherapy for Cancer. **ACS Nano**, v. 9, n. 1, p. 16-30, 2015.
- 20 FURMAN, N. E. T. et al. Reconstructed stem cell nanoghosts: a natural tumor targeting platform. **Nano Letters**, v. 13, n. 7, p. 3248-3255, 2013.
- 21 MERBACH, A. et al. **The chemistry of contrast agents in medical magnetic resonance imaging**. 2 nd ed. New York: John Wiley & Sons, 2013.
- 22 AGULLA, J. et al. Quick adjustment of imaging tracer payload, for in vivo applications of theranostic nanostructures in the brain. **Nanomedicine: nanotechnology, biology, and medicine**, v. 3, n. 4, p. 851-858, 2014.
- 23 DUMAS, S. et al. High Relaxivity Magnetic Resonance Imaging Contrast Agents Part 1 Impact of Single Donor Atom Substitution on Relaxivity of Serum Albumin-Bound Gadolinium Complexes. **Investigative Radiology**, v. 45, n. 10, p. 600-612, 2010.
- 24 NAA, H. B.; HYEON, T. Nanostructured T1 MRI contrast agents. **Journal of Materials Chemistry**, v. 19, n. 35, p. 6267-6273, 2009.
- 25 PENFIELD, J. G.; JR, R. F. R. What nephrologists need to know about gadolinium. **Nature Clinical Practice Nephrology**, v. 3, p. 654-668, 2007. doi:10.1038/ncpneph0660.
- 26 BROOME, D. R. Nephrogenic systemic fibrosis associated with gadolinium based contrast agents: a summary of the medical literature reporting. **European Journal of Radiology**, v. 66, n. 2, p. 230-234, 2008.
- 27 DAVENPORT, A.; WHITING, S. Profound pseudohypocalcemia due to gadolinium (Magnevist) contrast in a hemodialysis patient. **American Journal of Kidney Diseases**, v. 47, n. 2, p. 350-352, 2006.
- 28 ANANTA, J. S. et al. Geometrical confinement of gadolinium-based contrast agents in nanoporous particles enhances T-1 contrast. **Nature Nanotechnology**, v. 5, n. 11, p. 815-821, 2010.
- 29 WEN, S. et al. Multifunctional dendrimer-entrapped gold nanoparticles for dual mode CT/MR imaging applications. **Biomaterials**, v. 34, n. 5, p. 1570-1580, 2013.

- 30 LIU, Y. et al. Gadolinium-loaded polymeric nanoparticles modified with Anti-VEGF as multifunctional MRI contrast agents for the diagnosis of liver cancer. **Biomaterials**, v. 32, n. 22, p. 5167–5176, 2011.
- 31 COUGHLIN, A. J. et al. Gadolinium-Conjugated Gold Nanoshells for Multimodal Diagnostic Imaging and Photothermal Cancer Therapy. **Small**, v. 10, n. 3, p. 556–565, 2014.
- 32 ROTZ, M. W. et al. High Relaxivity Gd(III) - DNA Gold Nanostars: Investigation of Shape Effects on Proton Relaxation. **ACS Nano**, v. 9, n. 3, p. 3385-3396, 2015.
- 33 HUANG, X. H. et al. Gold Nanorods: From Synthesis and Properties to Biological and Biomedical Applications. **Advanced Materials**, v. 21, n. 48, p. 4880-4910, 2009.
- 34 HUANG, X. H. et al. Plasmonic photothermal therapy (PPTT) using gold nanoparticles. **Lasers in Medical Science**, v. 23, n. 3, p. 217-228, 2008.
- 35 PEREZ-JUSTE, J. et al. Gold nanorods: Synthesis, characterization and applications. **Coordination Chemistry Reviews**, v. 249, n. 17-18, p. 1870-1901, 2005.
- 36 LINIC, S. et al. Plasmonic-metal nanostructures for efficient conversion of solar to chemical energy. **Nature Materials**, v. 10, n. 12, p. 911-921, 2011.
- 37 LIAO, H. W.; HAFNER, J. H. Gold nanorod bioconjugates. **Chemistry of Materials**, v. 17, n. 18, p. 4636-4641, 2005.
- 38 STUART, H. R.; HALL, D. G. Absorption enhancement in silicon-on-insulator waveguides using metal island films. **Applied Physics Letters**, v. 69, n. 16, p. 2327-2329, 1996.
- 39 SCHAADT, D. M. et al. Enhanced semiconductor optical absorption via surface plasmon excitation in metal nanoparticles. **Applied Physics Letters**, v. 86, n. 6, 2005.
- 40 NEUMANN, O. et al. Nanoparticle-Mediated, Light-Induced Phase Separations. **Nano Letters**, v. 15, n. 12, p. 7880-7885, 2015.
- 41 NEUMANN, O. et al. Compact solar autoclave based on steam generation using broadband light-harvesting nanoparticles. **Proceedings of the National Academy of Sciences of the United States of America**, v. 110, n. 29, p. 11677-11681, 2013.
- 42 BARDHAN, R. et al. Fluorescence Enhancement by Au Nanostructures: Nanoshells and Nanorods. **ACS Nano**, v. 3, n. 3, p. 744-752, 2009.
- 43 AYALA-OROZCO, C. et al. Fluorescence Enhancement of Molecules Inside a Gold Nanomatryoshka. **Nano Letters**, v. 14, n. 5, p. 2926-2933, 2014.
- 44 HU, M. et al. Dark-field microscopy studies of single metal nanoparticles: understanding the factors that influence the linewidth of the localized surface plasmon resonance. **Journal of Materials Chemistry**, v. 18, n. 17, p. 1949-1960, 2008.

- 45 AARON, J. et al. Plasmon resonance coupling of metal nanoparticles for molecular imaging of carcinogenesis in vivo. **Journal of Biomedical Optics**, v. 12, n. 3, p. 034007, 2007.
- 46 DURR, N. J. et al. Two-photon luminescence imaging of cancer cells using molecularly targeted gold nanorods. **Nano Letters**, v. 7, n. 4, p. 941-945, 2007.
- 47 LEVIN, C. S. et al. Nanoshell-based substrates for surface enhanced spectroscopic detection of biomolecules. **Analyst**, v. 134, n. 9, p. 1745-1750, 2009.
- 48 LOMBARDINI, R. et al. Plasmonic Enhancement of Raman Optical Activity in Molecules near Metal Nanoshells: Theoretical Comparison of Circular Polarization Methods. **Journal of Physical Chemistry C**, v. 114, n. 16, p. 7390-7400, 2010.
- 49 CAI, X. et al. In Vivo Quantitative Evaluation of the Transport Kinetics of Gold Nanocages in a Lymphatic System by Noninvasive Photoacoustic Tomography. **ACS Nano**, v. 5, n. 12, p. 9658-9667, 2011.
- 50 TRUONG, P. L. et al. A new method for non-labeling attomolar detection of diseases based on an individual gold nanorod immunosensor. **Lab on a Chip**, v. 11, n. 15, p. 2591-2597, 2011.
- 51 CONGUR, G. et al. Voltammetric and impedimetric DNA detection at single-use graphite electrodes modified with gold nanorods. **Colloids and Surfaces B: biointerfaces**, v. 112, p. 61-66, 2013.
- 52 GUO, Y. J. et al. Multifunctional optical probe based on gold nanorods for detection and identification of cancer cells. **Sensors and Actuators B-chemical**, v. 191, p. 741-749, 2014.
- 53 AYALA-OROZCO, C. et al. Sub-100 nm gold nanomatryoshkas improve photo-thermal therapy efficacy in large and highly aggressive triple negative breast tumors. **Journal of Controlled Release**, v. 191, p. 90-97, 2014.
- 54 HUANG, X. H. et al. Cancer cell imaging and photothermal therapy in the near-infrared region by using gold nanorods. **Journal of the American Chemical Society**, v. 128, n. 6, p. 2115-2120, 2006.
- 55 HUSCHKA, R. et al. Light-Induced Release of DNA from gold nanoparticles: nanoshells and nanorods. **Journal of the American Chemical Society**, v. 133, n. 31, p. 12247-12255, 2011.
- 56 DE ABERASTURI, D. J. et al. Modern applications of plasmonic nanoparticles: from energy to health. **Advanced Optical Materials**, v. 3, n. 5, p. 602-617, 2015.
- 57 MAEDA, H. et al. Polymeric drugs for efficient tumor-targeted drug delivery based on EPR-effect. **European Journal of Pharmaceutics and Biopharmaceutics**, v. 71, n. 3, p. 409-419, 2009.
- 58 JAIN, P. K. et al. Au nanoparticles target cancer. **Nano Today**, v. 2, n. 1, p. 18-29, 2007.

- 59 EL-SAYED, M. A. Some interesting properties of metals confined in time and nanometer space of different shapes. **Accounts of Chemical Research**, v. 34, n. 4, p. 257-264, 2001.
- 60 NIKOOBAKHT, B.; EL-SAYED, M. A. Surface-enhanced Raman scattering studies on aggregated gold nanorods. **Journal of Physical Chemistry A**, v. 107, n. 18, p. 3372-3378, 2003.
- 61 LINK, S. et al. Simulation of the optical absorption spectra of gold nanorods as a function of their aspect ratio and the effect of the medium dielectric constant. **Journal of Physical Chemistry B**, v. 103, n. 16, p. 3073-3077, 1999.
- 62 LINK, S. et al. Simulation of the optical absorption spectra of gold nanorods as a function of their aspect ratio and the effect of the medium dielectric constant (vol 103B, pg 3073, 1999). **Journal of Physical Chemistry B**, v. 109, n. 20, p. 10531-10532, 2005.
- 63 CHON, J. W. M. et al. Spectral encoding on gold nanorods doped in a silica sol-gel matrix and its application to high-density optical data storage. **Advanced Functional Materials**, v. 17, n. 6, p. 875-880, 2007.
- 64 HUSCHKA, R. et al. Gene silencing by gold nanoshell-mediated delivery and laser-triggered release of antisense oligonucleotide and siRNA. **ACS Nano**, v. 6, n. 9, p. 7681-7691, 2012.
- 65 COLE, J. R. et al. Photothermal efficiencies of nanoshells and nanorods for clinical therapeutic applications. **Journal of Physical Chemistry C**, v. 113, n. 28, p. 12090-12094, 2009.
- 66 CHEN, W. X. et al. Targeting pancreatic cancer with magneto-fluorescent theranostic gold nanoshells. **Nanomedicine**, v. 9, n. 8, p. 1209-1222, 2014.
- 67 BARDHAN, R. et al. Nanosphere-in-a-nanoshell: a simple nanomatrix. **Journal of Physical Chemistry C**, v. 114, n. 16, p. 7378-7383, 2010.
- 68 PRODAN, E. et al. A hybridization model for the plasmon response of complex nanostructures. **Science**, v. 302, n. 5644, p. 419-422, 2003.
- 69 ERICKSON, T. A.; TUNNELL, J. W. Gold nanoshells in biomedical applications. In: **Nanotechnologies for the life sciences**. New York: Wiley-VCH Verlag, 2007. ISBN 9783527610419.
- 70 ZHOU, H. S. et al. Controlled synthesis and quantum-size effect in gold-coated nanoparticles. **Physical Review B**, v. 50, n. 16, p. 12052-12056, 1994.
- 71 JAIN, S. et al. Gold nanoparticles as novel agents for cancer therapy. **British Journal of Radiology**, v. 85, n. 1010, p. 101-113, 2012.
- 72 SAU, T. K.; MURPHY, C. J. Seeded high yield synthesis of short Au nanorods in aqueous solution. **Langmuir**, v. 20, n. 15, p. 6414-6420, 2004.

- 73 DUFF, D. G. et al. A new hydrosol of gold clusters. 1. formation and particle size variation. **Langmuir**, v. 9, n. 9, p. 2301-2309, 1993.
- 74 AVERITT, R. D. et al. Plasmon resonance shifts of Au-coated Au₂S nanoshells: insight into multicomponent nanoparticle growth. **Physical Review Letters**, v. 78, n. 22, p. 4217-4220, 1997.
- 75 SUN, X. M. et al. Separation of nanoparticles in a density gradient: FeCo@C and gold nanocrystals. **Angewandte Chemie International Edition**, v. 48, n. 5, p. 939-942, 2009.
- 76 MORRIS, T. et al. Synthesis and characterization of gold sulfide nanoparticles. **Langmuir**, v. 18, n. 2, p. 535-539, 2002.
- 77 HAISS, W. et al. Determination of size and concentration of gold nanoparticles from UV-Vis spectra. **Analytical Chemistry**, v. 79, n. 11, p. 4215-4221, 2007.
- 78 NIKOBAKH, B.; EL-SAYED, M. A. Preparation and growth mechanism of gold nanorods (NRs) using seed-mediated growth method. **Chemistry of Materials**, v. 15, n. 10, p. 1957-1962, 2003.
- 79 LIU, M. Z.; GUYOT-SIONNEST, P. Mechanism of silver(I)-assisted growth of gold nanorods and bipyramids. **Journal of Physical Chemistry B**, v. 109, n. 47, p. 22192-22200, 2005.
- 80 WALSH, M. J. et al. Symmetry breaking and silver in gold nanorod growth. **ACS Nano**, v. 9, n. 1, p. 715-724, 2015.
- 81 STÖBER, W. et al. Controlled growth of monodisperse silica spheres in micron size range. **Journal of Colloid and Interface Science**, v. 26, n. 1, p. 62-69, 1968.
- 82 KLEKOTKO, M. et al. Bio-mediated synthesis, characterization and cytotoxicity of gold nanoparticles. **Physical Chemistry Chemical Physics**, v. 17, n. 43, p. 29014-29019, 2015.
- 83 WU, H. Y. et al. Direct synthesis of branched gold nanocrystals and their transformation into spherical nanoparticles. **Journal of Physical Chemistry B**, v. 110, n. 39, p. 19291-19294, 2006.
- 84 YUAN, H. K. et al. In vivo particle tracking and photothermal ablation using plasmon-resonant gold nanostars. **Nanomedicine -nanotechnology biology and medicine**, v. 8, n. 8, p. 1355-1363, 2012.
- 85 CHABNER, B. A.; ROBERTS, T. G. Timeline - chemotherapy and the war on cancer. **Nature Reviews Cancer**, v. 5, n. 1, p. 65-72, 2005.
- 86 KIM, J. et al. Multifunctional nanostructured materials for multimodal imaging, and simultaneous imaging and therapy. **Chemical Society Reviews**, v. 38, n. 2, p. 372-390, 2009.
- 87 BARDHAN, R. et al. Theranostic nanoshells: from probe design to imaging and treatment of cancer. **Accounts of Chemical Research**, v. 44, n. 10, p. 936-946, 2011.

- 88 JORI, G.; SPIKES, J. D. Photothermal sensitizers - possible use in tumor-therapy. **Journal of Photochemistry and Photobiology B - biology**, v. 6, n. 1-2, p. 93-101, 1990.
- 89 LINK, S.; EL-SAYED, M. A. Shape and size dependence of radiative, non-radiative and photothermal properties of gold nanocrystals. **International Reviews in Physical Chemistry**, v. 19, n. 3, p. 409-453, 2000.
- 90 ABADDEER, N. S.; MURPHY, C. J. Recent progress in cancer thermal therapy using gold nanoparticles. **Journal of Physical Chemistry C**, v. 120, n. 9, p. 4691-4716, 2016.
- 91 SMITH, A. M. et al. BIOIMAGING second window for in vivo imaging. **Nature Nanotechnology**, v. 4, n. 11, p. 710-711, 2009.
- 92 MARANGONI, V. S. et al. Synthesis, physico-chemical properties, and biomedical applications of gold nanorods: a review. **Journal of Biomedical Nanotechnology**, v. 12, n. 6, p. 1136-1158, 2016.
- 93 PARDRIDGE, W. M. shRNA and siRNA delivery to the brain. **Advanced Drug Delivery Reviews**, v. 59, n. 2-3, p. 141-152, 2007.
- 94 HUANG, H. C. et al. Simultaneous enhancement of photothermal stability and gene delivery efficacy of gold nanorods using polyelectrolytes. **ACS Nano**, v. 3, n. 10, p. 2941-2952, 2009.
- 95 BRANNON-PEPPAS, L.; BLANCHETTE, J. O. Nanoparticle and targeted systems for cancer therapy. **Advanced Drug Delivery Reviews**, v. 56, n. 11, p. 1649-1659, 2004.
- 96 LOO, C. et al. Nanoshell-enabled photonics-based imaging and therapy of cancer. **Technology in Cancer Research & Treatment**, v. 3, n. 1, p. 33-40, 2004.
- 97 GAD, S. C. et al. Evaluation of the toxicity of intravenous delivery of auroshell particles (Gold-Silica Nanoshells). **International Journal of Toxicology**, v. 31, n. 6, p. 584-594, 2012.
- 98 ANSELMO, A. C.; MITRAGOTRI, S. A Review of clinical translation of inorganic nanoparticles. **AAPS Journal**, v. 17, n. 5, p. 1041-1054, 2015.
- 99 OKUNO, T. et al. Photothermal therapy of tumors in lymph nodes using gold nanorods and near-infrared laser light. **Journal of Controlled Release**, v. 172, n. 3, p. 879-884, 2013.
- 100 MALLICK, S. et al. Silica coated gold nanorods for imaging and photo-thermal therapy of cancer cells. **Journal of Nanoscience and Nanotechnology**, v. 13, n. 5, p. 3223-3229, 2013.
- 101 TONG, L. et al. Gold nanorods mediate tumor cell death by compromising membrane integrity. **Advanced Materials**, v. 19, n. 20, p. 3136-+, 2007.
- 102 LI, J. L.; GU, M. Surface plasmonic gold nanorods for enhanced two-photon microscopic imaging and apoptosis induction of cancer cells. **Biomaterials**, v. 31, n. 36, p. 9492-9498, 2010.

- 103 CHEN, C. L. et al. In situ real-time investigation of cancer cell photothermolysis mediated by excited gold nanorod surface plasmons. **Biomaterials**, v. 31, n. 14, p. 4104-4112, 2010.
- 104 CHEN, H. Y. et al. Combined chemo- and photo-thermal therapy delivered by multifunctional theranostic gold nanorod-loaded microcapsules. **Nanoscale**, v. 7, n. 19, p. 8884-8897, 2015.
- 105 LIAO, J. F. et al. Combined Cancer photothermal-chemotherapy based on doxorubicin/gold nanorod-loaded polymersomes. **Theranostics**, v. 5, n. 4, p. 345-356, 2015.
- 106 HUANG, X. et al. The conjugates of gold nanorods and chlorin e6 for enhancing the fluorescence detection and photodynamic therapy of cancers. **Physical Chemistry Chemical Physics**, v. 15, n. 38, p. 15727-15733, 2013.
- 107 WANG, J. et al. Photosensitizer-gold nanorod composite for targeted multimodal therapy. **Small**, v. 9, n. 21, p. 3678-3684, 2013.
- 108 KUO, W. S. et al. Gold nanomaterials conjugated with indocyanine green for dual-modality photodynamic and photothermal therapy. **Biomaterials**, v. 33, n. 11, p. 3270-3278, 2012.
- 109 YANG, L. L. et al. Single chain epidermal growth factor receptor antibody conjugated nanoparticles for in vivo tumor targeting and imaging. **Small**, v. 5, n. 2, p. 235-243, 2009.
- 110 OYELERE, A. K. et al. Peptide-conjugated gold nanorods for nuclear targeting. **Bioconjugate Chemistry**, v. 18, n. 5, p. 1490-1497, 2007.
- 111 MEDLEY, C. D. et al. Aptamer-conjugated nanoparticles for cancer cell detection. **Analytical Chemistry**, v. 83, n. 3, p. 727-734, 2011.
- 112 SALVATI, A. et al. Transferrin-functionalized nanoparticles lose their targeting capabilities when a biomolecule corona adsorbs on the surface. **Nature Nanotechnology**, v. 8, n. 2, p. 137-143, 2013.
- 113 MONOPOLI, M. P. et al. Biomolecular coronas provide the biological identity of nanosized materials. **Nature Nanotechnology**, v. 7, n. 12, p. 779-786, 2012.
- 114 XIAO, Y. L. et al. Gold nanorods conjugated with doxorubicin and cRGD for combined anticancer drug delivery and PET imaging. **Theranostics**, v. 2, n. 8, p. 757-768, 2012.
- 115 SANHAI, W. R. et al. Seven challenges for nanomedicine. **Nature Nanotechnology**, v. 3, n. 5, p. 242-244, 2008.
- 116 GAO, W. W. et al. Surface functionalization of gold nanoparticles with red blood cell membranes. **Advanced Materials**, v. 25, n. 26, p. 3549-3553, 2013.

- 117 PIAO, J.-G. et al. Erythrocyte membrane is an alternative coating to polyethylene glycol for prolonging the circulation lifetime of gold nanocages for photothermal therapy. **Acs Nano**, v. 8, n. 10, p. 10414-10425, 2014.
- 118 BRAHLER, M. et al. Magnetite-loaded carrier erythrocytes as contrast agents for magnetic resonance imaging. **Nano Letters**, v. 6, n. 11, p. 2505-2509, 2006.
- 119 DING, H. et al. Erythrocyte membrane-coated NIR-triggered biomimetic nanovectors with programmed delivery for photodynamic therapy of cancer. **Nanoscale**, v. 7, n. 21, p. 9806-9815, 2015.
- 120 BAHMANI, B. et al. Erythrocyte-derived photo-theranostic agents: hybrid nano-vesicles containing indocyanine green for near infrared imaging and therapeutic applications. **Scientific Reports**, v. 3, 2013.
- 121 PATEL, P. D. et al. Drug loaded erythrocytes: As novel drug delivery system. **Current Pharmaceutical Design**, v. 14, n. 1, p. 63-70, 2008.
- 122 GUPTA, N. et al. Nano-engineered erythrocyte ghosts as inhalational carriers for delivery of fasudil: preparation and characterization. **Pharmaceutical Research**, v. 31, n. 6, p. 1553-1565, 2014.
- 123 TANG, K. et al. Delivery of chemotherapeutic drugs in tumour cell-derived microparticles. **Nature Communications**, v. 3, 2012.
- 124 ZHANG, L. et al. Beta-lapachone and paclitaxel combination micelles with improved drug encapsulation and therapeutic synergy as novel nanotherapeutics for NQO1-targeted cancer therapy. **Molecular Pharmaceutics**, v. 12, n. 11, p. 3999-4010, 2015.
- 125 HOOKER, S. C. The constitution of lapachol and its derivatives part V the structure of Paterno's "isolapachone". **Journal of the American Chemical Society**, v. 58, n. 7, p. 1190-1197, 1936.
- 126 PINK, J. J. et al. NAD(P)H : quinone oxidoreductase activity is the principal determinant of beta-lapachone cytotoxicity. **Journal of Biological Chemistry**, v. 275, n. 8, p. 5416-5424, 2000.
- 127 PARK, H. J. et al. Heat-induced up-regulation of NAD(P)H: quinone oxidoreductase potentiates anticancer effects of beta-lapachone. **Clinical Cancer Research**, v. 11, n. 24, p. 8866-8871, 2005.
- 128 BLANCO, E. et al. Beta-Lapachone-containing PEG-PLA polymer micelles as novel nanotherapeutics against NQO1-overexpressing tumor cells. **Journal of Controlled Release**, v. 122, n. 3, p. 365-374, 2007.
- 129 SIGMA-ALDRICH. beta-Lapachone. Available from: <http://www.sigmaaldrich.com/catalog/product/sigma/12037>. Accessible at: 12 Mar. 2016.
- 130 PARDEE, A. B. et al. Cancer therapy with beta-lapachone. **Current Cancer Drug Targets**, v. 2, n. 3, p. 227-242, 2002.

- 131 NASONGKLA, N. et al. Enhancement of solubility and bioavailability of beta-lapachone using cyclodextrin inclusion complexes. **Pharmaceutical Research**, v. 20, n. 10, p. 1626-1633, 2003.
- 132 BLANCO, E. et al. beta-Lapachone micellar nanotherapeutics for non-small cell lung cancer therapy. **Cancer Research**, v. 70, n. 10, p. 3896-3904, 2010.
- 133 ZHENG, X. T.; LI, C. M. Restoring basal planes of graphene oxides for highly efficient loading and delivery of beta-lapachone. **Molecular Pharmaceutics**, v. 9, n. 3, p. 615-621, 2012.
- 134 JEONG, S. Y. et al. Systemic delivery and preclinical evaluation of Au nanoparticle containing beta-lapachone for radiosensitization. **Journal of Controlled Release**, v. 139, n. 3, p. 239-245, 2009.
- 135 SCHRURS, F.; LISON, D. Focusing the research effort. **Nature Nanotechnology**, v. 7, n. 9, p. 546-548, 2012.
- 136 KHLEBTSOV, N.; DYKMAN, L. Biodistribution and toxicity of engineered gold nanoparticles: a review of in vitro and in vivo studies. **Chemical Society Reviews**, v. 40, n. 3, p. 1647-1671, 2011.
- 137 QIU, Y. et al. Surface chemistry and aspect ratio mediated cellular uptake of Au nanorods. **Biomaterials**, v. 31, n. 30, p. 7606-7619, 2010.
- 138 LAU, I. P. et al. In vitro effect of CTAB- and PEG-coated gold nanorods on the induction of eryptosis/erythroptosis in human erythrocytes. **Nanotoxicology**, v. 6, n. 8, p. 847-856, 2012.
- 139 WANG, Y. C. et al. Comparison study of gold nanoheptapods, nanorods, and nanocages for photothermal cancer treatment. **ACS Nano**, v. 7, n. 3, p. 2068-2077, 2013.
- 140 DINISH, U. S. et al. Optimized synthesis of PEG-encapsulated gold nanorods for improved stability and its application in OCT imaging with enhanced contrast. **Plasmonics**, v. 8, n. 2, p. 591-598, 2013.
- 141 JOKERST, J. V. et al. Nanoparticle PEGylation for imaging and therapy. **Nanomedicine**, v. 6, n. 4, p. 715-728, 2011.
- 142 WANG, L. M. et al. Revealing the binding structure of the protein corona on gold nanorods using synchrotron radiation-based techniques: understanding the reduced damage in cell membranes. **Journal of the American Chemical Society**, v. 135, n. 46, p. 17359-17368, 2013.
- 143 ADURA, C. et al. Stable conjugates of peptides with gold nanorods for biomedical applications with reduced effects on cell viability. **ACS Applied Materials & Interfaces**, v. 5, n. 10, p. 4076-4085, 2013.

- 144 LUND, R. et al. Efficient isolation and quantitative proteomic analysis of cancer cell plasma membrane proteins for identification of metastasis-associated cell surface markers. **Journal of Proteome Research**, v. 8, n. 6, p. 3078-3090, 2009.
- 145 DESCHRIJVER, R.; VERMEULEN, D. Separation and quantitation of phospholipids in animal-tissues by iatrosan TLC/FID. **Lipids**, v. 26, n. 1, p. 74-76, 1991.
- 146 DE, M. et al. Biomimetic interactions of proteins with functionalized nanoparticles: a thermodynamic study. **Journal of the American Chemical Society**, v. 129, n. 35, p. 10747-10753, 2007.
- 147 BAIER, G. et al. BSA Adsorption on Differently Charged Polystyrene Nanoparticles using Isothermal Titration Calorimetry and the Influence on Cellular Uptake. **Macromolecular Bioscience**, v. 11, n. 5, p. 628-638, 2011.
- 148 OZCAN, I. et al. Pegylation of poly(gamma-benzyl-L-glutamate) nanoparticles is efficient for avoiding mononuclear phagocyte system capture in rats. **International Journal of Nanomedicine**, v. 5, p. 1103-1111, 2010. doi: 10.2147/IJN.S15493.
- 149 YEN, H. J. et al. Cytotoxicity and immunological response of gold and silver nanoparticles of different sizes. **Small**, v. 5, n. 13, p. 1553-1561, 2009.
- 150 RAO, J. S. et al. Inhibition of invasion, angiogenesis, tumor growth, and metastasis by adenovirus-mediated transfer of antisense uPAR and MMP-9 in non-small cell lung cancer cells. **Molecular Cancer Therapeutics**, v. 4, n. 9, p. 1399-1408, 2005.
- 151 TAN, S. W. et al. Cell or cell membrane-based drug delivery systems. **Theranostics**, v. 5, n. 8, p. 863-881, 2015.
- 152 LEE, J. et al. Liposome-based engineering of cells to package hydrophobic compounds in membrane vesicles for tumor penetration. **Nano Letters**, v. 15, n. 5, p. 2938-2944, 2015.
- 153 SCHRIER, S. L. et al. Energized endocytosis in human erythrocyte-ghosts. **Journal of Clinical Investigation**, v. 56, n. 1, p. 8-22, 1975.
- 154 NGHIEM, T. H. L. et al. Synthesis, capping and binding of colloidal gold nanoparticles to proteins. **Advances in Natural Sciences: nanoscience and nanotechnology**, v. 1, n. 2, p. 025009, 2010.
- 155 WANG, L. B. et al. Side-by-Side and end-to-end gold nanorod assemblies for environmental toxin sensing. **Angewandte Chemie International Edition**, v. 49, n. 32, p. 5472-5475, 2010.
- 156 URBAN, A. S. et al. Three-dimensional plasmonic nanoclusters. **Nano Letters**, v. 13, n. 9, p. 4399-4403, 2013.
- 157 SHIOHARA, A. et al. Recent approaches toward creation of hot spots for SERS detection. **Journal of Photochemistry and Photobiology C - photochemistry reviews**, v. 21, p. 2-25, 2014. doi: 10.1016/j.jphotochemrev.2014.09.001.

158 LIU, H. L. et al. Dynamic light scattering for gold nanorod size characterization and study of nanorod-protein interactions. **Gold Bulletin**, v. 45, n. 4, p. 187-195, 2012.

159 MARTINEZ-BARBOSA, M. E. et al. PEGylated degradable composite nanoparticles based on mixtures of PEG-b-Poly(gamma-benzyl L-glutamate) and Poly(gamma-benzyl L-glutamate). **Bioconjugate Chemistry**, v. 20, n. 8, p. 1490-1496, 2009.

160 WANG, L. et al. Photothermo-chemotherapy of cancer employing drug leakage-free gold nanoshells. **Biomaterials**, v. 78, p. 40-49, 2016. doi: 10.1016/j.biomaterials.2015.11.024.

161 PIAO, J. G. et al. Erythrocyte membrane is an alternative coating to polyethylene glycol for prolonging the circulation lifetime of gold nanocages for photothermal therapy. **ACS Nano**, v. 8, n. 10, p. 10414-10425, 2014.

162 PAN, Y. et al. Gold nanoparticles of diameter 1.4 nm trigger necrosis by oxidative stress and mitochondrial damage. **Small**, v. 5, n. 18, p. 2067-2076, 2009.

163 YAMASHITA, S. et al. Controlled-release system of single-stranded DNA triggered by the photothermal effect of gold nanorods and its in vivo application. **Bioorganic & Medicinal Chemistry**, v. 19, n. 7, p. 2130-2135, 2011.

164 CHEN, H. Y. et al. Multifunctional gold nanostar conjugates for tumor imaging and combined photothermal and chemo-therapy. **Theranostics**, v. 3, n. 9, p. 633-649, 2013.

165 ZHOU, H. et al. Homophilic adhesion between ig superfamily carcinoembryonic antigen molecules involves double reciprocal bonds. **Journal of Cell Biology**, v. 122, n. 4, p. 951-960, 1993.

166 CHOI, E. K. et al. Upregulation of NAD(P)H : quinone oxidoreductase by radiation potentiates the effect of bioreductive beta-lapachone on cancer cells. **Neoplasia**, v. 9, n. 8, p. 634-642, 2007.

167 PARK, H. J. et al. Susceptibility of cancer cells to beta-lapachone is enhanced by ionizing radiation. **International Journal of Radiation Oncology Biology Physics**, v. 61, n. 1, p. 212-219, 2005.

168 LI, J. X. et al. Toxicity of inorganic nanomaterials in biomedical imaging. **Biotechnology Advances**, v. 32, n. 4, p. 727-743, 2014.

169 BEY, E. A. et al. Catalase abrogates beta-Lapachone-Induced PARP1 hyperactivation-directed programmed necrosis in NQO1-positive breast cancers. **Molecular Cancer Therapeutics**, v. 12, n. 10, p. 2110-2120, 2013.

170 PARK, E. J. et al. beta-Lapachone induces programmed necrosis through the RIP1-PARP-AIF-dependent pathway in human hepatocellular carcinoma SK-Hep1 cells. **Cell Death & Disease**, v. 5, 2014. doi: 10.1038/cddis.2014.202.

171 HERMANN, P. et al. Gadolinium(III) complexes as MRI contrast agents: ligand design and properties of the complexes. **Dalton Transactions**, v. 23, p. 3027-3047, 2008. doi: 10.1039/B719704G.

- 172 KHEMTONG, C. et al. Polymeric nanomedicine for cancer MR imaging and drug delivery. **Chemical Communications**, n. 24, p. 3497-3510, 2009.
- 173 CARAVAN, P. Strategies for increasing the sensitivity of gadolinium based MRI contrast agents. **Chemical Society Reviews**, v. 35, n. 6, p. 512-523, 2006.
- 174 FANG, J. et al. Manipulating the surface coating of ultra-small Gd₂O₃ nanoparticles for improved T₁-weighted MR imaging. **Biomaterials**, v. 35, n. 5, p. 1636-1642, 2014.
- 175 AGULLA, J. et al. Quick adjustment of imaging tracer payload, for in vivo applications of theranostic nanostructures in the brain. **Nanomedicine - nanotechnology biology and medicine**, v. 10, n. 4, p. 851-858, 2014.
- 176 CHO, M. et al. Gadolinium oxide nanoplates with high longitudinal relaxivity for magnetic resonance imaging. **Nanoscale**, v. 6, n. 22, p. 13637-13645, 2014.
- 177 LAURENT, S. et al. Comparative study of the physicochemical properties of six clinical low molecular weight gadolinium contrast agents. **Contrast Media & Molecular Imaging**, v. 1, n. 3, p. 128-137, 2006.
- 178 PENFIELD, J. G.; REILLY, R. F. What nephrologists need to know about gadolinium. **Nature Clinical Practice Nephrology**, v. 3, n. 12, p. 654-668, 2007.
- 179 DAVENPORT, A.; WHITING, S. Profound pseudohypocalcemia due to gadolinium (Magnevist) contrast in a hemodialysis patient. **American Journal of Kidney Diseases**, v. 47, n. 2, p. 350-352, 2006.
- 180 BROOME, D. R. Nephrogenic systemic fibrosis associated with gadolinium based contrast agents: a summary of the medical literature reporting. **European Journal of Radiology**, v. 66, n. 2, p. 230-234, 2008.
- 181 ZHOU, S. Y. et al. PEGylated polyethylenimine as enhanced T₁ contrast agent for efficient magnetic resonance imaging. **ACS Applied Materials & Interfaces**, v. 6, n. 14, p. 11459-11469, 2014.
- 182 CARAVAN, P. et al. Influence of molecular parameters and increasing magnetic field strength on relaxivity of gadolinium- and manganese-based T₁ contrast agents. **Contrast Media & Molecular Imaging**, v. 4, n. 2, p. 89-100, 2009.
- 183 NA, H. B.; HYEON, T. Nanostructured T₁ MRI contrast agents. **Journal of Materials Chemistry**, v. 19, n. 35, p. 6267-6273, 2009.
- 184 LIU, Y. J. et al. Gadolinium-loaded polymeric nanoparticles modified with Anti-VEGF as multifunctional MRI contrast agents for the diagnosis of liver cancer. **Biomaterials**, v. 32, n. 22, p. 5167-5176, 2011.
- 185 WEN, S. H. et al. Multifunctional dendrimer-entrapped gold nanoparticles for dual mode CT/MR imaging applications. **Biomaterials**, v. 34, n. 5, p. 1570-1580, 2013.

186 GROGNA, M. et al. Polymer micelles decorated by gadolinium complexes as MRI blood contrast agents: design, synthesis and properties. **Polymer Chemistry**, v. 1, n. 9, p. 1485-1490, 2010.

187 ANANTA, J. S. et al. Geometrical confinement of gadolinium-based contrast agents in nanoporous particles enhances T-1 contrast. **Nature Nanotechnology**, v. 5, n. 11, p. 815-821, 2010.

188 SONG, Y. et al. Multimodal gadolinium-enriched DNA-gold nanoparticle conjugates for cellular imaging. **Angewandte Chemie International Edition**, v. 48, n. 48, p. 9143-9147, 2009.

189 PARK, J. A. et al. Gold nanoparticles functionalized by gadolinium-DTPA conjugate of cysteine as a multimodal bioimaging agent. **Bioorganic & Medicinal Chemistry Letters**, v. 20, n. 7, p. 2287-2291, 2010.

190 MORIGGI, L. et al. Gold nanoparticles functionalized with gadolinium chelates as high-relaxivity MRI contrast agents. **Journal of the American Chemical Society**, v. 131, n. 31, p. 10828-+, 2009.

191 KIELAR, F. et al. Large relaxivity enhancement of paramagnetic lipid nanoparticles by restricting the local motions of the Gd-III chelates. **Journal of the American Chemical Society**, v. 132, n. 23, p. 7836-+, 2010.

192 GHAGHADA, K. B. et al. New dual mode gadolinium nanoparticle contrast agent for magnetic resonance imaging. **Plos One**, v. 4, n. 10, 2009. doi:10.1371/journal.pone.0007628.

193 ROHRER, M. et al. Comparison of magnetic properties of MRI contrast media solutions at different magnetic field strengths. **Investigative Radiology**, v. 40, n. 11, p. 715-724, 2005.

194 COUGHLIN, A. J. et al. Gadolinium-conjugated gold nanoshells for multimodal diagnostic imaging and photothermal cancer therapy. **Small**, v. 10, n. 3, p. 556-565, 2014.

195 ROTZ, M. W. et al. High relaxivity Gd(III) - DNA gold nanostars: investigation of shape effects on proton relaxation. **ACS Nano**, v. 9, n. 3, p. 3385-3396, 2015.

196 TENZER, S. et al. Rapid formation of plasma protein corona critically affects nanoparticle pathophysiology. **Nature Nanotechnology**, v. 8, n. 10, p. 772-U1000, 2013.

197 SWANSON, S. D. et al. Targeted gadolinium-loaded dendrimer nanoparticles for tumor-specific magnetic resonance contrast enhancement. **International Journal of Nanomedicine**, v. 3, n. 2, p. 201-210, 2008.

198 HAK, S. et al. A high relaxivity Gd(III)DOTA-DSPE-based liposomal contrast agent for magnetic resonance imaging. **European Journal of Pharmaceutics and Biopharmaceutics**, v. 72, n. 2, p. 397-404, 2009.

199 PARK, J. Y. et al. Paramagnetic Ultrasmall Gadolinium Oxide Nanoparticles as Advanced T-1 MR1 Contrast Agent: Account for Large Longitudinal Relaxivity, Optimal Particle Diameter, and In Vivo T-1 MR Images. **ACS Nano**, v. 3, n. 11, p. 3663-3669, 2009.

- 200 AYALA-OROZCO, C. et al. Fluorescence enhancement of molecules inside a gold nanomatrix. **Nano Letters**, v. 14, n. 5, p. 2926–2933, 2014.
- 201 SOHAEBUDDIN, S. K. et al. Nanomaterial cytotoxicity is composition, size, and cell type dependent. **Particle and Fibre Toxicology**, v. 7, 2010. doi: 10.1186/1743-8977-7-22.
- 202 SINIGAGLIA, G. et al. Catalytically active bovine serum amine oxidase bound to fluorescent and magnetically drivable nanoparticles. **International Journal of Nanomedicine**, v. 7, p. 2249-2259, 2012. doi: 10.2147/IJN.S28237.
- 203 TÓTH, É. et al. The role of water exchange in attaining maximum relaxivities for dendrimeric MRI contrast agents. **Chemistry - a european journal**, v. 2, n. 12, p. 1607–1615, 1996.
- 204 STRIJKERS, G. J. et al. Relaxivity of liposomal paramagnetic MRI contrast agents. **Magnetic Resonance Materials in Physics Biology and Medicine**, v. 18, n. 4, p. 186-192, 2005.
- 205 HU, F. Q.; ZHAO, Y. S. Inorganic nanoparticle-based T-1 and T-1/T-2 magnetic resonance contrast probes. **Nanoscale**, v. 4, n. 20, p. 6235-6243, 2012.
- 206 COURANT, T. et al. Hydrogels Incorporating GdDOTA: Towards Highly Efficient Dual T1/T2 MRI Contrast Agents. **Angewandte Chemie International Edition**, v. 51, n. 36, p. 9119-9122, 2012.
- 207 HUANG, C. C. et al. Enhancing Transversal Relaxation for Magnetite Nanoparticles in MR Imaging Using Gd³⁺-Chelated Mesoporous Silica Shells. **ACS Nano**, v. 5, n. 5, p. 3905-3916, 2011.
- 208 JOKERST, J. V. et al. Nanoparticle PEGylation for imaging and therapy. **Nanomedicine**, v. 6, n. 4, p. 715-728, 2011.
- 209 TOTH, E. et al. The role of water exchange in attaining maximum relaxivities for dendrimeric MRI contrast agents. **Chemistry-a european journal**, v. 2, n. 12, p. 1607-1615, 1996.
- 210 STRAUCH, R. C. et al. Reporter Protein-Targeted Probes for Magnetic Resonance Imaging. **Journal of the American Chemical Society**, v. 133, n. 41, p. 16346-16349, 2011.
- 211 CHO, M. J. et al. Gadolinium oxide nanoplates with high longitudinal relaxivity for magnetic resonance imaging. **Nanoscale**, v. 6, n. 22, p. 13637-13645, 2014.
- 212 SUN, G. Y. et al. Synthesis and evaluation of novel polysaccharide-Gd-DTPA compounds as contrast agent for MRI. **Journal of Magnetism and Magnetic Materials**, v. 265, n. 2, p. 123-129, 2003.
- 213 CARAVAN, P. et al. Influence of molecular parameters and increasing magnetic field strength on relaxivity of gadolinium- and manganese-based T(1) contrast agents. **Contrast Media & Molecular Imaging**, v. 4, n. 2, p. 89-100, 2009.

- 214 RAYMOND, K. N.; PIERRE, V. C. Next generation, high relaxivity gadolinium MRI agents. **Bioconjugate Chemistry**, v. 16, n. 1, p. 3-8, 2005.
- 215 GOODMAN, A. M. et al. The Surprising in Vivo Instability of Near-IR-Absorbing Hollow Au-Ag Nanoshells. **ACS Nano**, v. 8, n. 4, p. 3222-3231, 2014.
- 216 ROHRER, M. et al. Comparison of Magnetic Properties of MRI Contrast Media Solutions at Different Magnetic Field Strengths, Investigative Radiology. **Investigative Radiology**, v. 40, n. 11, p. 715-724, 2005.
- 217 KIELAR, F. et al. Large Relaxivity Enhancement of Paramagnetic Lipid Nanoparticles by Restricting the Local Motions of the Gd-III Chelates. **Journal of the American Chemical Society**, v. 132, n. 23, p. 7836-7837, 2010.
- 218 BRUCKMAN, M. A. et al. Engineering Gd-loaded nanoparticles to enhance MRI sensitivity via T-1 shortening. **Nanotechnology**, v. 24, n. 46, p. 462001-462037, 2013.
- 219 MAEDA, H. et al. Polymeric drugs for efficient tumor-targeted drug delivery based on EPR-effect. **European Journal of Pharmaceutics and Biopharmaceutics**, v. 71, n. 3, p. 409-419, 2009.
- 220 ROHRER, M. et al. Comparison of magnetic properties of MRI contrast media solutions at different magnetic field strengths. **Invest Radiol**, v. 40, n. 11, p. 715-724, 2005.
- 221 BARDHAN, R. et al. Nanosphere-in-a-Nanoshell: A Simple Nanomatryushka. **Journal of Physical Chemistry C**, v. 114, n. 16, p. 7378-7383, 2010.
- 222 SOHAEBUDDIN, S. K. et al. Nanomaterial cytotoxicity is composition, size, and cell type dependent. **Particle and Fibre Toxicology**, v. 7, n. 22, p. 1-17, 2010.
- 223 LAUFFER, R. B. Paramagnetic metal complexes as water proton relaxation agents for NMR imaging: theory and design. **Chemical Reviews**, v. 87, n. 5, p. 901-927, 1987.
- 224 LAURENT, S. et al. Comparative study of the physicochemical properties of six clinical low molecular weight gadolinium contrast agents. **Contrast Media & Molecular Imaging**, v. 1, n. 3, p. 128-137, 2006.
- 225 SVITOVA, A. L. et al. Magnetic moments and exchange coupling in nitride clusterfullerenes Gd_xSc_{3-x}N@C₈₀ (x = 1-3). **Dalton Transactions**, v. 43, n. 20, p. 7387-7390, 2014.
- 226 NEALON, G. L. et al. Magnetism in gold nanoparticles. **Nanoscale**, v. 4, p. 5244-5258, 2012.